Tracer-Kinetic Model-Driven Motion Correction with Application to Renal DCE-MRI

Dimitra Flouri

Submitted in accordance with the requirements for the degree of
Doctor of Philosophy

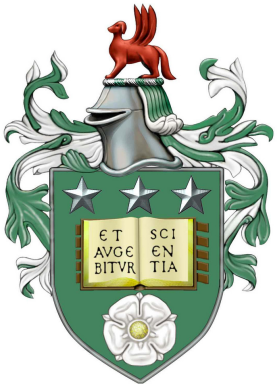

The University of Leeds

Department of Applied Mathematics
&
Division of Biomedical Imaging

November, 2016

The candidate confirms that the work submitted is her own, except where work which has formed part of jointly authored publications has been included. The contribution of the candidate and the other authors to this work has been explicitly indicated below. The candidate confirms that appropriate credit has been given within the thesis where reference has been made to the work of others.

Joint Publications

Work from the following jointly authored paper, which is listed as [44] in the References, is included in this thesis:

Journal Paper:

Flouri, D., Lesnic, D. and Sourbron, S. P. (2016). Fitting the two-compartment model in DCE-MRI by linear inversion. Magnetic Resonance in Medicine, **76**, 998-1006.

Chapter 3 of this thesis is based on work contained in this paper. The candidate performed all the numerical implementation and computational work, as well as many other aspects. Some of the theoretical proofs jointly performed with co-authors.

Conference Abstracts:

Flouri, D., Lesnic, D., Crysochou, C., Kalra, P. and Sourbron, S. P. (2017). Motion correction for 3D free-breathing renal DCE-MRI using tracer-Kinetic model-driven registration. ISMRM 2017, Honolulu, USA. Oral presentation.

Flouri, D., Lesnic, D. and Sourbron, S. P. (2016). Motion correction in DCE-MRI by tracer-kinetic model-driven registration: Beyond the Tofts model. ISMRM 2016, Singapore. Oral presentation.

Flouri D, SP Sourbron and D Lesnic. (2015). Tracer-kinetic model driven registration for DCE-MRI using free-form deformation. 32nd Annual Scientific Meeting, ESMRMB 2015, Edinburgh, Scotland, UK. Oral presentation.

Flouri, D., Lesnic, D. and Sourbron, S. P. (2013). Fitting the two-compartment model with linear inversion. 30th Annual Scientific Meeting, ESMRMB 2013, Toulouse, France. e-Poster presentation.

Flouri, D., Lesnic, D. and Sourbron, S. P. (2013). Fitting the two-compartment model with linear inversion. 19th Annual Scientific Meeting of the British Chapter for the ISMRM 2013, York, UK. Poster presentation.

Flouri, D., Lesnic, D. and Sourbron, S. P. (2013). Fitting the Two-compartment model with linear inversion. Postgraduate Symposium of the British Chapter of ISMRM 2013, London, UK. Poster presentation.

The work presented in Chapter 4 lead to conference publications at ESMRMB 2015 and ISMRM 2016. The work included in Chapter 5 has been submitted to ISMRM 2017. In the above conference abstracts the candidate performed all the numerical implementation and computational work, as well as many other aspects. Some of the theoretical proofs jointly performed with co-authors.

When mathematics meets medicine...

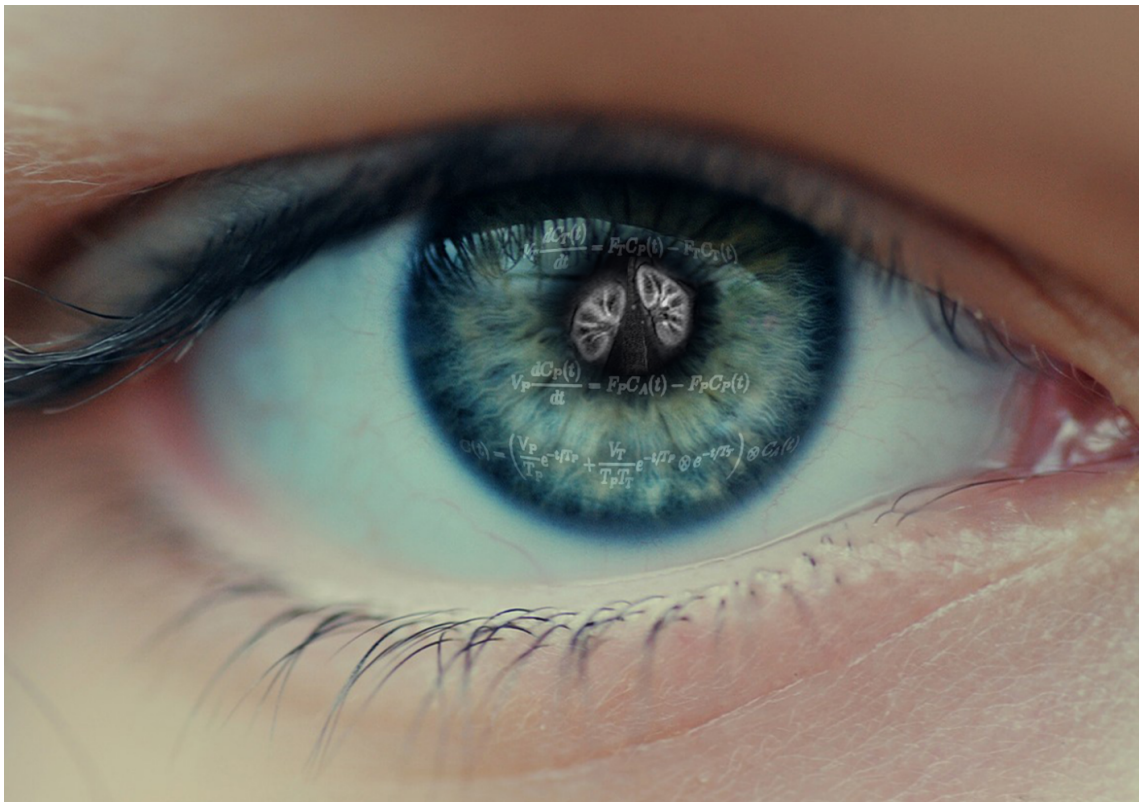

University of Leeds Annual Showcase 2015 - 2^{nd} Prize Award

Acknowledgments

First and foremost I would like to thank my supervisors, Daniel Lesnic and Steven Sourbron for their help and advice over the last four years. Their support and guidance all along this experience was valuable and essential for the progress of the study. I am particularly indebted to Steven, for the generosity he has displayed in giving his time and leading his experience. I also want to thank my industrial supervisor, Philip Murphy for his support at various stages of the project. I also offer my thanks to Mark Kelmanson who introduced me to this project and therefore the reason of the beginning of this journey.

More generally, I would like to thank all the staff of the School of Mathematics for their help with all the little things that keep everything running smoothly. I also would like thank all my friends and postgraduate colleagues who also do or did a PhD for sharing the many good moments with me.

On a personal note, I wish to thank my parents Stelio and Lenia, who supported me and for always being there for me. Words cannot explain how grateful I am for having the best parents one could ask for. I would also like to thank my beloved sisters Chara and Maria for always believing in me and for their invaluable help during these four years.

The work presented in this thesis was supported by the Engineering and Physical Sciences Research Council (EPSRC) in partnership with GlaxoSmithKline (GSK). I am grateful to my sponsors for their financial support.

Abstract

A major challenge of the image registration in dynamic contrast-enhanced magnetic resonance imaging (DCE-MRI) is related to the image contrast variations caused by the contrast agent passage. Tracer-kinetic model-driven motion correction is an attractive solution for DCE-MRI, but previous studies only use the 3-parameter modified Tofts model. Firstly, a generalisation based on a 4-parameter 2-compartment tracer-kinetic model is presented. A practical limitation of these models is the need for non-linear least-squares (NLLS) fitting. This is prohibitively slow for image-wide parameter estimations, and is biased by the choice of initial values. To overcome this limitation, a fast linear least-squares (LLS) method to fit the two-compartment exchange and -filtration models (2CFM) to the data is introduced. Simulations of normal and pathological data were used to evaluate calculation time, accuracy and precision of the LLS against the NLLS method. Results show that the LLS method leads to a significant reduction in the calculation times. Secondly, a novel tracer-kinetic model-driven motion correction algorithm is introduced which uses a 4-parameter 2-compartment model to tackle the problem of image registration in 2D renal DCE-MRI. The core architecture of the algorithm can briefly described as follows: the 2CFM is linearly fitted pixel-by-pixel and the model fit is used as target for registration; then a free-form deformation model is used for pairwise co-registration of source and target images at the same time point. Another challenge that has been addressed is the computational complexity of non-rigid registration algorithms by precomputing steps to remove redundant calculations. Results in 5 subjects and simulated phantoms show that the algorithm is computationally efficient and improves alignment of the data. The proposed registration algorithm is then translated to 3D renal dynamic MR data. Translation to 3D is however challenging due to ghosting artefacts caused by within-frame breathing motion. Results in 8 patients show that the algorithm effectively removes between-frame breathing motion despite significant within-frame artefacts. Finally, the effect of motion correction on the clinical utility has been examined. Quantitative evaluation of single-kidney glomerular filtration rate derived from DCE-MRI against reference measurements shows a reduction of the bias, but precision is limited by within-frame artefacts.

The suggested registration algorithm with a 4-parameter model is shown to be a computational efficient approach which effectively removes between-frame motion in a series of 2D and 3D renal DCE-MRI data.

Abbreviations

AIF	Arterial Input Function
ARVD	Atherosclerotic Renovascular Disease
CI	Confidence Interval
CKD	Chronic Kidney Disease
CNR	Contrast-to-Noise Ratio
CT	Computed Tomography
DCE	Dynamic Contrast-Enhanced
DICOM	Digital Imaging and Communications in Medicine
DMSA	Dimercaptosuccinic Acid
DOTA	Tetraazacyclododecane Tetraacetic Acid
DTPA	Diethylenetriamine Pentaacetic Acid
EDTA	Ethylenediaminetetraacetic Acid
EES	Extracellular Extravascular Space
ESRF	End Stage Renal Failure
FFD	Free Form Deformation
FID	Free Induction Decay
FoM	Figures of Merit
Gd	Gadolinium
GE	Gradient Echo
GFR	Glomerular Filtration Rate
GLLS	Generalized Linear Least-Squares
GPU	Graphical Processing Unit
LLS	Linear Least-Squares
MR	Magnetic Resonance
MRI	Magnetic Resonance Imaging
NLLS	Nonlinear Least-Squares
NMR	Nuclear Magnetic Resonance
PET	Positron Emission Tomography
PMI	Platform for Research in Medical Imaging
RAS	Renal Artery Stenosis
RF	Radio Frequency
ROI	Region of Interest
SD	Standard Deviation
SE	Spin Echo

SENSE	Sensitivity Encoding
SK-GFR	Single-Kidney Glomerular Filtration Rate
SNR	Signal-to-Noise Ratio
SSD	Sum of Squared Differences
SVD	Singular Value Decomposition
TE	Echo Time
TR	Repetition Time
WLLS	Weighted Linear Least-Squares
2CFM	Two-Compartment Filtration Model
2CXM	Two-Compartment Exchange Model
2D	Two-Dimensional
3D	Three-Dimensional

List of Symbols

A	Amplitude
[CA]	Concentration of the contrast agent
B	B-spline basis functions
$\mathbf{B_0}$	Static magnetic field
$\mathbf{B_1}$	Oscillating external magnetic field
C	Concentration of the contrast agent in a tissue
c_a	Concentration of the contrast agent in arterial blood
c_e	Concentration of the contrast agent in extravascular volume
$\mathcal{C}$	Cost Function
C_i^{fit}	Fitted concentrations
C_i^{msr}	Measured concentrations
c_p	Concentration of the contrast agent in plasma volume
c_T	Concentration of the contrast agent in tubular volume
E	Extraction fraction
E_i	Error
F_p	Plasma flow
F_T	Tubular flow
$\mathbf{G_{FE}}$	Frequency encoding gradient
I	Impulse response function
I_{corr}	Motion corrected image
I_{source}	Source image
I_{target}	Target image
J_i	Compartment inlet
J_o	Compartment outlet
M_{xy}	Net transverse magnetisation
M_z	Net longitudinal magnetisation
$\mathbf{M_0}$	Net magnetisation in z-direction
P_i	Reconstructed parameter
PS	Permeability-surface area product
T_1	Longitudinal (spin-lattice) relaxation time constant
$T_{1,0}$	Baseline longitudinal relaxation time
T_2	Transverse (spin-spin) relaxation time constant
T_2^*	Transverse relaxation time constant with microscopic field inhomogeneities
T	Mean transit times of combined system

$\mathbf{T}$	Transformation
$\mathbf{T}(\mathbf{x})$	Transformed position of location $\mathbf{x}$
Tacq	Acquisition time
T_e	Mean transit times of the extravascular compartment
T_p	Mean transit times of the blood
T_T	Mean transit time in the tubular compartment
$\mathbf{v}$	Eigenvector
v_e	Extravascular volume
v_i	Intracellular fraction volume
v_p	Plasma volume
v_T	Tubular volume
W	Weighting function
$\mathbf{x}$	Location in image domain
α	Flip angle
γ	Gyromagnetic ratio
Δ	Discriminant
λ	Eigenvalue
μ	Angular momentum
ρ	Spearman's rank correlation coefficient
$\omega_\mathbf{0}$	Angular frequency
Ω	Image domain
$\mathcal{C}$	Cost function

Contents

List of Figures

List of Tables

Chapter 1

Introduction

1.1 Context and Motivation

The desire for accurate quantification of diagnosis and therapy monitoring has led to the formation of many new medical imaging modalities such as the Magnetic Resonance Imaging (MRI). The increased sophistication of MRI has brought additional challenges to the area of medical image registration. The use of contrast agents for Dynamic Contrast-Enhanced MRI (DCE-MRI) to alter image contrast in regions of interest have increased use in recent years [3]. DCE-MRI allows for non-invasive quantitative analysis for contrast agent to extract quantitative information from image data in such a way that the information can contribute to clinical care.

The monitoring of uptake and washout of contrast agent in tissues requires long scan times leading to many images with different contrast and image misalignments due to motion of the patient during the acquisition. Such misalignments have strong impact on the analysis of DCE-MRI data and image registration is thus required. In addition, changes to the intensity of some parts of an image relative to others are a major challenge as this affects the pixel-by-pixel intensity matching assumed by many registration algorithms. Image registration is important when someone is seeking to extract information from multiple images. Good alignment of the images is required so that equivalent imaging pixels represent the same structures and therefore can be compared.

DCE-MRI plays a significant role in many applications, such as perfusion imaging,

MR angiography and MR renography [4]. This thesis focuses on the latter application, i.e. DCE-MRI of the kidneys. Glomerular Filtration Rate (GFR) is considered to be the most useful index of kidney function. It is traditionally measured by radioisotope measurement techniques which are time consuming and involve ionising radiation exposure. A potential alternative to radioisotope measurement techniques is DCE-MRI which enables measurements of single-kidney GFR (SK-GFR) and renal perfusion in one imaging session.

1.2 Objectives of the Thesis

The different studies presented in this thesis focus on solutions proposed to address the challenges stated above. The main objective of the presenting work is to develop and evaluate a registration algorithm which incorporates the tracer-kinetic information to motion correction process to account for signal intensity changes due to the passage of contrast agent. The proposed algorithm is an iterative model-based registration method. The model fit is used as a target for image registration where each source image is registered to its corresponding target image instead of registering all the source images to a single target. Non-linear least-squares methods are the most commonly used algorithms to fit tracer-kinetic models to the data. This type of method requires considerable computation time and therefore may become impractical for image-wide parameter estimations. This thesis addresses this issue by presenting a fast linear least-squares method to fit the two-compartment exchange and filtration models to the data. The effect of motion correction on the clinical utility is also presented.

The specific objectives of the study as stated above are as follows:

1. Develop a fast linear least-squares method to fit the two-compartment exchange and -filtration models.
2. Develop a tracer-kinetic model-driven motion correction algorithm for two-dimensional (2D) renal DCE-MRI data in order to overcome the problem of the registration of images containing local contrast changes.
3. Translate the tracer-kinetic model-driven motion correction algorithm to three-dimensional (3D) renal DCE-MRI data.

4. Investigate the accuracy and precision of DCE-MRI measured SK-GFR before and after motion correction, using radioisotope measurements as the reference method in the context of clinical routine.

1.3 Thesis Overview

The thesis is divided into six main chapters. Each of these contains thematically related sections and all parts build upon each other. The outline of the thesis reads as follows:

Chapter 2: Background

Knowledge that is required to comprehend all subsequent chapters is to be provided in a concise way. A brief description of the concept of MR theory and contrast agents used in MRI, followed by a more specific presentation of quantitative DCE-MRI is given. This chapter also introduces background concepts that are the foundation for the deformable medical image registration. Detailed literature reviews are integrated in later chapters.

Chapter 3: Linear Least-Squares Method for multi-compartment models

Non-linear least-squares methods are the most commonly used algorithms to fit tracer-kinetic models to the data. This type of methods require a choice of initial values which is updated iteratively using gradient-descent type methods, until the difference between predicted and measured data is minimal. The process is slow, and there is a risk of convergence to local minima. If this happens the result is biased by the initial guess. An alternative is the use of linear least squares methods, which produce parameter estimates by solving a linear system of equations. This chapter discusses the development of a fast linear least squares methods to fit the two-compartment exchange and -filtration models. Preliminary work on the development of linear least-squares method to fit simpler models such as the Tofts and modified Tofts models is also presented. The preliminary work aimed to ensure that the claims stated in the literature are valid. Related work done by other research groups is also outlined.

Chapter 4: Model-based Motion Correction in DCE-MRI

This chapter is about motion correction in 2D renal DCE-MRI. A major challenge of motion correction in DCE-MRI is related to the contrast variations between image pairs or among temporal sequences caused by the passage of contrast agent. A novel registration technique which incorporates the use of a 4-parameter 2-compartment tracer-kinetic model in the motion correction process is introduced and defined as: tracer-kinetic model-driven registration. The application of the proposed registration algorithm to a total of 5 DCE-MRI datasets and simulated phantom is presented. The data processed were acquired under free breathing. Existing methods to register DCE-MRI data are also discussed.

Chapter 5: Application of Tracer-Kinetic Model-Driven Registration to Renal DCE-MRI Data

The tracer-kinetic model-driven registration algorithm developed in Chapter 4 is now extended to 3D renal DCE-MRI data. The extended algorithm is applied to renal DCE-MRI data acquired during free breathing. The development of 3D registration is discussed alongside with the analogous problems impacting image registration due to ghosting artefacts cause by within-frame breathing motion. The application of registration algorithm is aimed to assess the clinical benefit of using motion correction as a pre-processing step for quantification of SK-GFR in DCE-MRI analysis.

Chapter 6: General Conclusions and Future Work

The most important conclusions discussed in the thesis are summarised and closing remarks are given. Possible directions for future work on related topics are provided.

Chapter 2

Background

2.1 Introduction

This chapter introduces the background theory to the research area in order to fully understand the methods used and the different aspects of this work. The chapter begins with a brief description of the concept of MRI (Section 2.2) followed by Section 2.3 which gives a more specific presentation of quantitative DCE-MRI technique used in this thesis. Section 2.4 describes the kidney anatomy and physiology. Subsequently, a general introduction to tracer-kinetic theory is given in Section 2.5 along with an introduction of the tracer-kinetic models that have become standard for the analysis of DCE-MRI. Finally, Section 2.6 gives a description of what image registration is followed by a presentation of its main components and the challenge of motion correction in DCE-MRI data.

2.2 Magnetic Resonance Imaging

MRI is a non-invasive and relatively recent medical imaging technique. It is based upon the principle of nuclear magnetic resonance (NMR) and thus does not involve the use of ionising radiation, unlike other imaging modalities based on X-rays or radioactive isotopes. MRI makes possible the acquisition in any imaging plane (axial, coronal, sagittal), see Figure 2.1. The main advantage of MRI is that it gives good soft-tissue contrast and does not use ionising radiation.

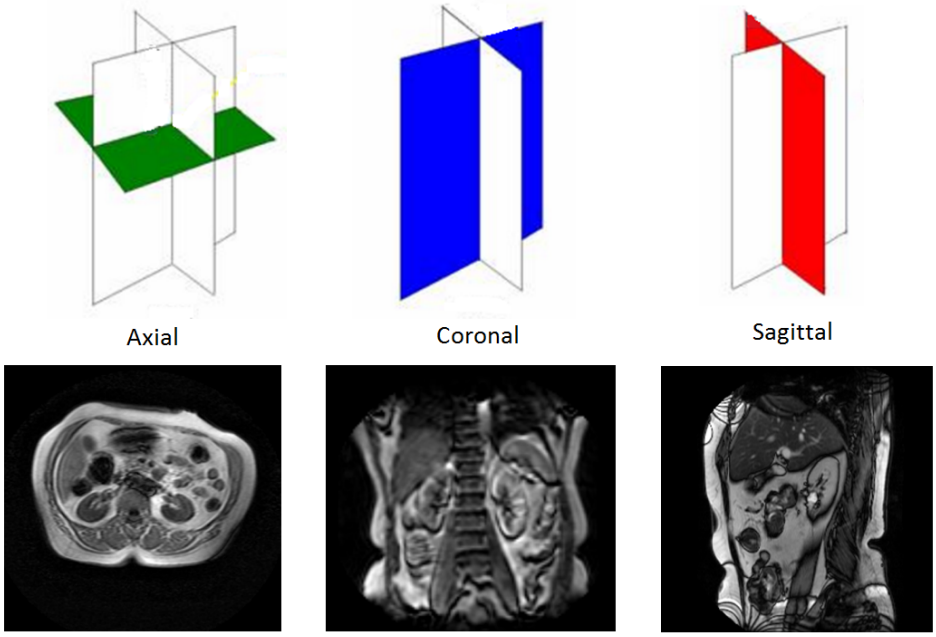

Figure 2.1: An axial image, a coronal image and a sagittal image of the kidneys.

The principle of magnetic resonance (MR) was discovered in the mid 1940's by Felix Bloch and Edward Purcell independently [1]. MR uses the fact that protons immersed in a static magnetic field can be excited by a radiofrequency (RF) field at the resonance frequency. In 1971, Raymond Damadian discovered that normal tissues and tumours excited at the same frequency have different relaxation times [1]. This has opened the door to a new era of MRI for medical use. In recent years, MRI has become a powerful imaging tool used for diagnosis, surgery planning and monitor treatments.

2.2.1 MRI Theory

As mentioned above NMR is the foundation on which MRI is built. NMR is a physical phenomenon that occurs when certain elements interact with a magnetic field. In order to demonstrate NMR these elements must have a magnetic moment and a spin angular momentum [5]. A large percentage of human body is made up of water about 70%, therefore, the hydrogen atoms in water are a good choice of magnetic resonance. The hydrogen nucleus exhibits an intrinsic property called spin angular momentum. In the absence of an external magnetic field, the orientation of

the spins will be random as illustrated in Figure 2.2.

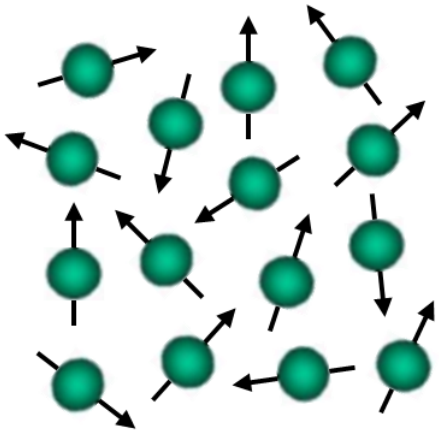

Figure 2.2: Randomly oriented spins outside a magnetic field.

When inside the static magnetic field of the scanner ($\mathbf{B_0}$) spins are going to precess around $\mathbf{B_0}$ in a trajectory describing a cone because of spin angular momentum, as illustrated in Figure 2.3. It is important to note that the spins never fully assume a truly parallel or antiparallel orientation with $\mathbf{B_0}$. The angular frequency ($\omega_\mathbf{0}$) of precession is given by Larmor's equation:

$$\omega_\mathbf{0} = \gamma \mathbf{B_0}, \tag{2.1}$$

where γ is the gyromagnetic ratio (constant). The precession is then described by the Bloch equation:

$$\frac{d\boldsymbol{\mu}}{dt} = \omega_\mathbf{0} \times \boldsymbol{\mu}, \tag{2.2}$$

where $\boldsymbol{\mu}$ is the magnetic moment.

Although the precession of spins is initially isotropic, due to the finite temperature (e.g. body temperature) of the sample this isotropy breaks down leading to an anisotropic precession of spins. It is slightly more likely that the cone of precession of spins are driven towards an orientation with low magnetic energy, that is parallel to $\mathbf{B_0}$, than a high magnetic energy (i.e. antiparallel to $\mathbf{B_0}$). This slight difference results in a net magnetisation ($\mathbf{M}$). When no scanning is taking place the initial net

magnetisation ($\mathbf{M_0}$) is aligned with the static magnetic field $\mathbf{B_0}$. MR occurs when a RF pulse ($\mathbf{B_1}$) at the Larmor frequency is applied. This causes $\mathbf{M_0}$ to tilt away from $\mathbf{B_0}$. The direction of the $\mathbf{B_0}$ field is usually designated as the z-axis. Since $\mathbf{M_0}$ is tipped out of alignment with the $\mathbf{B_0}$ field it forms a component on the transverse plane (M_{xy}), see Figure 2.4. The M_{xy} component while moving away from the z-axis is actually precessing around it inducing an electromagnetic field. In the presence of a receiver coil, the variation of the M_{xy} induces a current which when amplified can be detected. This is called the NMR signal or free-induction decay (FID).

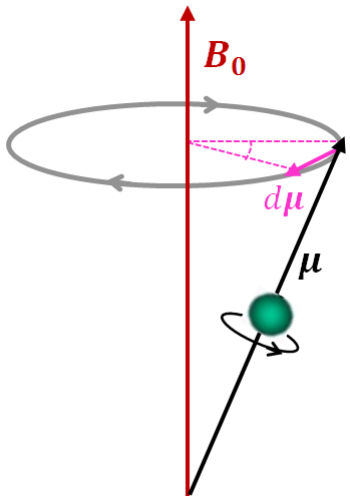

Figure 2.3: Schematic representation of precession of an isolated magnetic moment $\boldsymbol{\mu}$ in a static magnetic field $\mathbf{B_0}$.

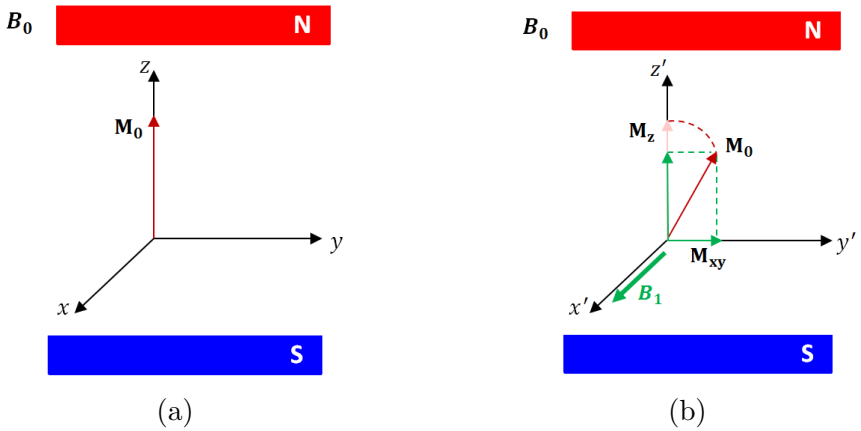

(a) (b)

Figure 2.4: (a) The net magnetisation $\mathbf{M_0}$ in the equilibrium state. (b) The presence of the RF pulse $\mathbf{B_1}$ tips the spin towards the xy-plane and produces two magnetisation components M_z and M_{xy}.

2.2.2 Relaxation Mechanism

The spin system remains in the excited state during the applied RF pulse, however when the RF is stopped, energy is lost so that the spin system gets back to its equilibrium state. This process is called relaxation and can be divided into two mechanism: longitudinal relaxation of the M_z component and transverse relaxation of the M_{xy} component. We have already seen that an RF pulse promotes the hydrogen nuclei with low energy state to high energy state causing a net absorption of energy. The longitudinal relaxation of the M_z component corresponds to the spin-lattice relaxation and is characterised by the time constant T_1. This type of relaxation is the loss of the excess energy from the system of spins to the surrounding environment or lattice. The recovery of longitudinal magnetisation is described by the equation [6]:

$$M_z(t) = M_0(1 - e^{-t/T_1}). \tag{2.3}$$

The transverse relaxation corresponds to the spin-spin relaxation and is characterised by the time constant T_2. This type of relaxation arises in the system of spins that does not involve an exchange of energy with the lattice, but rather a loss of phase coherence between spins (i.e. spins have different phase and frequency). The dephasing due to both T_2 decay and the magnetic field inhomogeneities are indicated as T_2^*.

2.2.3 Acquisition

2.2.3.1 Spatial Encoding

The technique for spatial encoding of the NMR signal that allows us to produce MR images is achieved by using a gradient in the magnetic field, i.e. a static field increase linearly in strength in the given direction along the x, y or z-axis. In order to be able to spatially locate different tissue types it is necessary to get a separate signal from volumes of space (voxels). In 2D acquisition, only one slice is excited at a time. The first step of spatial encoding is slice selection. To do this, a field gradient is applied in conjunction with the RF pulse along a given axis of space so that a

thin slab of tissue is excited corresponding to the range of increasing frequencies generated by the gradient. Each element of the selected 2D slice is then encoded in frequency and phase.

The first direction encoded by applying a frequency encoding gradient ($\mathbf{G_{FE}}$) at the time of measurement along one of the two in-plane dimensions of the selected slice (typically the x-direction). While it is applied, all the spins in that slice are precessing at a frequency, (f), that depends on the static magnetic field plus however much gradient magnetic field they experienced. The amount of the gradient magnetic field experienced by those spins depends on their location along the selected direction, i.e. at any point $\mathbf{x}$ the f will be:

$$f(\mathbf{x}) = \gamma(B_0 + \mathbf{x}\mathbf{G_{FE}}). \tag{2.4}$$

Hence, the measured signal is composed of different components signals each of which has a different frequency.

The second direction can be spatially encoded by applying a phase encoding gradient along the other in-plane dimension (typically the y-axis) which intervenes for a limited period of time. At this point one should notice that this second gradient is applied before the frequency encoding gradient. While the gradient is applied, it temporarily modifies the speed at which proton spins precess, inducing dephasing. When the gradient is interrupted, spins return back to their original precession frequency but maintain the phase angle obtained from the gradient applied. The process is repeated at different strengths of the gradient resulting in a range of different phases. The number of phase encoding steps defines the number of pixels in the phase encoding direction [7]. For example, if the matrix size is 128×128 that would mean that we need 128 phase encoding steps and 128 frequency encoding steps.

The spatial frequency and phase information that comprise the measured MR signal are digitized and stored into k-space. A Fourier transform of k-space values is then decodes this information and generates the final MR image.

2.2.3.2 Basic Pulse Sequences

Pulse sequences are a pattern of RF pulses and magnetic field gradients that are used to construct images. In MRI, the two main types of pulse sequences are spin echo (SE) and gradient echo (GE). Before introduce the main pulse sequence it is essential to define the term flip angle. The flip angle is the amount of rotation of the $\mathbf{M_0}$ experiences during application of a RF pulse.

In SE sequences a 90° RF excitation pulse is applied to excite the hydrogen nuclei, as illustrated in Figure 2.5. After the 90° RF pulse the spins start to dephase immediately as some are processing faster due to higher local field strength, and some slower due to lower field strength, than the average. After a certain amount of time an additional 180° is applied, see Figure 2.6. Such a pulse inverts the dephasing causing a rephasing of the spins, or echo, after a period of time equal to the original dephasing time. In MRI, the term TE is the echo time (i.e. the time between the initial 90° RF pulse and the spin echo) and TR is the repetition time (i.e. the time between two consecutive 90° RF pulse).

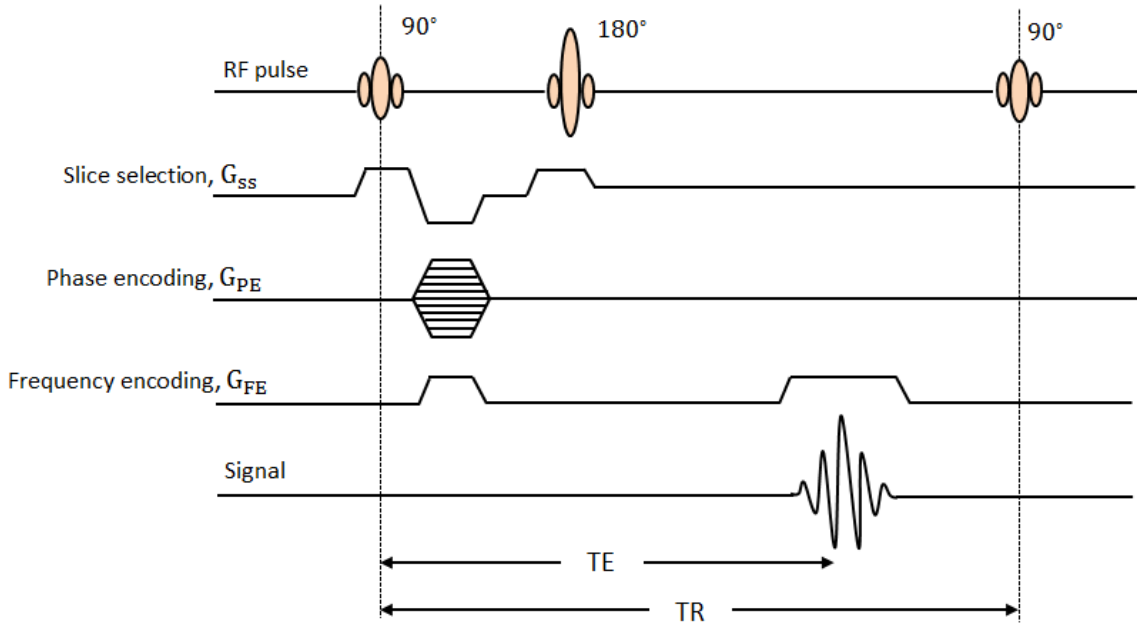

Figure 2.5: Spin echo pulse sequence diagram (modification of [1]).

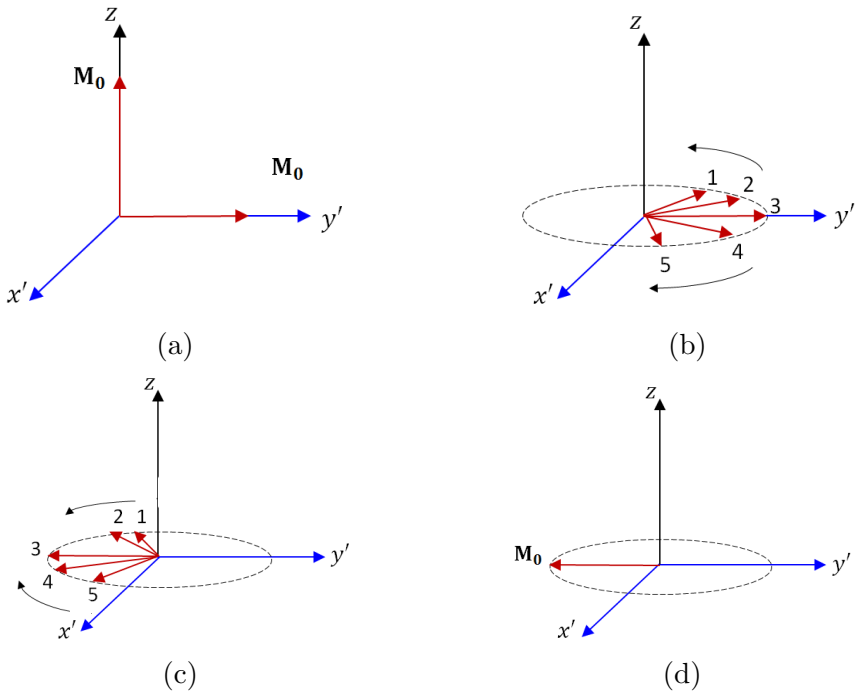

Figure 2.6: Dephasing and rephasing during the spin echo sequence. (a) Right after the 90° RF pulse. (b) The spins start to dephase. (c) After the 180° RF pulse the sign of the phase lag is changed and the spins start to rephase again. (d) The individual spins are in phase again at the echo time.

A GE sequence does not require an additional 180° pulse, instead a gradient magnetic field is applied to rephase the spins (see Figure 2.7). Due to the absence of a 180° RF pulse, a GE makes the sequence more time efficient than the SE allowing MR signal measurements with shorter TR to be achieved. The received signal in this type of sequence depends on T_2^* rather than T_2. The signal equation for the GE sequence is given by:

$$S_{GE} = \rho \frac{(1 - e^{-\mathrm{TR}/T_1})sin(\alpha)}{1 - e^{-\mathrm{TR}/T_1}cos(\alpha)} e^{-\mathrm{TE}/T_2^*}, \tag{2.5}$$

where ρ is proportional to the proton density within a specific tissue and α is the flip angle.

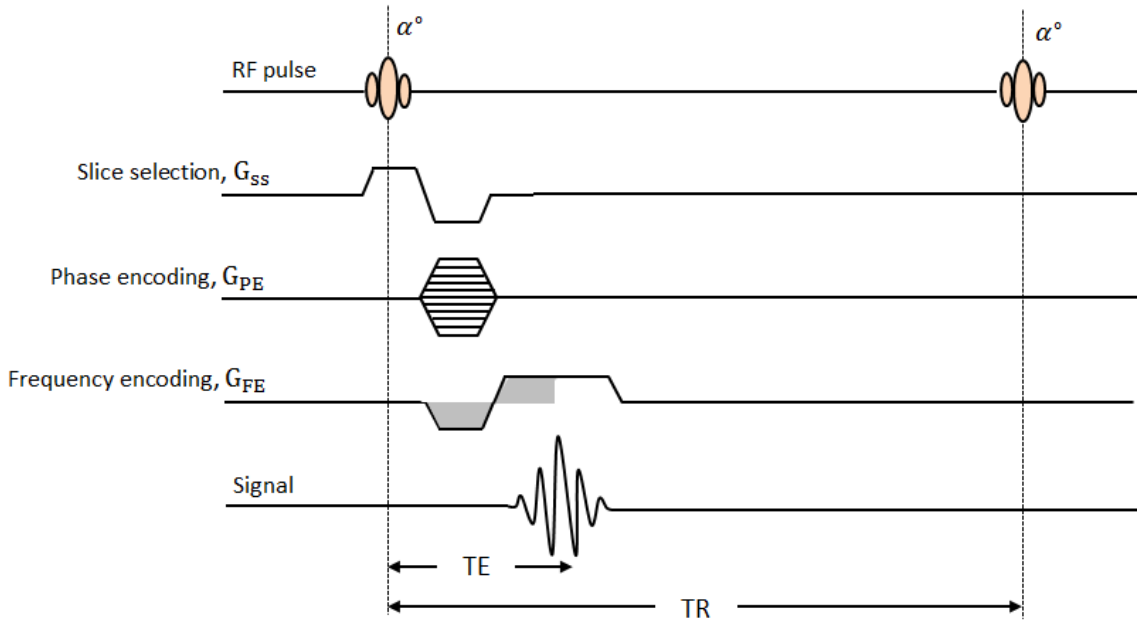

Figure 2.7: Gradient echo pulse sequence diagram (modification of [1]).

2.2.4 Effects of MR Contrast Agents

The term 'contrast agent' in the context of this work is defined as a substance administrated to a patient with the scope of adding value to medical images. Contrast agents are widely used in clinical imaging to improve sensitivity and specificity and to increase the ability to identify normal and pathological tissues. The most frequently used contrast agents for MRI are paramagnetic gadolinium-based (Gd) contrast agents. Gd injection has magnetic properties which decrease the T_1-relaxation times of surrounding water molecules and therefore T_1-weighted images have higher signal, the strength of which depends on its concentration in the tissue (the higher the concentration, the more enhanced the signal). The $T1$-relaxation times after injection of Gd can be calculated as:

$$\frac{1}{T_1(t)} = \frac{1}{T_{1,0}} + r_1[\mathrm{CA}](t), \tag{2.6}$$

where $T_1(t)$ is the longitudinal relaxation at time t of the dynamic series, $T_{1,0}$ is the baseline longitudinal relaxation time estimated prior to administration of intravenous contrast agent, r_1 is the longitudinal relaxivity of the contrast agent and $[\mathrm{CA}](t)$ is the contrast agent concentration at time t.

Gd-based contrast agent also influence and shortens T_2-relaxation times resulting in a reduced signal on T_2-weighted images.

2.3 Dynamic Contrast Enhanced MRI

In Dynamic Contrast-Enhanced MRI (DCE-MRI) we are interested in the T_1 reduction caused by the Gd. The acquisition process starts with a series of pre-contrast MR images to enable an estimate of the baseline signal. A contrast agent is then administrated as an intravenous bolus and therefore its arrival and distribution in tissue is monitored (see Figure 2.8). When Gd reaches a tissue it rapidly diffuses into the extravascular extracellular space (EES), and accumulates within the tissue causing an increase in the MR signal. The signal intensity in the tissue starts decaying until Gd is completely cleared out form the body by renal excretion. The analysis of the resulting signal intensity changes as a function of time provides valuable

information on the amount of Gd reaching particular regions, which consequently gives information on tissue perfusion. Examples of time-intensity curves obtained in DCE-MRI are shown in Figure 2.9. Moreover, the timing of such intensity variations (e.g. fast arrival of Gd and slow washout) provides further information on the tissue vascular properties.

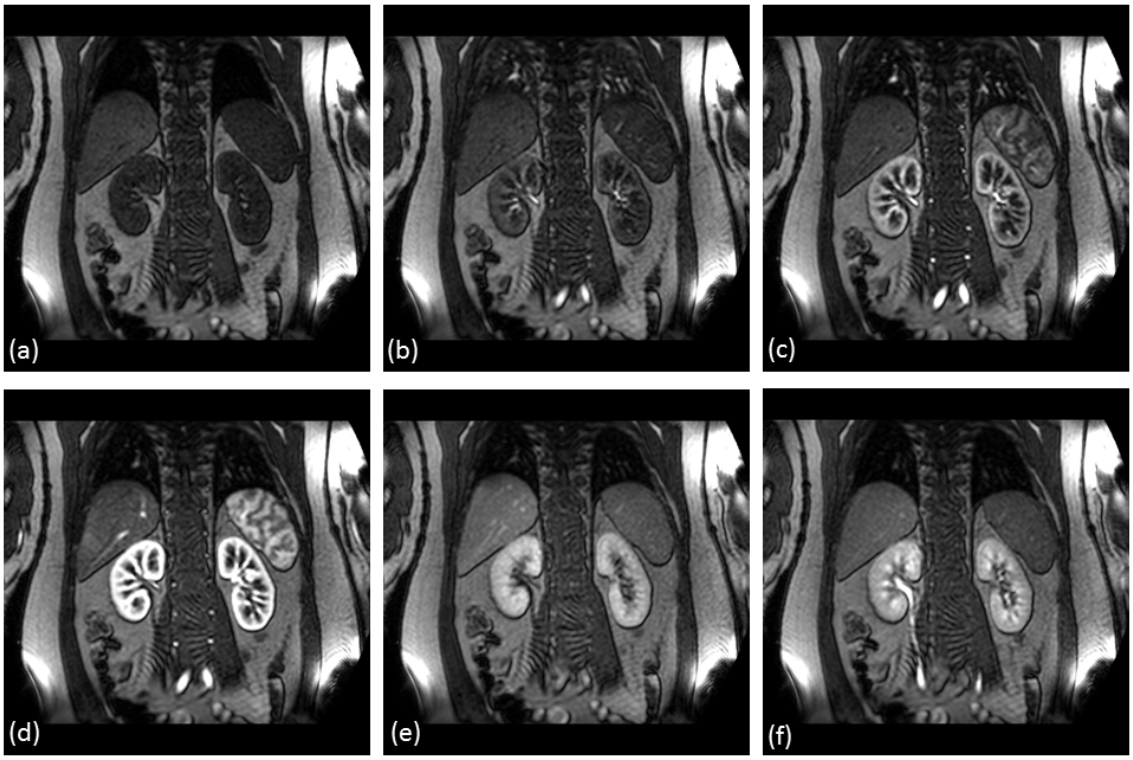

Figure 2.8: Example of DCE-MRI renal data acquired in the coronal plane. (a) pre-contrast image, (b)-(d) bolus arrival and contrast agent uptake, (e)-(f) post-contrast washout phase.

2.3.1 Conversion of Signal into Concentration

In Section 2.2.4 has been illustrated how MR signal intensities on T_1-weighted images decrease during the passage of a Gd bolus. In order to extract some more accurate and meaningful physiological information from this raw data we have to convert the MR signal intensity information into contrast agent concentration ([CA]). Even though the MR signal intensities are not directly proportional to [CA], there is a linear relationship between [CA] and the inverse of T_1 relaxation times, given by the

well-known equation [8]:

$$[\mathrm{CA}](t) = \frac{\frac{1}{T_1(t)} - \frac{1}{T_{1,0}}}{r_1}. \tag{2.7}$$

Therefore, the T_1 measurements before, during and after the injection of contrast agent provide useful information on how to quantify the actual concentration of Gd from its MR signal.

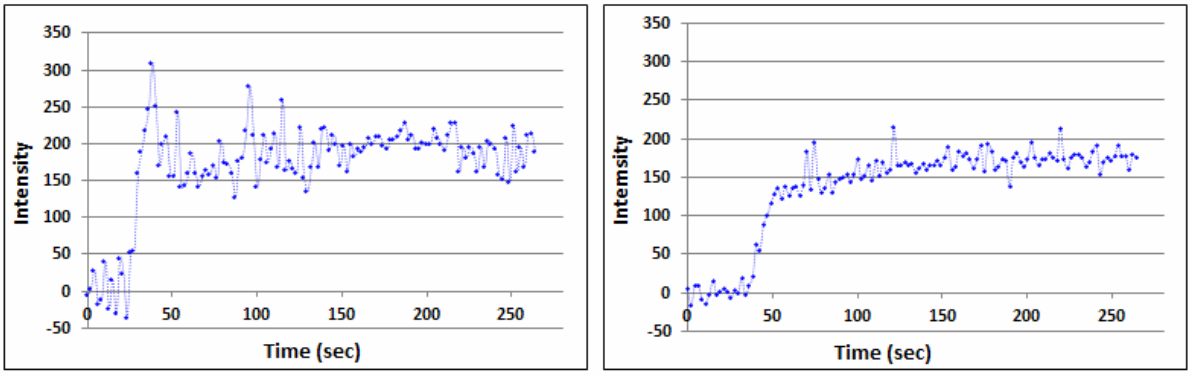

Figure 2.9: Examples of DCE-MRI time-intensity curves. The shape of the enhancement profiles show differences in the contrast agent uptake and washout reflecting the local tissue properties.

2.3.2 Quantitative Dynamic Contrast-Enhanced MRI

DCE-MRI can be assessed qualitatively or quantitatively. A quantitative analysis of DCE-MRI can be performed using mathematical models that describe the passage of a bolus of contrast agent through the tissue of interest. The concentration time series data obtained from the DCE-MRI acquisition depends on many physiological characteristics of a relevant tissue. The method used to extract the physiological tissue parameters such as blood flow and volume, capillary permeability and the volume of extravascular extracellular space is called tracer-kinetic modelling. A detailed description of tracer-kinetic modelling is given in Section 2.5.

2.4 Kidney Anatomy and Physiology

The purpose of this section is to offer an understanding of the kidney anatomy as well as further understanding of the evaluation of kidney perfusion. A number of factors influence the signal intensity of the kidney such as physiologic mechanisms of the kidney and characteristics of contrast agents. Blood flow to the kidneys is received from the abdominal aorta that branches into the left and right renal arteries. Despite their small weight of approximately 0.5% of the total body weight, the two kidneys normally receive approximately 22% of the cardiac output, that is, about 1100 ml per minute [9]. Most of the blood entering the kidneys remain in the cortex and only 1% reaches the medulla [10].

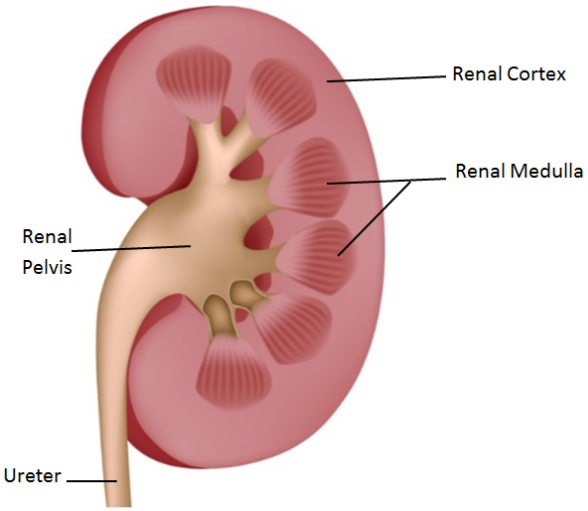

Figure 2.10: Coronal cross section of the left kidney showing the major structures.

The kidneys can be divided into three major regions: the renal cortex, the renal medulla and the renal pelvis, shown in Figure 2.10. The cortex is the outermost region of the kidney, followed by the renal medulla. The medulla is made up of 10 to 18 renal pyramids which point inward towards the pelvis. Within the renal cortex and medulla are about 800,000 to 1,000,000 nephrons, the functional unit of the kidney (see Figure 2.11). Each nephron consists of two parts: renal corpuscle and renal tubule. Blood filters by nephrons in the glomerular capillaries. Water and some solutes of blood plasma form the glomerular filtrate and flow into the Bowman's capsule which lies in the the cortex of the kidney. As the fluid enters the proximal convoluted tubule approximately two-thirds of the filtered water is

passively reabsorbed. From proximal convoluted tubule, fluid flows through the descending limb into the loop of Henle located in the medulla of the kidney. Solutes continues to remove out of the tubular fluid while returning back to the cortex through the ascending limb of the loop and the distal tubule. The distal tubule lies in the kidney cortex like the proximal tubule. The fluid leads to the collecting duct that extends to the kidney medulla, where water reabsorption depends on the level of antidiuretic hormon. The collecting ducts empty the fluid into the pelvis for extraction via papillae.

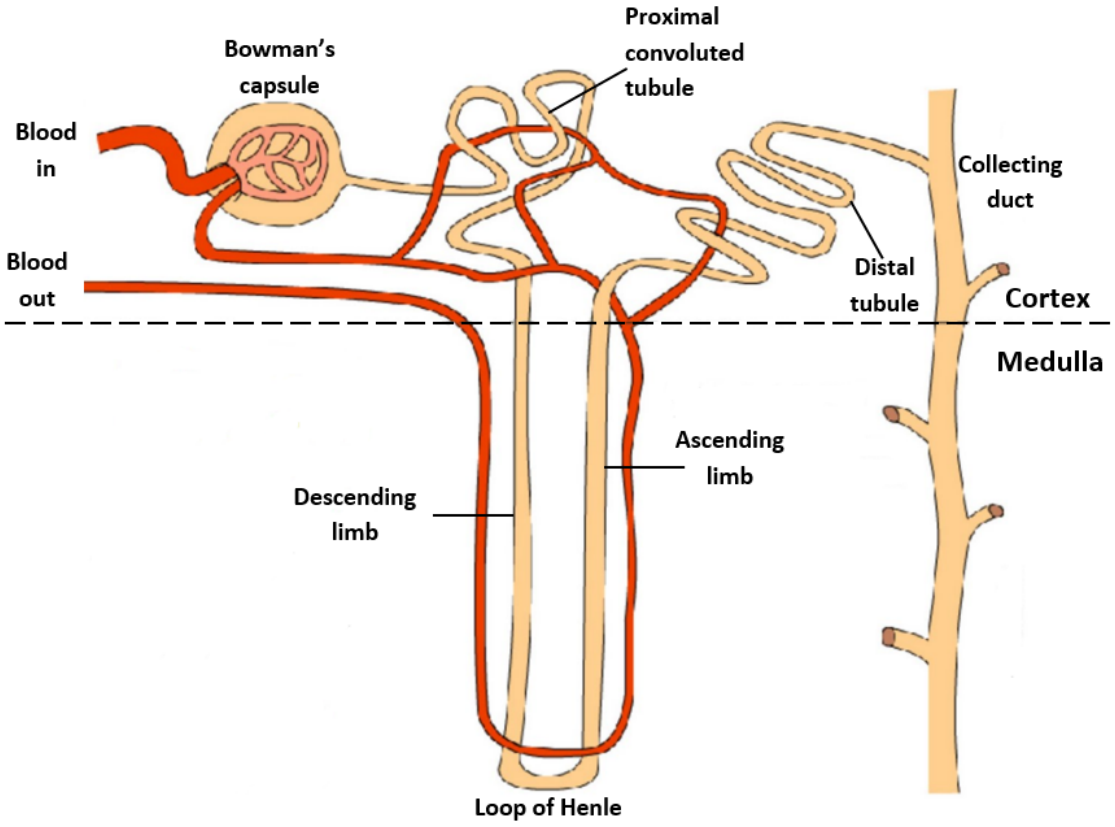

Figure 2.11: Schematic representation of the basic tubular segments of a single nephron. (The figure is a modification of Biology Animation File, URL: http://bioanimation.blogspot.co.uk/2011/07/nephronswf.html).

In the particular case of kidneys, the contrast agent first enters into the vascular space where it distributes over the vascular volume v_p. Subsequently through ultrafiltration, a fraction of the entering contrast agent is filtered out of the vascular space and is transported by the tubular flow F_T into the tubular system where it distributes over the tubular volume v_T [11]. The contrast agent is then excreted

completely from the kidneys by the outflow.

2.5 Tracer-Kinetic Modelling

Tracer-kinetic modelling is a mathematical modelling technique used to describe the distribution of contrast agent in humans and other animal species. The idea behind this technique is to treat a tissue as a compartment often composed of other subspaces/compartments. Tracer-kinetic models attempt to describe the relationship between the measurable data and the physiological parameters that affect the uptake and distribution of the contrast agent. A suitable tracer-kinetic model can account for most of the biological factors that contribute to the tissue signal. At this point it is essential to mention that the physiological tissue architecture as well as the properties of the contrast agent determine the number of compartments in which a tissue of interest can be expressed.

2.5.1 Basic Principles of Tracer-Kinetic Theory

After injection the Gd contrast agent resides immediately in plasma and diffuses due to a concentration gradient across the vascular compartment into the EES compartment, with their fractional volumes denoted as v_p and v_e, respectively. The rate of diffusion depends on the blood flow (F_p), vascular permeability (P) and vascular surface area (S) [12]. Gd based contrast agent does not leak into the intracellular space of the tissue (v_i), so its distribution volume depends on v_p and v_e. A schematic representation of compartmental modeling of a tissue is illustrated in Figure 2.12.

2.5.1.1 Tracer-Kinetic Modelling of an arbitrary tissue

Let us assume that we have a tissue with a number of inlets and outlets, which transport the contrast agent in and out of the tissue as illustrated in Figure 2.13. The tissue concentration C is equal to the amount of contrast agent in the tissue divided by the total volume of the tissue. We will define the contrast agent's volume of distribution v (in ml/100 ml) as the fraction of tissue that is accessible to the contrast agent. The contrast agent concentration c is defined as the amount of contrast agent

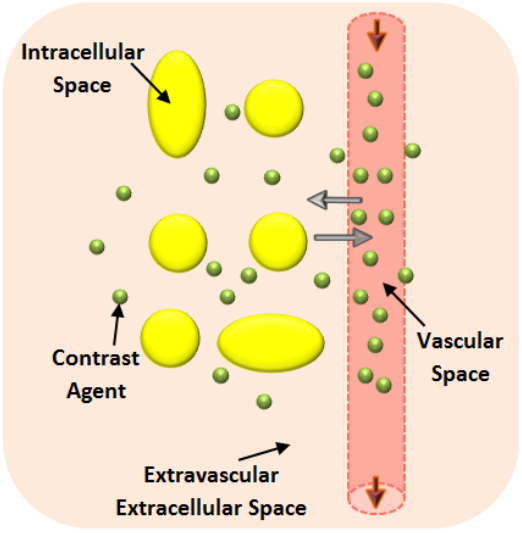

Figure 2.12: Tissue compartmentalization. The figure is a modification of the corresponding figure from [2].

in the distribution space divided by the volume that the tracer occupies, the so-called volume of distribution. The tissue concentration is then given by [13, 14]

$$C(t) = vc(t), \qquad \text{where } 0 \leq v \leq 1. \tag{2.8}$$

The amount of contrast agent that passes through an inlet or outlet per unit of time will be referred to as the flux J. For simplification, J is normalised to the tissue volume so it has units of mmol/min/100 ml [15]. The clearance, F, of an inlet or outlet is the ratio of J to the concentration c at that particular inlet or outlet [15] and is given by the following relation:

$$J(t) = Fc(t). \tag{2.9}$$

The clearance F has several physiological interpretations depending on the mechanism that transports the contrast agent: if the contrast agent is transported by convection, then F is the flow of the carrier fluid [15].

The conservation of contrast agent mass implies that no contrast agent is created or destroyed inside the tissue. In that case, the rate of change of tissue concentration $C(t)$ is given by the difference between the total inlets and outlets [13, 14]:

$$\frac{dC(t)}{dt} = \sum_{i \in \text{Inlets}} J_i(t) \; - \sum_{o \in \text{Outlets}} J_o(t), \tag{2.10}$$

where J_i and J_o denote the flux of contrast agent through an inlet and outlet, respectively.

A compartment is defined as a well mixed space where the contrast agent is uniformly distributed. The equation of mass conservation for a compartment depends on $c(t)$ and the inlet concentrations. Inserting Eqs. (2.8) and (2.9) into (2.10) we have:

$$v\frac{dc}{dt}(t) = \sum_{i \in \text{Inlets}} F_i c_i(t) \; - \sum_{o \in \text{Outlets}} F_o c_o(t). \tag{2.11}$$

A multi-compartment model can be seen as a system of $n \in \mathbb{N}$ interacting compartments, where an outlet of one compartment is the inlet of another [14]. Applying Eq. (2.11) to each of the compartments gives a system of n differential equations where the impulse response function $I(t)$ is a sum of n exponential functions [16, 17]:

$$I(t) = \sum_{i=1}^{n} A_i e^{-tB_i}. \tag{2.12}$$

This implies that in the case of one-compartment the impulse response function $I(t)$ will be a mono-exponential function.

A relationship between the inflow and outflow can be obtained through the notion of contrast agent transit time (in min). The transit time of the contrast agent is the time elapsed between entering and leaving the tissue. This link between the inflow and outflow is based on two fundamental assumptions that the system is both linear and stationary. A system is said to be linear if the response to an influx is assumed to be proportional to the contrast agent dose and it is stationary if the distribution of the transit time is independent of the time of injection. In this work, we consider a tissue with a single inlet a through which the arterial plasma flow F_p (in ml/min/100 ml) enters it. The concentration in the blood plasma of the feeding artery $c_a(t)$ is also called the arterial input function (AIF). When the assumptions of a linear and stationary tissue hold and the AIF satisfies $c_a(0) = 0$, the tissue concentration $C(t)$ is then described by a convolution (denoted by the symbol $\otimes$)

of the impulse response function $I(t)$ and the AIF:

$$C(t) = I(t) \otimes c_a(t). \tag{2.13}$$

The convolution product $f \otimes g$ of two functions $f(t)$ and $g(t)$ is defined as follows:

$$(f \otimes g)(t) = \int_0^t f(\tau)\, g(t-\tau)\, d\tau. \tag{2.14}$$

We will denote the concentration in the vascular space and EES as c_p and c_e, respectively. A mathematical expression that describes the total tissue concentration may be obtained by applying Eq.(2.10) to all of the compartments comprising the model, to result into:

$$C(t) = v_p c_p(t) + v_e c_e(t). \tag{2.15}$$

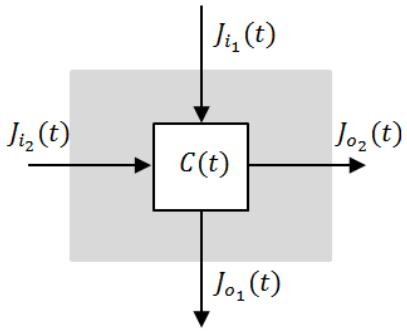

Figure 2.13: Schematic representation of an arbitrary system. The system has two inlets (J_{i_1} and J_{i_2}) and two outlets (J_{o_1} and J_{o_2}).

2.5.2 Tracer-Kinetic Models

Extracting the physiologic characteristics of tissue from DCE-MRI can be done through tracer-kinetic modelling. This approach was first introduced by Kety [18] in the context of general gas exchange in the lungs and was subsequently used by Crone [19] in the context of contrast agent diffusion. Models developed in the early

90s have become a standard in many applications. While simpler models describe only the amount of contrast agent that flows into the kidneys, other more complex models describe the tubular outflow with one or more compartments. An overview of some of these models is given below.

2.5.2.1 Definitions and Notations

Before introducing some of the standard tracer-kinetic models, it is essential to introduce some definitions and notations. Let the mean transit time in the vascular and tubular compartments be denoted as T_p and T_T, respectively. T_p and T_T measure how long it takes for the contrast agent molecule to pass through the plasma and tubules (in min), respectively. Extraction fraction (E) measures how much of the blood plasma delivered to the tissue is filtered out by the glomeruli (in %). Let us denote the concentration of the contrast agent in the arterial and tubular space as $c_a(t)$ and $c_T(t)$, respectively. One should note that the central volume theorem provides a fundamental relation between the parameters characterising the vascular space [17]:

$$F_p = v_p/T_p. \tag{2.16}$$

2.5.2.2 Two-compartment filtration model (2CFM)

The two-compartment filtration model (2CFM) divides the kidney into two compartments, the vascular and tubular compartment, see Figure 2.14(a). The total tissue concentration is then given by

$$C(t) = v_p c_p(t) + v_T c_T(t). \tag{2.17}$$

As introduced in Section 2.5.1.1 the change of tracer mass in the tubular compartment is the difference between the concentration that flows into the tubular compartment from the vascular compartment and the concentration that flows out. The mass balance equation of the tubular space then amounts to:

$$v_T \frac{dc_T(t)}{dt} = F_T c_p(t) - F_T c_T(t). \tag{2.18}$$

Here we defined:

$$F_T = v_T/T_T, \tag{2.19}$$

where F_T denotes the tubular flow.

A similar expression can be also derived by expressing the conservation of tracer mass in the vascular compartment:

$$v_p \frac{dc_p(t)}{dt} = F_p c_a(t) - F_p c_p(t). \tag{2.20}$$

Because the transit times in a compartment are exponentially distributed [17], the vascular concentration can be expressed as:

$$c_p(t) = T_p^{-1} e^{-t/T_p} \otimes c_a(t). \tag{2.21}$$

Solving Eq.(2.18) for $c_T(t)$ leads to the following convolution equation:

$$c_T(t) = T_T^{-1} e^{-t/T_T} \otimes c_p(t). \tag{2.22}$$

Substituting Eq.(2.21) into Eq.(2.22) results in:

$$c_T(t) = \frac{1}{T_p T_T} e^{-t/T_p} \otimes e^{-t/T_T} \otimes c_a(t). \tag{2.23}$$

Substituting $c_p(t)$ and $c_T(t)$) into Eq.(2.17), the total tissue concentration leads to:

$$C(t) = \left(\frac{v_p}{T_p} e^{-t/T_p} + \frac{v_T}{T_p T_T} e^{-t/T_p} \otimes e^{-t/T_T} \right) \otimes c_a(t) \tag{2.24}$$

The 2CFM is defined by the Eq.(2.24), which is completely determined by the four parameters T_p, T_T, v_p and v_T.

2.5.2.3 Modified Tofts model

The modified Tofts model is one of the most widely used models in T_1-weighted DCE-MRI analysis. It was originally developed for use in the brain with a relatively low temporal resolution [20]. This model states that the contrast agent resides in and exchanges between two compartments in the tissue: the vascular space and the EES, see Figure 2.14(b). With the additional assumption that the concentration in the vascular space, c_p, is equal to the concentration at the arterial input throughout the tissue:

$$c_p(t) = c_a(t). \tag{2.25}$$

Eq.(2.18) then becomes:

$$v_T \frac{dc_T(t)}{dt} = F_T c_a(t) - F_T c_T(t). \tag{2.26}$$

One can solve this equation for c_T to find

$$c_T(t) = T_T^{-1} e^{-t/T_T} \otimes c_a(t). \tag{2.27}$$

Similar to the 2CFM the total tissue concentration is given by Eq.(2.17). Thus, substituting Eqs. (2.25) and (2.27) into Eq.(2.17), leads to:

$$C(t) = v_p c_a(t) + \frac{v_T}{T_T} e^{-t/T_T} \otimes c_a(t). \tag{2.28}$$

The modified Tofts model does not allow for the measurement of plasma flow, F_p. Instead, the three fitted parameters are the v_p, v_T and T_T. The modified Tofts model is only valid in tissues with a relatively high flow.

2.5.2.4 Tofts Model

Tofts et al. [20] firstly proposed a one-compartment model commonly known as the Tofts model. The Tofts model describes the transfer of contrast agents between the capillaries and the EES. The assumption underlying this model is that the vascular compartment is assumed to have a negligible contribution to the total tissue

concentration, i.e. $v_p = 0$ (Figure 2.14(c)). This leads to the following relation:

$$C(t) = v_T c_T(t). \tag{2.29}$$

Substituting Eq.(2.22) into (2.29) leads to:

$$C(t) = \frac{v_T}{T_T} e^{-t/T_T} \otimes c_p(t). \tag{2.30}$$

The total concentration in tissue is defined by Eq.(2.30), which is completely determined by the two parameters v_T and T_T.

2.5.2.5 Two-compartment Exchange Model (2CXM)

The two-compartment exchange model (2CXM) features four parameters, see Figure 2.14(d). The contrast agent transport through plasma compartment and its exchange in the capillaries with the EES. The exchange of contrast agent between the two compartments is assumed to be symmetric and is quantified by the PS [21]. The total tissue concentration is given by:

$$C(t) = v_p c_p(t) + v_e c_e(t). \tag{2.31}$$

The plasma space and EES are both modeled as well mixed compartments. The mass conservation for extravascular compartment then reads:

$$v_e \frac{dc_e(t)}{dt} = PS(c_p(t) - c_e(t)). \tag{2.32}$$

A similar expression can also be derived by expressing the concentration of tracer mass in the vascular compartment:

$$v_p \frac{dc_p(t)}{dt} = F_p(c_a(t) - c_p(t)) + PS(c_e(t) - c_p(t)). \tag{2.33}$$

The differential equations stated above can be written as a nonhomogeneous system

of the form:

$$\mathbf{u}'(t) = \mathbf{J}\mathbf{u}(t) + \mathbf{g}(t), \tag{2.34}$$

where $\mathbf{J}$ is an $n \times n$ constant matrix and $\mathbf{g}(t)$ is an $n \times 1$ vector. The general solution of the differential equation (2.34) takes the form [22]:

$$\mathbf{u}(t) = \mathbf{W}(t)\mathbf{c} + \mathbf{W}(t) \int_{t_0}^{t} \mathbf{W}^{-1}(s)\mathbf{g}(s)\, ds, \quad \text{for any } \mathbf{c} \in \mathbb{R}^n. \tag{2.35}$$

Using Eqs. (2.32) and (2.33) lead to the following system of equations (writing $c_e'(t)$ for the time derivative of $c_e(t)$):

$$\begin{pmatrix} c_e'(t) \\ \\ c_p'(t) \end{pmatrix} = \begin{pmatrix} \dfrac{-PS}{v_e} & \dfrac{PS}{v_e} \\ \\ \dfrac{PS}{v_p} & -\dfrac{(PS+F_p)}{v_p} \end{pmatrix} \begin{pmatrix} c_e \\ \\ c_p \end{pmatrix} + \begin{pmatrix} 0 \\ \\ \dfrac{F_p}{v_p} c_a(t) \end{pmatrix}. \tag{2.36}$$

The discriminant (Δ) of the above system is equal to:

$$\Delta = \left(\frac{v_e F_p + PS(v_e - v_p)}{v_e v_p} \right)^2 + \frac{4PS^2}{v_e v_p} > 0. \tag{2.37}$$

We then find the eigenvalues of the matrix $\mathbf{J}$ given by:

$$\lambda_{1,2} = \frac{1}{2} \left[\left(\frac{F_p}{v_p} + \frac{PS}{v_p} + \frac{PS}{v_e} \right) \pm \sqrt{\Delta} \right], \tag{2.38}$$

and the corresponding eigenvectors:

$$\mathbf{v_{1,2}} = \begin{pmatrix} 1 \\ \\ \dfrac{v_e}{PS}\lambda_{1,2} + 1 \end{pmatrix}. \tag{2.39}$$

Thus the basic solutions of the homogeneous system are

$$\mathbf{u_{1,2}}(t) = e^{\lambda_{1,2}(t)} \begin{pmatrix} 1 \\ \\ \dfrac{v_e}{PS}\lambda_{1,2} + 1 \end{pmatrix}. \tag{2.40}$$

The matrix $W(t)$ can then constructed from the solutions $\mathbf{u_{1,2}}(t)$:

$$\mathbf{W}(t) = \begin{pmatrix} e^{\lambda_1 t} & e^{\lambda_2 t} \\ \\ e^{\lambda_1 t}\left(\dfrac{v_e}{PS}\lambda_1 + 1\right) & e^{\lambda_2 t}\left(\dfrac{v_e}{PS}\lambda_2 + 1\right) \end{pmatrix}. \tag{2.41}$$

The inverse of $\mathbf{W}(t)$ equals to:

$$\mathbf{W}^{-1}(t) = \frac{PS}{v_e}\frac{1}{\lambda_2 - \lambda_1} \begin{pmatrix} \left(\dfrac{v_e}{PS}\lambda_2 + 1\right)e^{-\lambda_1 t} & -e^{-\lambda_1 t} \\ \\ -\left(\dfrac{v_e}{PS}\lambda_1 + 1\right)e^{-\lambda_2 t} & e^{-\lambda_2 t} \end{pmatrix}. \tag{2.42}$$

We assume $c_p(0) = c_e(0) = c_a(0) = 0$ which leads to the initial condition

$$\mathbf{u}(0) = 0. \tag{2.43}$$

Finally, substituting for $\mathbf{W}^{-1}(s)\mathbf{g}(s)$ and $\mathbf{W}(t)$ in Eq.(2.35) gives the solution $\mathbf{u}(t)$ of the system (2.34):

$$\mathbf{u}(t) = \begin{pmatrix} A\displaystyle\int_0^t e^{\lambda_1(t-s)}c_a(t)\,ds + A\int_0^t e^{\lambda_2(t-s)}c_a(t)\,ds \\ \\ AB_1\displaystyle\int_0^t e^{\lambda_1(t-s)}c_a(t)\,ds + AB_2\int_0^t e^{\lambda_2(t-s)}c_a(t)\,ds \end{pmatrix}, \tag{2.44}$$

where $A = \dfrac{PSF_p}{v_e v_p}\dfrac{1}{\lambda_2 - \lambda_1}$, $B_1 = \lambda_1\dfrac{v_e}{PS} + 1$ and $B_2 = \lambda_2\dfrac{v_e}{PS} + 1$.

Hence the c_e and c_p can be expressed as:

$$c_e(t) = \left(\frac{PSF_p}{v_e v_p} \left(\frac{e^{\lambda_1 t} + e^{\lambda_2 t}}{\lambda_2 - \lambda_1} \right) + \frac{F_p}{v_p} \left(\frac{\lambda_1 e^{\lambda_1 t} + \lambda_2 e^{\lambda_2 t}}{\lambda_2 - \lambda_1} \right) \right) \otimes c_a(t), \tag{2.45}$$

$$c_p(t) = \frac{PSF_p}{v_e v_p} \left(\frac{e^{\lambda_1 t} + e^{\lambda_2 t}}{\lambda_2 - \lambda_1} \right) \otimes c_a(t). \tag{2.46}$$

Substituting $c_p(t)$ and $c_e(t)$ into Eq.(2.31), the total tissue concentration leads to:

$$C(t) = F_p \left(\frac{PS(v_p + v_e)}{v_e v_p} \left(\frac{e^{\lambda_1 t} + e^{\lambda_2 t}}{\lambda_2 - \lambda_1} \right) + \frac{v_e}{v_p} \left(\frac{\lambda_1 e^{\lambda_1 t} + \lambda_2 e^{\lambda_2 t}}{\lambda_2 - \lambda_1} \right) \right) \otimes c_a(t). \tag{2.47}$$

The 2CXM is defined by Eq.(2.47) which is completely determined by the four parameters F_p, v_p, v_e and PS.

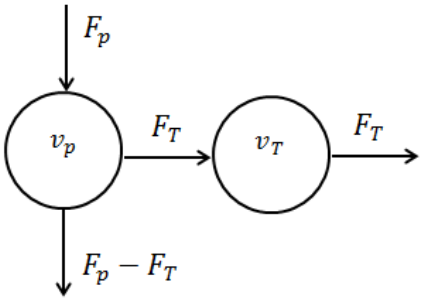

(a)

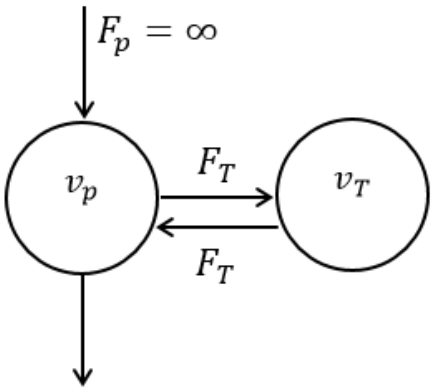

(b)

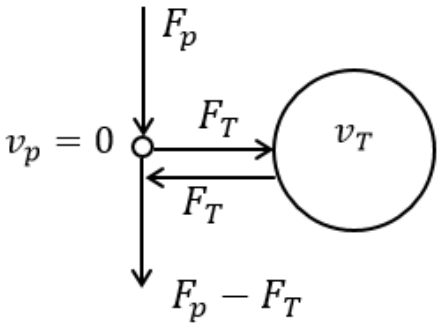

(c)

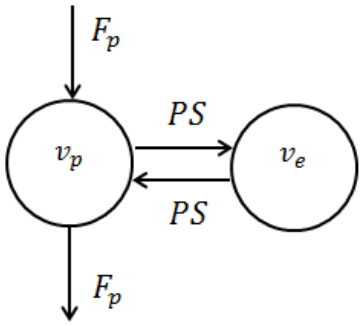

(d)

Figure 2.14: Tracer kinetic models: (a) Two-compartment filtration model, (b) Modified Tofts model and (c) Tofts model and (d) Two-compartment exchange model.

2.5.3 Arterial Input Function in Tracer-Kinetic Modelling

Tracer-kinetic models require an AIF to provide information on the arrival and delivery of the bolus to tissue, see Figure 2.15. As mentioned previously, the parameters extracted form tracer-kinetic modelling of tissue response to contrast agent passage are used to evaluate the response to treatment of malignant tumors. Hence, reliable model fitting to produce accurate parameter values is important in clinical diagnosis, prognosis and therapy. In order to achieve reproducible model fitting, accurate representation of the AIF describing the arrival and the way the contrast agent bolus is transmitted along the local arteries and network of arterioles is essential. The AIF may be estimated either by average inputs from experimentally derived input functions [23] or by using standard functional forms [24]. In addition several techniques have been developed based on automatic selection of the AIF [25, 26].

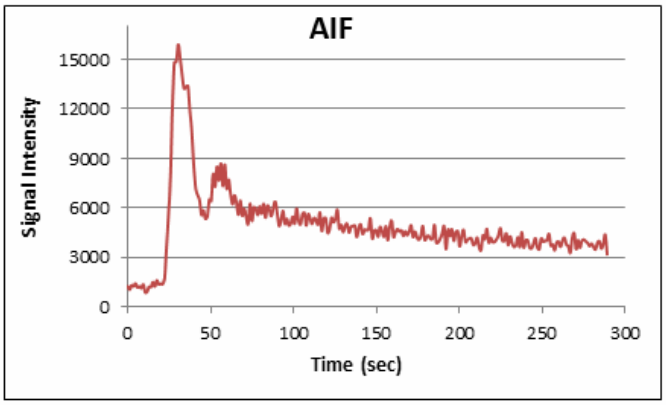

Figure 2.15: Example of AIF.

2.6 Image Registration

Image registration is the process of finding a coordinate transformation that spatially aligns two or more images. This process involves designating one image that is not change during registration, called target image and applying geometric transformations to the other image, called source image, so that it aligns with the target. The image which is made increasingly similar to the target image is called motion corrected image and is defined as:

$$I_{\text{corr}}(\mathbf{x}) = I_{\text{source}}(\mathbf{T}\big(\mathbf{x}\big)\big), \tag{2.48}$$

where $I_{\text{corr}}(\mathbf{x})$ and $I_{\text{source}}(\mathbf{x})$ is the intensity of motion corrected image and source image in position $\mathbf{x}$, and $\mathbf{T}(\mathbf{x})$ is the transformation to be identified.

Image registration can be defined between images acquired by the same imaging modality (mono-modal) or between images acquired by two different types of modalities (multi-modal) such as the registration of an MR image to a PET image. Registration algorithms can be classified into two main categories: feature-based and intensity-based. In feature-based registration methods a pre-processing step is required to extract geometrical features from one image and then match them with their counterparts in the second image. These features can either be extracted from contours of anatomical structures or corner points, or from markers with known locations [27]. An advantage of these methods is their dimensionality reduction which consequently reduces the computational time. However, a key limitation of using this type of methods is the dependence of the registration process on the feature extraction pre-processing step. As opposed to feature-based methods, intensity-based registration methods align images directly based on their pixel intensity values. Thus, a key advantage of this type of methods is that the registration process uses all the available image information and does not rely on any pre-processing step [27]. A downside of intensity-based methods is that they are based solely on intensities and currently remain a great challenge for multi-modal image registration where the images to be registered have totally different intensity distributions.

A registration algorithm usually contains three main components: the transformation model, the similarity measure and the optimisation method. An overview of the main components of medical image registration can be found below.

2.6.1 Transformation Model

The first component of an image registration algorithm is the transformation model. As mentioned above, the transformation model defines the set of transformations that is required to spatially align the I_{corr} with I_{target}. The number of parameters needed to describe a transformation are often called degrees of freedom. The number of degrees of freedom depends on the type of the transformation and on the dimensionality of the images. The most well-known types of transformations are rigid, affine and non-rigid. Rigid transformations allow only translation and rotation, see Figure 2.16. Affine transformations increase registration flexibility since they include rigid transformation plus scaling and shearing, see Figure 2.16. Non-rigid registration is the most interesting and challenging work in image registration today. Non-rigid transformations can account for more general deformations as it allows to the object to deform, at the cost of increased complexity. Among the most important families of geometric transformations, one may cite transformations derived from interpolation theory. One of the most important families inspired by interpolation theory is that of Free-Form Deformations (FFD). In the particular case of FFD, the transformation function in Eq.(2.48), defines how to transform pixel coordinates in the source image to match pixel coordinates in the target image. This type of information is usually stored in the so called deformation field. A deformation field is formally a vectorial function $\mathbf{d} : \Omega \rightarrow \mathbb{R}^{2,3}$, on the image domain Ω and is usually used in the transformation function. An example of a deformation field can be seen in Figure 2.17. At a spatial location $\mathbf{x} = (x, y, z)$, the transformation function of a FFD is of the general form [28]:

$$\mathbf{T}(\mathbf{x}) = \mathbf{x} + \mathbf{d}(\mathbf{x}), \qquad \mathbf{x} \in \Omega. \tag{2.49}$$

2.6.1.1 Free-Form Deformations

In recent years, transformation models using FFD have gained significant popularity in registration of medical images. Sederberg and Parry [29] first described the concept of FFD as a powerful modelling tool which can be used to represent complex deformations. The basic idea of the FFD is to deform an image by manipulating an underlying mesh of control points that are distributed throughout the image, pro-

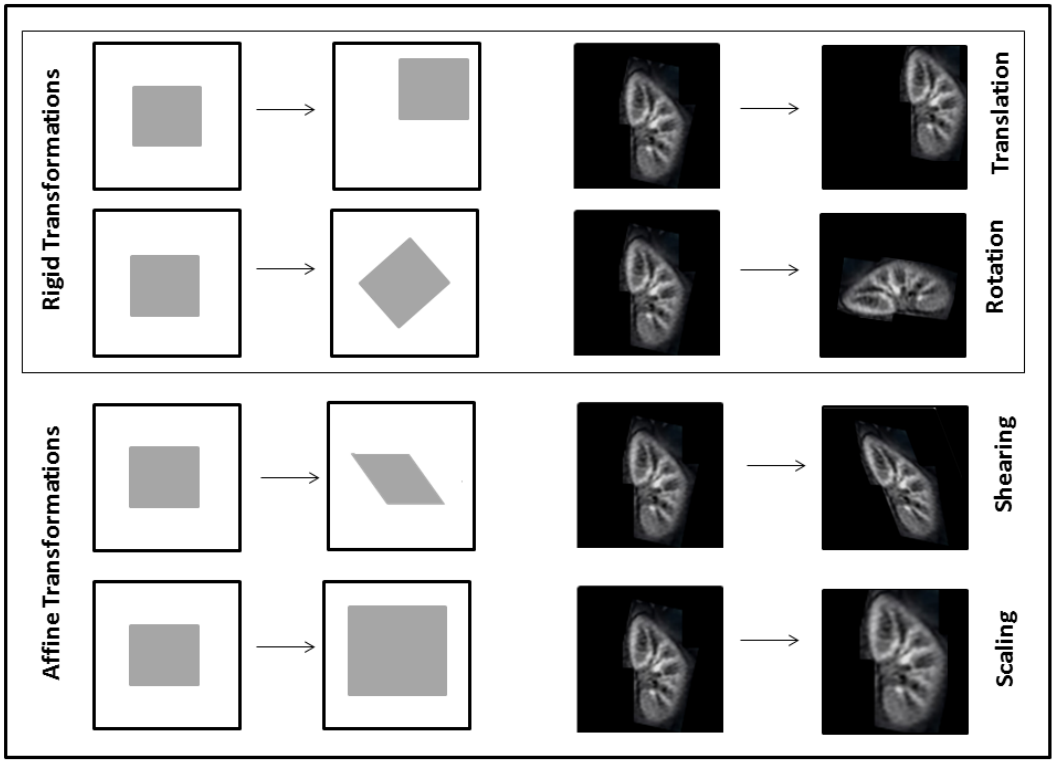

Figure 2.16: Examples of 2D rigid and affine transformations.

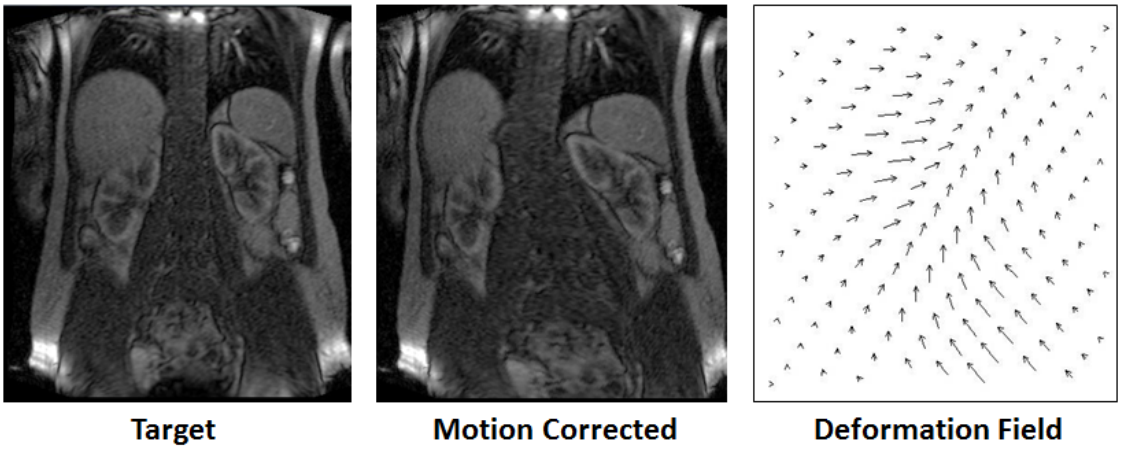

Figure 2.17: The deformation field gives for every pixel location in the motion corrected image the direction and distance how it has to move in order to match the target image.

ducing a smooth transformation. This requires a regular mesh of uniformly spaced control points. The locations of the individual pixels between the control points is computed from the positions of the neighboring control points.

To define an FFD, let us denote the image domain as the rectangle $\Omega = \{(x, y, z)|0 \leq x < X, 0 \leq y < Y, 0 \leq z < Z\}$. When image Ω is deformed, its shape can be represented by the vectorial function, $\mathbf{d}$. Let $n_x \times n_y \times n_z$ be a mesh of control points with uniform spacing δ overlaid on image Ω. In the initial configuration of the said mesh, the ijk^{th} control point is at its initial position, i.e. $\mathbf{d}_{ijk} = (i, j, k)$. The deformation field is then defined as:

$$\mathbf{d}(\mathbf{x}) = \sum_{i,j,k \in I_\Phi} W_{i,j,k}(\mathbf{x}) \mathbf{d}_{i,j,k}, \tag{2.50}$$

where I_Φ is an N-dimensional discrete array representing the set of all control point coordinates in the image and $W_{i,j,k}$ is a weighting function which equals to 1 in the control point at location i, j, k and equals to 0 in the other control points.

2.6.1.2 Splines

Originally, splines were devised to model ships and planes using long flexible strips of wood or metal, i.e. the splines. The strips were bent to the desired shape by applying a set of weights at specific positions. In spline based image transformations the applied weights correspond to the displacement of a specific point. Nowadays, splines in conjunction with FFD are widely applied in many image registration techniques which use splines based transformation model.

2.6.1.3 B-Splines Parametrisation

FFD gained wide acceptance in the medical image registration when coupled with B-splines [30, 31, 32]. Rueckert et al. [30] first proposed the use of FFD based on B-splines which is most frequently cited as the reference of FFD based image registration. In the case of B-splines based image registration, the dense deformation field is parametrised by a sparse set of control points, resulting in the formation of two grids: a dense grid and a sparse control point grid [33]. Similarly to Eq.(2.50),

the deformation field is given according to [30, 34, 35] as:

$$\mathbf{d}_{\text{cubic}}(\mathbf{x}) = \sum_{l=0}^{3}\sum_{m=0}^{3}\sum_{n=0}^{3} B_l(u)B_m(v)B_n(w)\mathbf{d}_{i+l,j+m,k+n}, \tag{2.51}$$

where $i = \lfloor \frac{x}{n_x} \rfloor - 1$, $j = \lfloor \frac{y}{n_y} \rfloor - 1$, $k = \lfloor \frac{z}{n_z} \rfloor - 1$, $u = x/n_x - \lfloor \frac{x}{n_x} \rfloor$, $v = y/n_y - \lfloor \frac{y}{n_y} \rfloor$, $w = z/n_z - \lfloor \frac{z}{n_z} \rfloor$, and $B_l(u)$ are the uniform B-spline basis functions evaluated at u. They are defined as:

$$\begin{aligned} B_0(u) &= (1-u)^3/6 \\ B_1(u) &= (3u^3 - 6u^2 + 4)/6 \\ B_2(u) &= (-3u^3 + 3u^2 + 3u + 1)/6 \\ B_3(u) &= u^3/6. \end{aligned}$$

The basis functions for $B_m(v)$ and $B_n(w)$ are defined similar. B-splines are locally controlled and have a limited support which makes them computationally efficient even for a large number of control points [30]. That is, changing a control point affects the transformation only the in neighborhood of the particular control point. In case of cubic B-splines this neighborhood consists of 16 control points in 2D case and 64 control points in 3D case.

A FFD could also be formulated as a summation of linear B-splines instead of cubic B-splines. In case of linear B-splines the displacement field simplifies to:

$$\mathbf{d}_{\text{linear}}(\mathbf{x}) = \sum_{l=0}^{1}\sum_{m=0}^{1}\sum_{n=0}^{1} B_l(u)B_m(v)B_n(w)\mathbf{d}_{i+l,j+m,k+n}, \tag{2.52}$$

where the uniform B-spline basis functions $B_l(u)$ are defined as:

$$\begin{aligned} B_0(u) &= (1-u) \\ B_1(u) &= u. \end{aligned}$$

In case of linear B-splines transformation function the neighborhood consists of 4 control points in 2D case and 8 control points in 3D case.

2.6.1.4 Bilinear Interpolation

In the particular case of 2D image registration, the current implementation of the proposed registration algorithm is based on bilinear interpolation. Interpolation is required during the registration iterations to interpolate the dense deformation grid according to the sparse control point grid. Bilinear interpolation considers the closest 2×2 neighborhood of known pixel values surrounding the unknown pixel [36]. Let us assume that we want to find the displacement of the point P at an arbitrary location (x, y). Suppose we know the value of the displacement $\mathbf{d}$ at the four points (x_i, y_j), (x_i, y_{j+1}), (x_{i+1}, y_j) and (x_{i+1}, y_{j+1}), as shown in Figure 2.18. The interpolation formula by definition is given by:

$$\mathbf{d}_{\text{linear}}(x,y) = (1-u)(1-v)\,\mathbf{d}_{i,j} + u(1-v)\,\mathbf{d}_{i+1,j} + (u-1)v\,\mathbf{d}_{i,j+1} + uv\,\mathbf{d}_{i+1,j+1}. \quad (2.53)$$

For reasons of consistency Eq.(2.53) can be written as follows:

$$\mathbf{d}_{\text{linear}}(x,y) = p\,\mathbf{d}_{i,j} + q\,\mathbf{d}_{i+1,j} + r\,\mathbf{d}_{i,j+1} + s\,\mathbf{d}_{i+1,j+1}, \quad (2.54)$$

where p, q, r and s are defined as follows:

$$\begin{aligned} p &= (1-u)(1-v), \\ q &= u(1-v), \\ r &= (1-u)v, \\ s &= uv. \end{aligned}$$

2.6.2 Similarity Measures

The second component of a registration algorithm is the similarity measure. The similarity measure compares the target image and the motion corrected image and measure how different these are. The motion corrected image is the image which is made increasingly similar to the target image, as defined in Eq.(2.48). The choice of the similarity measure depends on the modality of the images to be registered. The

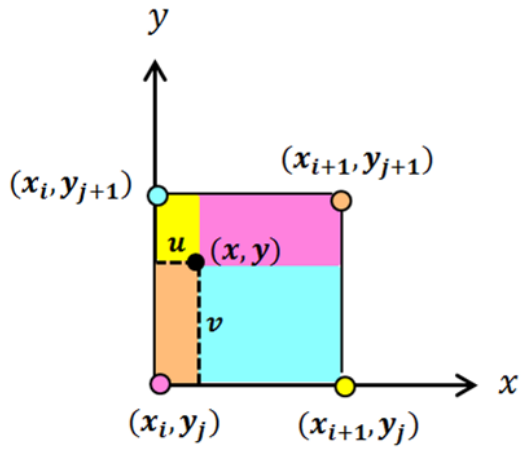

Figure 2.18: Geometric visualisation of bilinear interpolation on a unit square.

most popular for registration of mono-modal images are Sum of Squared Differences (SSD) and Cross-correlation. These similarity measures are based on the assumption that similar anatomical structures in the two images have similar intensities [37]. Mutual information and normalised mutual information are commonly used for registration of multi-modal images. In this case the assumption that similar structures share similar intensity values is not valid [37].

The registration algorithm presented in this thesis is targeted at mono-modal image registration problem. The similarity measure used in the algorithm is based on the SDD. The SDD method is widely used in image registration due to its simplicity and it relies on the fact that similar structures share similar intensity values on the two images I_{target} and I_{corr}, i.e.:

$$\text{SSD}(I_{\text{target}}, I_{\text{corr}}) = \sum_{\mathbf{x}\in\Omega} \Big(I_{\text{target}}(\mathbf{x}) - I_{\text{corr}}\big(\mathbf{T}(\mathbf{x})\big) \Big)^2, \tag{2.55}$$

where $I_{\text{target}}(\mathbf{x})$ is the intensity of the target image in position $\mathbf{x}$.

2.6.3 Optimisation Method

The last component of a registration algorithm is the optimisation method. The optimisation approach can be viewed as the connection between the transformation model and the similarity measure. The transformation that relates the target image

and the motion corrected image is estimated by iteratively minimising the cost function to find the optimum match between the two images. This procedure can be formulated as a minimisation problem:

$$\hat{\mathbf{d}}(\mathbf{x}) = \arg\min_{\mathbf{d}} \mathcal{C}\big(I_{\text{target}}(\mathbf{x}), I_{\text{corr}}(\mathbf{x})\big), \tag{2.56}$$

where $\hat{\mathbf{d}}$ denotes the optimal solution and the cost function $\mathcal{C}$ equals the similarity metric.

In order to define the optimal set of parameters $\hat{\mathbf{d}}$ an iterative optimisation approach is employed, of the general form:

$$\mathbf{d}_{k+1} = \mathbf{d}_k + a_k \mathbf{s}_k, \qquad k = 0, 1, 2, \ldots \tag{2.57}$$

with $\mathbf{s}_k$ represents the search direction at iteration k and $a_k > 0$ is a scalar factor controlling the step size along the search direction. Several optimisation techniques have been proposed in the literature [38, 39], usually they differ in the way they compute the a_k and $\mathbf{s}_k$. Standard optimisation approaches are Gradient Descent, Conjugate Gradient and Quasi-Newton method. Evaluation of optimisation methods is beyond the scope of this work. An extensive review of optimisation methods for medical image registration can be found in [40]. The process of the optimisation approach is illustrated in Figure 2.19.

A gradient descent method is implemented in this work [39]. This method takes steps in the direction of the negative gradient of the cost function:

$$\mathbf{d}_{k+1} = \mathbf{d}_k - a_k G(\mathbf{d}_k), \tag{2.58}$$

where $G(\mathbf{d}_k)$ is the derivative of the cost function evaluated at the current position $\mathbf{d}_k$.

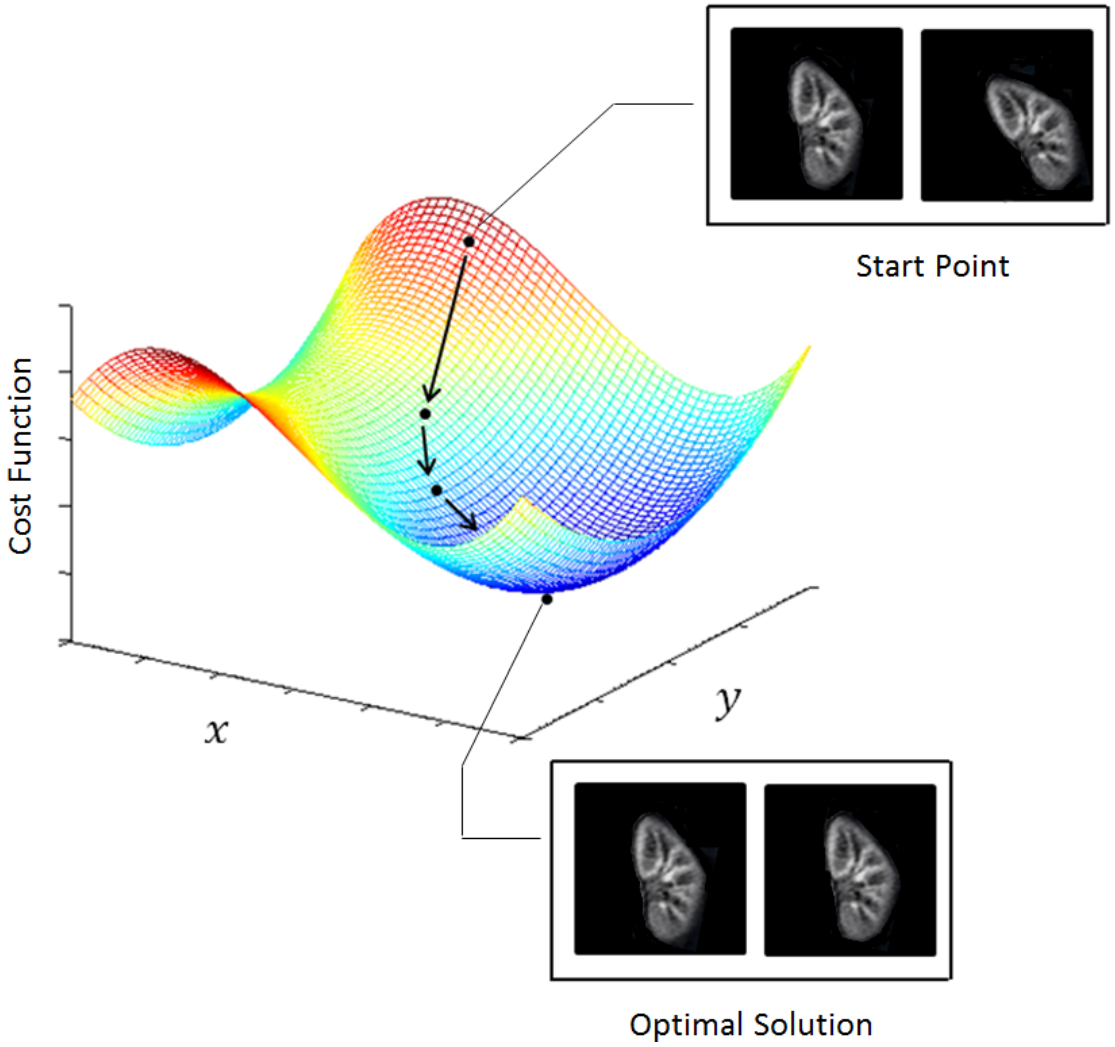

Figure 2.19: Iterative optimisation approach: The start point at the top of the graph with high cost function value represents the images before registration. The optimal solution corresponds to the point at the bottom of the graph with minimum cost function value. The arrows represent the series of iterative steps taken in order to find the minimum.

2.6.3.1 Multiresolution Strategy

A multiresolution strategy is a step by step hierarchical approach, in which the registration process starts on a level with reduced complexity, then continuing to levels with increased complexity, until the desired level is reached [41]. To reduce complexity two approaches are distinguished: reduction of data complexity (i.e. downsampled images) and reduction of transformation complexity. This work focus on multiresolution approach that reduce the transformation complexity. A detailed description of the multiresolution strategies can be found in [42].

In order to reduce transformation complexity it is common to start the registration process with fewer degrees of freedom for the transformation model. In the particular case of FFD the degrees of freedom equals the number of elements of the deformation field, i.e. the number of control points. Several types of deformations can be occur to a tissue. In a series of images that need to be registered there can be movement on a relatively large scale such as breathing or movement on a relatively small scale such as heartbeat. Large deformations between the images to be registered can be modeled with a comparatively coarse control point grid (i.e. small number of control points). On the other hand, small deformations will hardly be reconstructed since few control points have to move over relatively small distances. Thus, to take advantage of both coarse and fine control point grid the registration first run on the coarsest resolution in order to capture large deformations and then the resolution of the grid is constantly increasing to account for small deformations. At each resolution level of the grid an interpolation method takes place. The control point grid obtained from the previous coarser level is interpolated to initialise the next finer control point grid. In the current implementation of the registration algorithm presented in this thesis a bilinear and trilinear interpolations are used. Although this technique improves the convergence of the registration and reduces the computation time, it should be obvious that the computational complexity increases with the transformation complexity, i.e. the resolution of the control point grid.

2.6.4 Motion Correction of DCE-MRI data

As mentioned previously, DCE-MRI data are collected over a period of minutes in order to monitor the uptake and washout of the contrast agent in tissues. Thus, various sources of patient motion affect its performance during the image acquisition

and cause inter-frame misalignments. Abdominal DCE-MRI is mainly affected by respiratory motion. The magnitude of motion due to breathing of abdominal organs such as the liver, kidneys and spleen has been observed to be about 15 mm under normal breathing conditions along the superior-inferior axis [43]. Such movements significantly reduce the accuracy of DCE-MRI analysis and image registration is thus required. A major challenge of the image registration in DCE-MRI is related to the contrast variations between image pairs or among temporal sequences caused by the passage of contrast agent. An overview of existing methods to register DCE-MRI data in Chapter 4.

2.7 Conclusion

To sum up, MRI utilises the spin properties of hydrogen nuclei which are abundant in the human body to generate signals which are then converted to images. In order to create these images, a selection of pulse sequences is then required to enable differentiation of the different tissue properties. Gd based contrast agents are administrated to alter image contrast and to provide additional structural and functional information. Consecutive improvements in DCE-MRI such as higher spatial and temporal resolution have driven the development of more complex compartment models to extract useful information from the acquired data. However, the monitoring of contrast agent uptake and washout in different tissues require long scan times and image misalignments are caused by the movements of the patient. Such misalignments cause errors in the quantitative MRI analysis and therefore should be corrected for. The following chapters will discuss some of these challenges in more detail and the proposed solutions.

Chapter 3

Linear Least-Squares Method for Multi-Compartment Models

In previous chapter, background details of DCE-MRI and models for performing quantitative DCE analysis were reviewed. The aim of the study presented in this chapter was to develop a fast linear least-squares method to fit a 4-parameter 2-compartment tracer kinetic model. The standard method for fitting this model to the data is the non-linear least-squares method. However, this method is prohibitively slow for image-wide parameter estimations, and is biased by the choice of initial values. Following a presentation of the existing linearised Tofts model and modified-Tofts model, a new fast linear least-squares method for the two-compartment exchange and -filtration models is introduced. A large part of this work was published in Magnetic Resonance in Medicine [44].

3.1 Introduction

As has already been mentioned in the previous chapter, DCE-MRI involves the serial acquisition of T1-weighted MR images before, during, and after an intravenous administration of contrast agent. Tracer-kinetic analysis of the data produces physiological parameters such as tissue blood flow, capillary permeability, and the volume of the EES [13].

The most common class of tracer-kinetic models are the multi-compartment models,

which are also widely used in other modalities such as positron-emission tomography (PET) and computed tomography (CT). Current standards in DCE-MRI are the two- or three parameter Patlak and Tofts models [45, 46], which do not produce a measurement of tissue blood flow. In recent years, the increasing availability of DCE-MRI at high temporal resolution has promoted the use of four-parameter flow-weighted models such as the two-compartment exchange model (2CXM) [21] and the renal two-compartment filtration model (2CFM) [47, 11].

Non-linear least squares (NLLS) methods are the most commonly used algorithms to fit the model to the data [48]. They require a choice of initial values which is updated iteratively using gradient-descent type methods, until the difference between predicted and measured data is minimal. The process is slow, and there is a risk of convergence to local minima [49, 50]. If this happens the result is biased by the initial values. A potential solution is to repeat the fit over a grid of initial values, but this requires massive computing capacity for pixel-based analysis [51].

An alternative is the use of linear least squares (LLS) methods, which produce parameter estimates by solving a linear system of equations. This is a fast computation that is guaranteed to have a single global minimum and does not require initial values. A classic LLS method is the Patlak plot [45] which solves a two-parameter model using simple linear regression analysis. In 2004, Murase [52] introduced a LLS method for the modified Tofts model. Simulations demonstrated that this improves calculation times significantly without an associated cost in accuracy and precision. The method is rapidly becoming a standard in applications of DCE-MRI [53, 54, 55, 56].

A LLS method for the Tofts model and modified Tofts model has first been performed as preliminary work to ensure that the observations in [52] are valid. The NLLS method for the modified Tofts and Tofts model is based on an explicit analytical solution of the Eqs.(2.28) and (2.30), respectively (see Sections 2.5.2.3 and 2.5.2.4). The linear derivation for the modified Tofts that is to follow is a repetition of a previous study by Murase [52].

To derive a linear inversion method for the modified Tofts model we substitute Eq.(2.25) into Eq.(2.17) which leads to:

$$C(t) = v_p c_a(t) + v_T c_T(t). \tag{3.1}$$

Differentiate Eq.(3.1) and use Eq.(2.26) to eliminate c_T' (writing c_T' for the time-derivative of c_T):

$$C' = v_p c_a' + F_T(c_a - c_T). \tag{3.2}$$

Solving Eq.(3.1) for $c_T(t)$ results in:

$$c_T(t) = \frac{1}{v_T}c(t) - \frac{v_p}{v_T}c_a(t). \tag{3.3}$$

Inserting Eq.(3.3) into Eq.(3.2) leads to a first-order differential equation that only depends on the data C, c_a, and the unknown model parameters. The result is more transparent when expressed in terms of the parameters v_p, v_T, T_T.

$$C' = -\frac{1}{T_T}C + v_p c_a' + \frac{v_p + v_T}{T_T}c_a. \tag{3.4}$$

In order to derive a linear inversion method for the Tofts model we first differentiate Eq.(2.29) and use Eq.(2.26) to eliminate c_T':

$$C' = F_T c_a - F_T c_T. \tag{3.5}$$

Solving Eq.(2.29) for c_T results in:

$$c_T(t) = \frac{1}{v_T}C(t). \tag{3.6}$$

Inserting Eq.(3.6) into Eq.(3.5) leads to a first-order differential equation that only depends on the data C, c_a, and the unknown model parameters. The result in terms of the parameters v_T and T_T is given by:

$$C' = -\frac{1}{T_T}C + \frac{v_T}{T_T}c_a. \tag{3.7}$$

A LLS method for the more general 2CXM and 2CFM has not yet been proposed in the field of DCE-MRI, but in nuclear medicine it is well-known that such more

general models can be linearised too [49, 57, 58, 59, 60, 61]. The aim of this study is to develop a LLS method for the Tofts model and modified Tofts model as preliminary work to ensure that the observations presented in the literature are valid and to further develop a newly LLS method for the 2CXM and 2CFM, and evaluate calculation time, accuracy and precision using simulated data. A standard NLLS with a single set of initial values is used as a point of comparison.

3.2 Theory and Definitions

Although some of the concepts presented in this chapter have already been introduced in previous chapter, they are restated here so this chapter is essentially self-contained. In order the 2CFM to be comparable with the 2CXM we changed the notation from F_T and v_T, as used in previous chapter, to PS and v_e, respectively. The 2CFM is depicted graphically in Figure 3.1. The key difference is that the flux out of the extravascular space is either directed back into the plasma space (2CXM) or directly to the outside (2CFM). Since the physiological interpretation of the parameters is not relevant for the purposes of this chapter, the conventional notations of the 2CFM parameters [11] are modified to emphasize the symmetries and eliminate redundant notations.

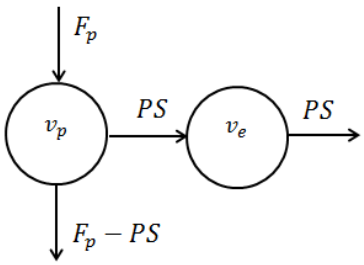

Figure 3.1: Diagram of the 2CFM.

The four independent model parameters are v_p, v_e, F_p and PS. The mean transit times of the extravascular compartment (T_e) and combined system (T) have the same form in both models:

$$T_e = \frac{v_e}{PS}, \qquad T = \frac{v_p + v_e}{F_p}. \tag{3.8}$$

The measured tissue concentration $C(t)$ is a weighted average of the concentrations $c_p(t)$ and $c_e(t)$ in the individual spaces:

$$C = v_p c_p + v_e c_e \tag{3.9}$$

The mass-balance for $c_e(t)$ is the same for both models (writing c_e' for the time-derivative of c_e):

$$v_e c_e' = PS(c_p - c_e) \tag{3.10}$$

The difference between 2CXM and 2CFM lies in the mass-balance for $c_p(t)$. Given the arterial concentration $c_a(t)$, we have [21, 11]:

$$\text{2CFM} \quad : \quad v_p c_p' = F_p(c_a - c_p), \tag{3.11}$$

$$\text{2CXM} \quad : \quad v_p c_p' = F_p(c_a - c_p) + PS(c_e - c_p). \tag{3.12}$$

We assume that $c_p(0) = c_e(0) = c_a(0) = 0$ which immediately leads to the initial conditions

$$C(0) = C'(0) = 0. \tag{3.13}$$

3.3 Methods

3.3.1 Non-Linear Least-Squares

As we have seen in previous chapter, the NLLS method is based on an explicit analytical solution of the models:

$$C(t) = F_p \left(\frac{T - T_-}{T_+ - T_-} e^{-t/T_+} + \frac{T_+ - T}{T_+ - T_-} e^{-t/T_-} \right) \otimes c_a(t). \tag{3.14}$$

The difference between 2CXM and 2CFM lies in the relation between $T_\pm$ and the physiological parameters F_p, v_p, PS, v_e. The formulae are most straightforward in terms of the mean transit times (Eqs.(3.8)):

$$\text{2CFM} \ : \ T_+ = T_e, \qquad T_- = T_p, \tag{3.15}$$

$$\text{2CXM} \ : \ T_{\pm} = \frac{1}{2}\left(T + T_e \pm \sqrt{(T+T_e)^2 - 4T_pT_e}\right). \tag{3.16}$$

The analytical solution of the 2CXM as introduced in previous chapter in Eq.(2.47) is equivalent to Eq.(3.14) when the following relation between the eigenvalues and $T_{\pm}$ taken into account:

$$\lambda_{1,2} = -\frac{1}{T_{\mp}}. \tag{3.17}$$

The conventional NLLS method uses gradient-descent type techniques to minimise the mean-square difference between left- and right hand sides of Eq.(3.14).

3.3.2 Linear Least-Squares

The LLS method is based on a reduction of the two first-order differential equations for the unmeasurable concentrations $c_p(t)$ and $c_e(t)$ (Eqs.(3.10), (3.11) and (3.12)) to a single second-order differential equation for the measurable concentration $C(t)$ (Eq.(3.9)). The derivation follows a standard recipe that applies more generally to arbitrary N-compartment models [57].

We will present the derivation in more detail for the 2CFM alone, as the procedure is exactly the same for the 2CXM. First, differentiate Eq.(3.9) and use Eqs.((3.10), (3.11)) to eliminate c_e' and c_p':

$$C' = F_p(c_a - c_p) + PS(c_p - c_e). \tag{3.18}$$

Then repeat the same process: differentiate Eq.(3.18), use Eqs.(3.10) and (3.11) to eliminate c_e' and c_p', and simplify the result:

$$C'' = F_p c_a' - (F_p - PS)\frac{F_p}{v_p}(c_a - c_p) - PS\frac{PS}{v_e}(c_p - c_e). \tag{3.19}$$

We have now produced 3 equations (Eqs.(3.9,3.18,3.19)) that only contain two unknown functions $c_p(t)$ and $c_e(t)$. The first two of these equations are used to solve for these unknown functions, and the results are then inserted into the third. Explicitly, solving Eqs.(3.9) and (3.18) for c_p and c_e leads to:

$$c_p = \frac{PSC - (F_p c_a - C')v_e}{PSv_p + (PS - F_p)v_e}, \tag{3.20}$$

$$c_e = \frac{F_p v_p c_a + (PS - F_p)C - v_p C'}{PS v_p + (PS - F_p) v_e}. \tag{3.21}$$

Inserting Eqs.(3.20) and (3.21) into Eq.(3.19) leads to a single second-order equation that only depends on the data C, c_a, and the unknown model parameters. The result is most transparent when expressed in terms of the parameters F_p, T, T_p, T_e. After some simplification a very similar result arises for 2CFM and 2CXM:

$$C'' = -\alpha C - \beta C' + \gamma c_a + F_p c_a'. \tag{3.22}$$

The parameters (α, β, γ) are defined as:

$$\text{2CFM} \; : \; \alpha = \frac{1}{T_e T_p}, \quad \beta = \frac{T_e + T_p}{T_e T_p}, \quad \gamma = \frac{F_p T}{T_e T_p} \tag{3.23}$$

$$\text{2CXM} \; : \; \alpha = \frac{1}{T_e T_p}, \quad \beta = \frac{T_e + T}{T_e T_p}, \quad \gamma = \frac{F_p T}{T_e T_p} \tag{3.24}$$

To avoid the problems associated with numerical differentiation of noisy data, Eq.(3.22) can be integrated twice over time. Using the following notation for the integral:

$$\bar{f}(t) = \int_0^t f(\tau)\, d\tau \tag{3.25}$$

this leads to:

$$C(t) = -\alpha\, \bar{\bar{C}}(t) - \beta\, \bar{C}(t) + \gamma\, \bar{\bar{c}}_a(t) + F_p\, \bar{c}_a(t). \tag{3.26}$$

If the data $C(t)$ and $c_a(t)$ are measured at N time points $t_0, t_1, \ldots, t_{N-1}$, then Eq.(3.26) leads to a system of N linear equations. They can be summarised as a matrix equation $\mathbf{C} = \mathbf{A}\mathbf{X}$, where $\mathbf{C} = [C(t_0), \ldots, C(t_{N-1})]$ is a vector holding the measured concentrations, and $\mathbf{X} = [\alpha, \beta, \gamma, F_p]$ contains the unknowns. The $4 \times N$-element matrix $\mathbf{A}$ is given explicitly by:

$$\mathbf{A} = \begin{pmatrix} -\bar{\bar{C}}(t_0) & -\bar{C}(t_0) & \bar{\bar{c}}_a(t_0) & \bar{c}_a(t_0) \\ -\bar{\bar{C}}(t_1) & -\bar{C}(t_1) & \bar{\bar{c}}_a(t_1) & \bar{c}_a(t_1) \\ \vdots & \vdots & \vdots & \vdots \\ -\bar{\bar{C}}(t_{N-1}) & -\bar{C}(t_{N-1}) & \bar{\bar{c}}_a(t_{N-1}) & \bar{c}_a(t_{N-1}) \end{pmatrix} \tag{3.27}$$

The matrix elements can be calculated via Eq.(3.25) by numerical integration of the data $C(t_n)$ and $c_a(t_n)$. The matrix equation can be solved using standard methods for linear least squares problems, e.g. the ordinary LLS yields:

$$\mathbf{X} = (\mathbf{A}^{\mathrm{T}}\mathbf{A})^{-1}\mathbf{A}^{\mathrm{T}}\mathbf{C}. \tag{3.28}$$

Since the typical number of time points in DCE-MRI is in the 100's, and there are only 4 unknowns, this presents a strongly overdetermined system.

It remains to derive the physiological parameters T, T_e, T_p from given α, β, γ, F_p by inverting Eqs.(3.23) and (3.24). For the 2CXM this is most straightforward:

$$T = \frac{\gamma}{\alpha F_p}, \quad T_e = \frac{\beta}{\alpha} - T, \quad T_p = \frac{1}{\alpha T_e}. \tag{3.29}$$

In the 2CFM, the formula for T is the same, but T_e and T_p are the solutions of a quadratic equation:

$$T_p = \frac{\beta - \sqrt{\beta^2 - 4\alpha}}{2\alpha}, \quad T_e = \frac{\beta + \sqrt{\beta^2 - 4\alpha}}{2\alpha}. \tag{3.30}$$

A second solution could be derived by reversing the roles of T_p and T_e, but in reality it is safe to assume that contrast agent passes faster through the microvasculature than through the extravascular space ($T_p < T_e$). Since α and β are measured there is no a priori guarantee that these solutions are real. In case they are not ($\beta^2 < 4\alpha$) the best solution in the least squares sense is:

$$T_p = T_e = \frac{\beta}{2\alpha}. \tag{3.31}$$

The parameters v_p, v_e and PS can be derived from F_p, T, T_p, T_e by inverting Eqs.(3.8):

$$v_p = F_p T_p, \qquad v_e = F_p(T - T_p), \qquad PS = \frac{v_e}{T_e}. \tag{3.32}$$

3.3.3 Weighted Linear Least-Squares

Eq.(3.26) can be generalised by multiplying both sides with an arbitrary weighting function $W(t)$:

$$WC = -\alpha W\bar{\bar{C}} - \beta W\bar{C} + \gamma W\bar{c_a} + F_p W\bar{c_a}. \tag{3.33}$$

With $W(t) = 1$ this reduces to the LLS, but a large number of possible weighting functions $W(t)$ could be used. To investigate the effect and potential of weighting we will consider in this study the strategy $W(t) = c_a(t)$, i.e. we use the signal itself for weighting the data. As the arterial input function is strongly weighted by the first pass data, one would expect this to improve the accuracy in the parameters F_p and T_p which are mainly determined by the high-frequency components occuring in this time window.

3.4 Simulation Setup

Simulations were used to evaluate the sensitivity of the LLS to two important types of data error, random noise and temporal undersampling. Simulations were performed for the 2CFM and the 2CXM as well as for the modified Tofts and Tofts models. Simulations were written in IDL 6.4 (Exelis VIS, Boulder, CO) conducted on a desktop PC with a 3.4 GHz Intel Core processor and 32GB memory. All simulation code for the 2CFM and the 2CXM can be found online (https://github.com/plaresmedima/Linear-2CM).

As the 2CFM is typically applied to renal data, a representative set of five whole-kidney tissues were defined: one representing normal kidneys with parameter values measured in healthy volunteers [11], and four pathological kidneys taken from a recent patient study [62]. Cases were selected by identifying the kidneys corresponding to the 10th and 90th percentiles in T_e and v_p. The parameters are summarised in Table 3.1.

To generate an exact ground-truth $C(t)$, one of the five tissue types was selected at random with equal probability, and $C(t)$ was calculated with the analytical solution (Eq.(3.14)). A literature-based arterial input function $c_a(t)$ was used [23], prepadded with zeroes to create a 20s baseline. $C(t)$ and $c_a(t)$ were created at a pseudo-continuous temporal resolution of 10msec for times ranging from $t = 0s$ to a total

	T_p (sec)	T_e (sec)	v_p	v_e
Normal	6.5	125	0.24	0.62
Patient 1	9.5	102	0.17	0.24
Patient 2	13.9	153	0.31	0.24
Patient 3	7.27	117	0.19	0.26
Patient 4	10.3	214	0.29	0.18

Table 3.1: Parameter values of the simulated data sets.

of $T_{acq} = 300s$. All convolutions in this study are calculated using a formula that is optimised for convolutions with an exponential factor (see Appendix A).

Measurements with a given uniform sampling interval TR (sec) and Contrast-to-Noise Ratio (CNR) were simulated. CNR is defined in this study as the ratio of peak arterial concentration to the standard deviation (SD) of the noise, i.e. CNR = $\max(c_a)$/SD. In DCE-MRI this is a better measure for the noise level than Signal-to-Noise Ratio (SNR) as the analysis is performed on signal changes rather than on absolute signal values. The first time-point t_0 of the measurement was determined by selecting a random number from a uniform distribution on the interval [0,TR]. Then time-points $t_n = t_0 + n\text{TR}$ were added with $n = 1, \ldots, N-1$ and $N = \lfloor T_{acq}/\text{TR} \rfloor$. Downsampled $C(t_n)$ and $c_a(t_n)$ were created by interpolating linearly between the values of the pseudo-continuous curves, and Gaussian noise was added.

The LLS matrix (Eq.(3.27)) was calculated by numerical integration of the measured $C(t_n)$ and $c_a(t_n)$ using the trapezoidal rule. The least-squares system was solved by inverting the 4×4 normal equations to obtain the solution (3.28). The NLLS was implemented by fitting the analytical solution (Eq.(3.14)) using the Levenberg-Marquardt algorithm with the function MPFIT [63]. Convolutions were calculated with the iterative formula in the Appendix A. Partial derivatives with respect to the model parameters were calculated numerically and default values were used for the termination tolerance (10^{-3}) and maximum number of iterations (200). No constraints were placed on any of the parameters, and fixed initial values were used. They were taken at approximately half the exact values in normal tissue to avoid a bias with respect to a particular tissue type ($T_p = 3s$, $T_e = 60s$, $v_p = 0.1$, $v_e = 0.3$).

In the particular case of the preliminary study, the input data $C(t)$ and $c_a(t)$ were numerically generated for the modified Tofts models and Tofts model in the same way as in 2CFM and 2CXM. It is essential to mention that the data have been simulated and then fitted using the modified Tofts model and Tofts model individu-

ally. The sensitivity of the LLS method with respect to random noise and temporal resolution has been tested only in normal kidneys. To simulate the effect of noise alone on accuracy and precision of the LLS, TR was fixed to 1s and CNR was varied from 50 to 250 in 9 steps. To isolate the effect of temporal undersampling, TR is ranging from 0.001s to 9s in 9 steps at fixed CNR value of 1000.

3.5 Data Analysis

For each reconstruction P_i of a parameter $P = F_p$, PS, T_p, T_e, the error $E_i(P)$ was determined as a percentage of the exact value:

$$E_i(P) = 100 * \frac{P_i - P}{P} \tag{3.34}$$

The goodness-of-fit was quantified in a similar way as the relative distance between the fitted concentrations $C_i^{\text{fit}}(t_n)$ and measured concentrations $C_i^{\text{msr}}(t_n)$:

$$E_i(C) = 100 * \frac{\|C_i^{\text{fit}} - C_i^{\text{msr}}\|_2}{\|C_i^{\text{msr}}\|_2} \tag{3.35}$$

Simulations for given TR and CNR were repeated 10,000 times to determine the distribution of results. The median relative error E_{50} was recorded as a measure of the systematic error, and the 90% confidence interval CI $= E_{95} - E_5$ as a measure of the random error.

The performance of the LLS or WLLS was quantified via two figures of merit (FoM), one for the accuracy and one for the precision:

$$\text{FoM (Accuracy)} = |E_{50}(\text{NLLS})| - |E_{50}(\text{LLS})| \tag{3.36}$$

$$\text{FoM (Precision)} = \text{CI(NLLS)} - \text{CI(LLS)} \tag{3.37}$$

A positive (negative) FoM means that the LLS improves (reduces) the accuracy or precision. Numerically, a FoM of 1% implies that LLS reduces the systematic or random error by 1% of the exact parameter value. FoM's were determined explicitly for 3 different protocols:

- Protocol 1 (CNR=50 and TR=1.25s) models single-voxel data at high tem-

poral resolution (and thus high noise levels).

- Protocol 2 (CNR=10000 and TR=12.5s) models ROI data at low temporal resolution (and thus low noise levels).
- Protocol 3 (CNR=10000 and TR=1.25s) models ideal conditions of high temporal resolution and low noise levels.

Protocols 1 and 2 represent realistic boundary regimes, and may be used to measure F_p-maps (protocol 1) or ROI-based PS (protocol 2). Protocol 3 represents a limiting case of error-free data that cannot be realised in practice but is useful to help understand the fundamental behavior of the methods. Realistic CNR and TR values for protocol 1 were estimated by measurement on a patient data set acquired with a standard 2D acquisition protocol [11]. Values for protocol 2 were estimated on the same data after time-averaging to a TR of 12.5s.

3.6 Results

3.6.1 Preliminary Work

Figures 3.2 and 3.3 show the relative error of the estimated parameter values for the normal tissues, as functions of the TR, obtained using the LLS and NLLS methods for the Tofts model and modified Tofts model, respectively. From these figures it can be seen that both LLS and NLLS show close agreement in terms of precision and accuracy.

Figures 3.4 and 3.5 show the same relative error of the estimated parameter values for the normal tissue, but as functions of the percentage of noise, obtained using the LLS and NLLS methods for the Tofts and modified Tofts model, respectively. The figures show that the LLS and NLLS methods show close agreement in terms of precision and accuracy.

Regarding the calculation time, for the modified Tofts model the LLS method is faster than the NLLS method by a factor of 56. In absolute terms, for an MR image of 256×256 pixels the computation time on a laptop PC is 1.7 sec and 1.6 min for the LLS and NLLS methods, respectively. For Tofts model the LLS method is faster than the NLLS method by a factor of 49. In absolute terns, for an MR image of 256×256 pixels the computation time on a laptop PC is 1.6 sec and 1.3 min for the LLS and NLLS methods, respectively.

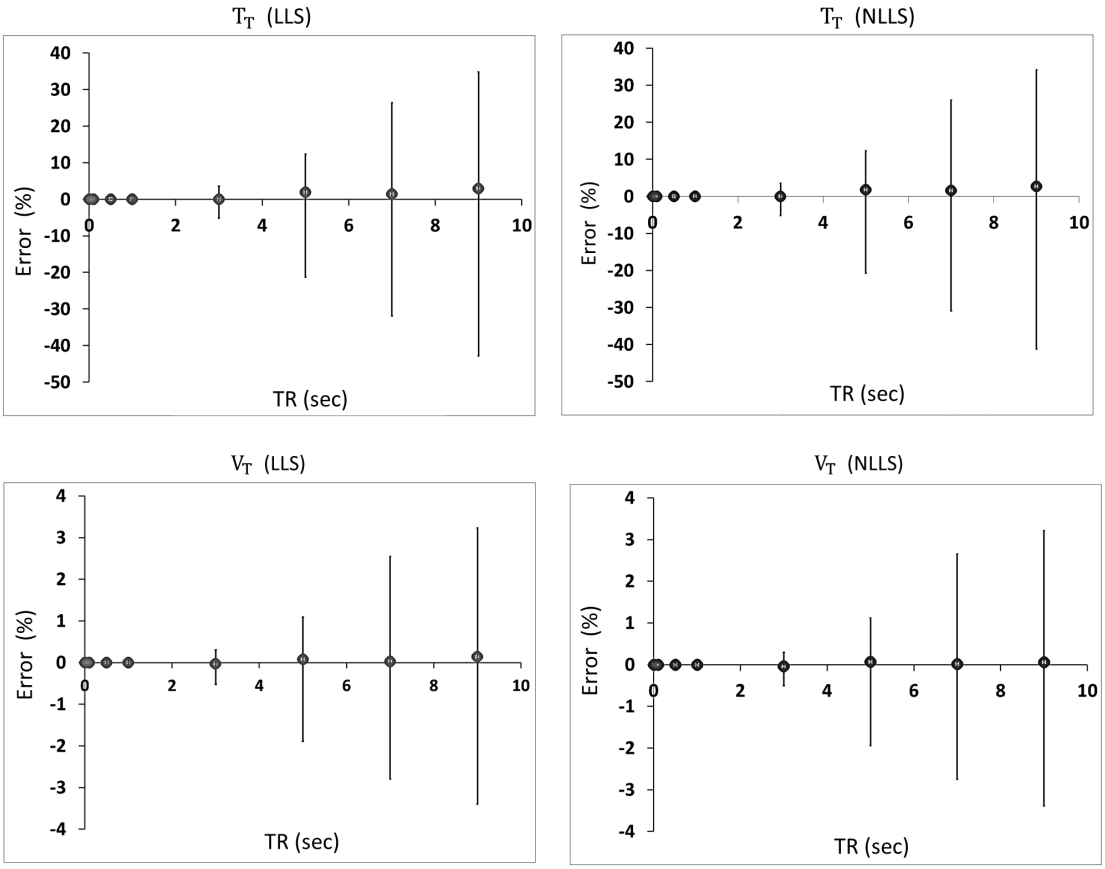

Figure 3.2: Error distribution of the Tofts model at fixed CNR=1000 but variable TR. The circles indicate the median error and the error bars represent the 90% confidence interval. Results are shown for each method (LLS - left column, NLLS - right column) and for each parameter (T_T - top row, v_T - lower row).

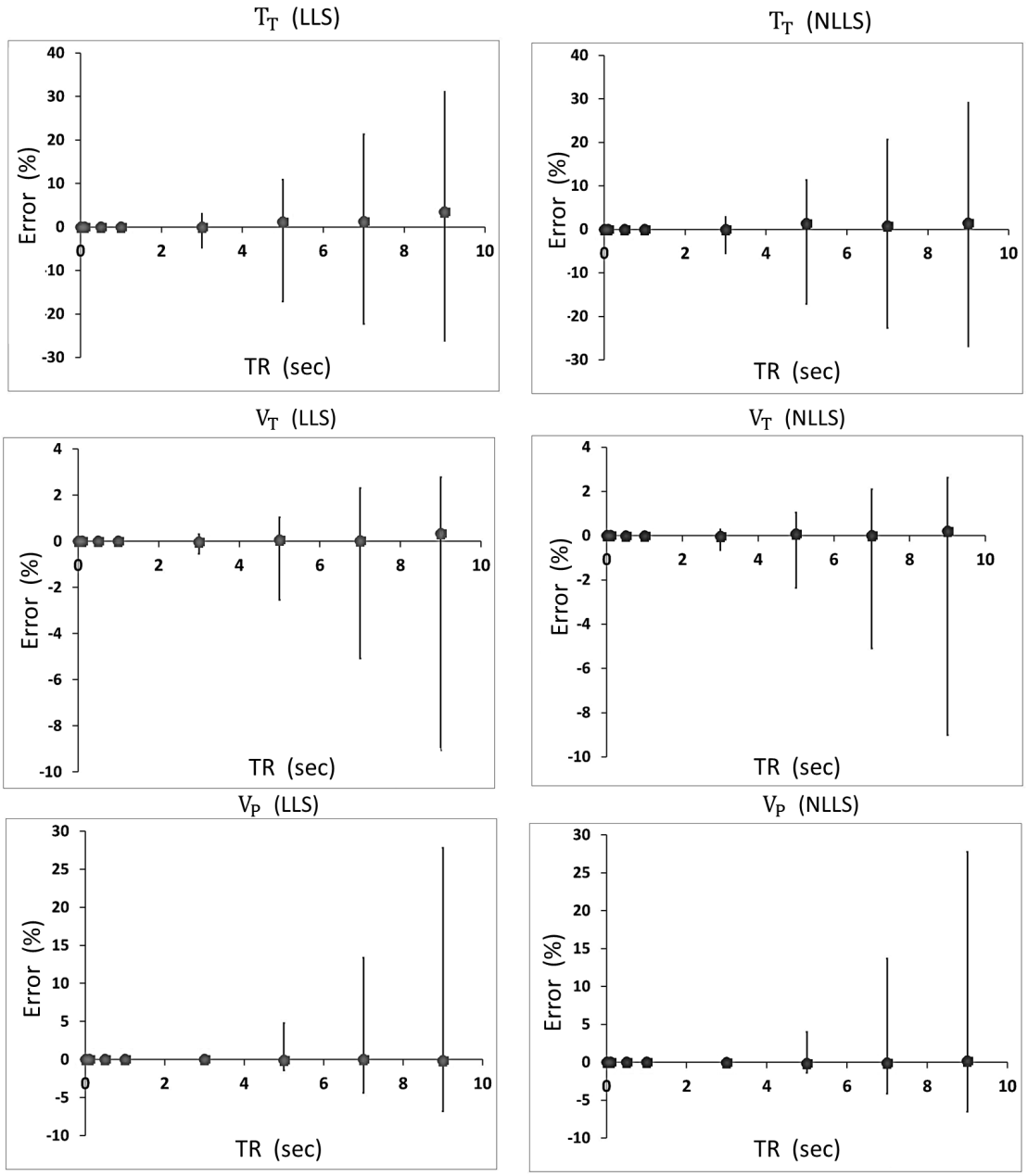

Figure 3.3: Error distribution of the modified Tofts model at fixed CNR=1000 but variable TR. The circles indicate the median error and the error bars represent the 90% confidence interval. Results are shown for each method (LLS - left column, NLLS - right column) and for each parameter (T_T - top row, v_p - middle row, v_T - lower row).

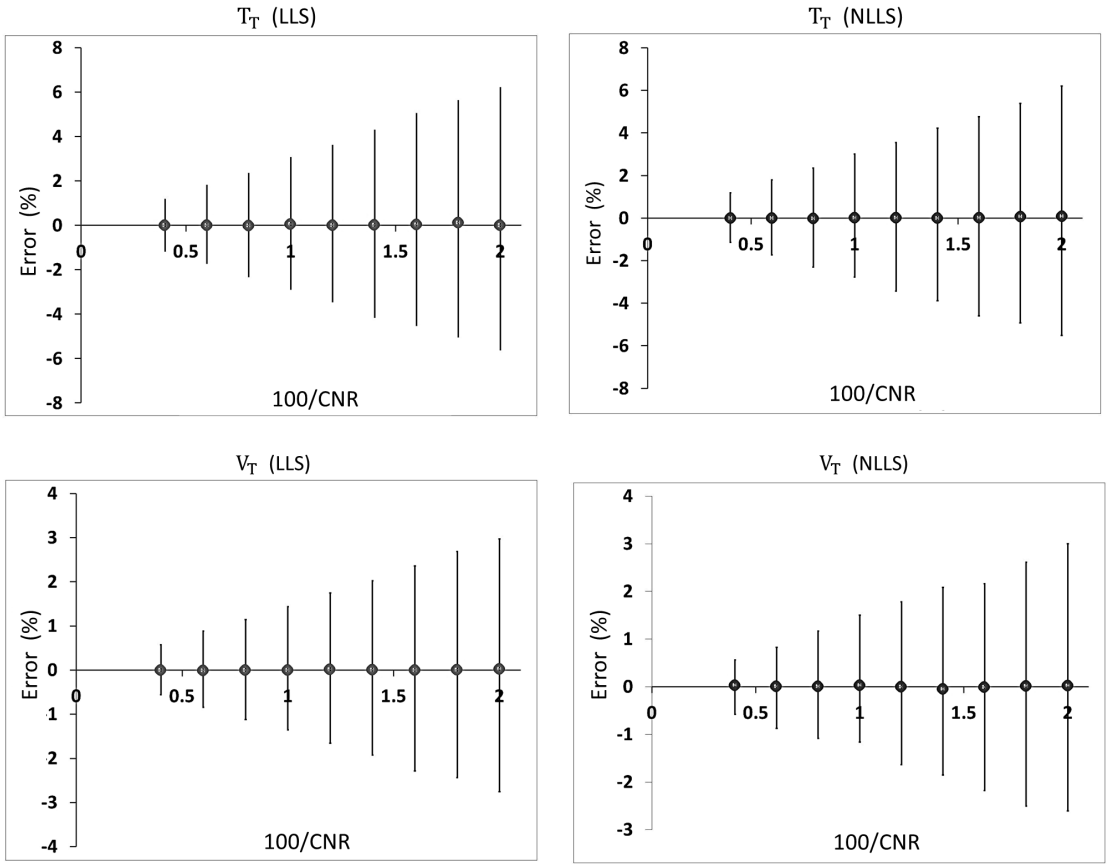

Figure 3.4: Error distribution of the Tofts model at fixed TR=1s but variable CNR with a minimum of CNR=50. The circles indicate the median error and the error bars represent the 90% confidence interval. Results are shown for each method (LLS - left column, NLLS - right column) and for each parameter (T_T - top row, v_T - lower row).

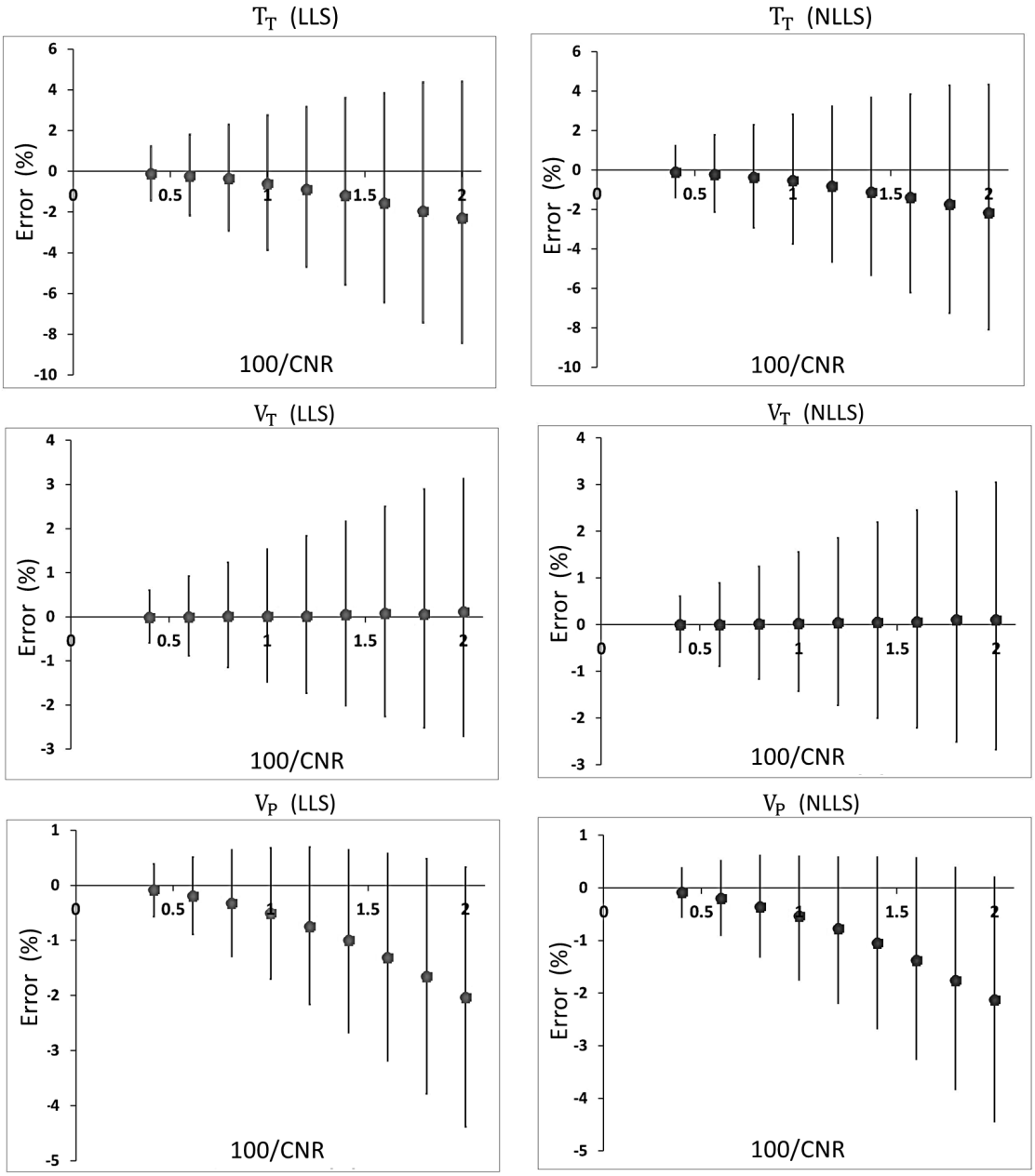

Figure 3.5: Error distribution of the modified Tofts model at fixed TR=1s but variable CNR with a minimum of CNR=50. The circles indicate the median error and the error bars represent the 90% confidence interval. Results are shown for each method (LLS - left column, NLLS - right column) and for each parameter (T_T - top row, v_p - middle row, v_T - lower row).

3.6.2 Two-compartment Model

Figures 3.6 and 3.7 provide an illustration of the data and model fits at the highest noise level considered in this study using the 2CFM and 2CXM, respectively. The plots show that the fit to the data is significantly poorer with LLS than with NLLS, which provides an almost exact reconstruction of the underlying concentrations despite high levels of noise.

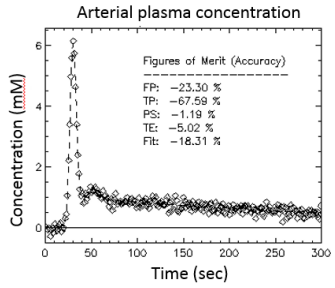

(a)

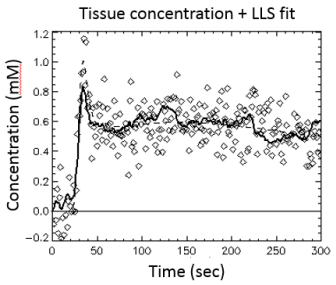

(b)

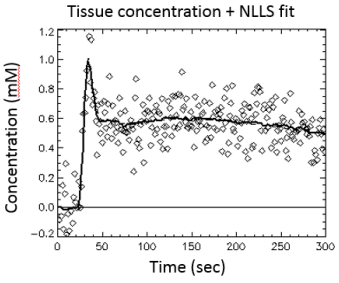

(c)

Figure 3.6: Example of simulated data for single-voxel curve (protocol 1) at TR=1.25s and CNR=50. (a) The figure shows results in the arterial plasma. The dashed line represent the exact concentration. The insert gives the Figures of Merit for each of the parameters in this particular case. (b) The figure shows results in the tissue with an overlay of the LLS fit (full line) using the 2CFM. The dashed line represent the exact concentration and the diamonds indicate the simulated measurements. (c) The figure shows results in the tissue with an overlay of the NLLS fit (full line). The dashed line represent the exact concentration and the diamonds indicate the simulated measurements.

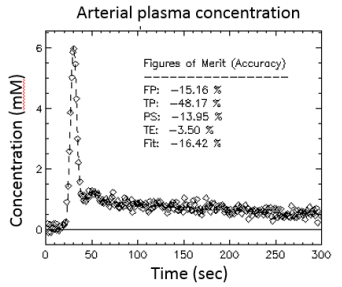

(a)

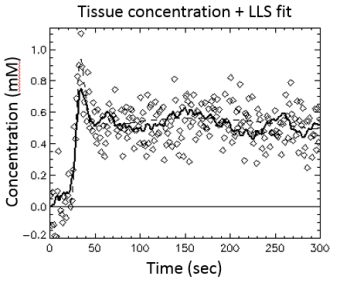

(b)

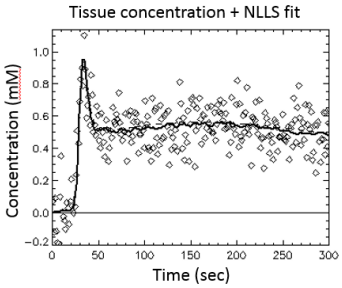

(c)

Figure 3.7: Example of simulated data for single-voxel curve (protocol 1) at TR=1.25s and CNR=50. (a) The figure shows results in the arterial plasma. The dashed line represent the exact concentration. The insert gives the Figures of Merit for each of the parameters in this particular case. (b) The figure shows results in the tissue with an overlay of the LLS fit (full line) using the 2CXM. The dashed line represent the exact concentration and the diamonds indicate the simulated measurements. (c) The figure shows results in the tissue with an overlay of the NLLS fit (full line). The dashed line represent the exact concentration and the diamonds indicate the simulated measurements.

Tables 3.2 and 3.3 provide the FoM's under the conditions of high noise and high temporal resolution (protocol 1) for the 2CFM and 2CXM, respectively. In this regime the LLS is associated with a significant loss in accuracy in all parameters (2CFM: -30%, 2CXM: -34% on average). Adding weighting improves the accuracy in all parameters, but it is still lower than with NLLS (2CFM: -9%, 2CXM: -11% on average). The effect on precision depends on the parameter: LLS causes a major loss in precision for T_p (2CFM: -95%, 2CXM:-119%), but improves the precision for PS and T_e. In this case the weighting has a benefit as it reduces the loss in precision for T_p. But the effect remains significant and also leads to a reduction in precision of F_p.

	LLS		**WLLS**	
	Accuracy(%)	Precision(%)	Accuracy(%)	Precision(%)
F_p	-19	-5	-3	-17
T_p	-45	-95	-9	-32
PS	-31	32	-16	4
T_e	-23	1810	-7	1985

Table 3.2: Figures of Merit (FoM) of the 2CFM for LLS and WLLS for protocol 1 at high noise level (CNR=50) and high temporal resolution (TR=1.25s).

	LLS		**WLLS**	
	Accuracy(%)	Precision(%)	Accuracy(%)	Precision(%)
F_p	-23	-7	-3	-18
T_p	-42	-119	-1	-26
PS	-33	24	-19	5
T_e	-39	279	-22	598

Table 3.3: Figures of Merit (FoM) of the 2CXM for LLS and WLLS for protocol 1 at high noise level (CNR=50) and high temporal resolution (TR=1.25s).

Tables 3.4 and 3.5 provide the FoM's under the opposite conditions of low noise and low temporal resolution (protocol 2) for the 2CFM and 2CXM, respectively. Under these conditions the LLS shows a clear improvement in accuracy (2CFM: +10%, 2CXM: +11% on average) and precision in all parameters. In this particular scenario there is no numerical benefit in adding a weighting with $W(t) = c_a(t)$. The gain in precision is +4763% for the 2CFM and +4672% for the 2CXM on average, but this is largely determined by an outlier (T_e). Excluding this, the gain in precision is still +129% using the 2CFM and +139% using he 2CXM on average.

	LLS		**WLLS**	
	Accuracy(%)	Precision(%)	Accuracy(%)	Precision(%)
F_p	14	265	-14	122
T_p	13	49	-13	-242
PS	7	74	6	-40
T_e	6	18664	-0.1	18680

Table 3.4: Figures of Merit (FoM) of the 2CFM for LLS and WLLS for protocol 2 at low noise level (CNR=10000) and low temporal resolution (TR=12.5s).

	LLS		**WLLS**	
	Accuracy(%)	Precision(%)	Accuracy(%)	Precision(%)
F_p	14	310	-16	147
T_p	13	52	-14	-217
PS	7	56	5	-55
T_e	8	18269	9	18264

Table 3.5: Figures of Merit (FoM) of the 2CXM for LLS and WLLS for protocol 2 at low noise level (CNR=10000) and low temporal resolution (TR=12.5s).

Tables 3.6 and 3.7 provide the FoM's under the ideal circumstances of protocol 3 (low noise and high temporal resolution) for the 2CFM and 2CXM, respectively. The results show that LLS leads to small changes in both accuracy (0.1% improvement on average) and precision (0.1% loss on average) for both models. As for protocol 2 there is no numerical benefit in adding a weighting with $W(t) = c_a(t)$ in this particular scenario.

	LLS		**WLLS**	
	Accuracy(%)	Precision(%)	Accuracy(%)	Precision(%)
F_p	0.27	-0.11	0.1	-0.2
T_p	0.15	-0.14	0.01	-0.2
PS	-0.01	-0.1	-0.13	-0.2
T_e	-0.01	-0.1	-0.07	-0.3

Table 3.6: Figures of Merit (FoM) of the 2CFM for LLS and WLLS for protocol 3 under ideal conditions of low noise level (CNR=10000) and high temporal resolution (TR=1.25s).

	LLS		**WLLS**	
	Accuracy(%)	Precision(%)	Accuracy(%)	Precision(%)
F_p	0.24	-0.13	0.1	-0.2
T_p	0.19	-0.16	0.01	-0.2
PS	-0.1	-0.1	-0.15	-0.2
T_e	-0.01	-0.1	-0.07	-0.3

Table 3.7: Figures of Merit (FoM) of the 2CXM for LLS and WLLS for protocol 3 under ideal conditions of low noise level (CNR=10000) and high temporal resolution (TR=1.25s).

Figures 3.8 and 3.9 show that the differences in accuracy and precision are small under the ideal conditions of protocol 3. The distinction between LLS and NLLS is most pronounced in the parameter F_p, where NLLS and LLS produce relative errors in the range $0.4\% \pm 0.6\%$ and $0.2\% \pm 0.4\%$, respectively (median $\pm$ half of 90% CI) in both models.

Figures 3.10 and 3.11 visualise the transition in the low-noise regime for 2CFM and 2CXM, respectively, from protocol 3 (high temporal resolution) to protocol 2 (low temporal resolution) in more detail. Both figures show that the improved accuracy and precision of the LLS persists across the whole range of temporal resolutions, becoming gradually more pronounced towards protocol 2 at the low temporal resolution (right side of the plot).

Figures 3.12 and 3.13 visualise the transition in the high temporal resolution regime for the 2CFM and 2CXM, respectively, from protocol 3 (low noise) to protocol 1 (high noise). Both figures show that the errors increase in a systematic manner with CNR, showing the stronger noise-sensitivity of LLS. For a measurement targeting the vascular parameters F_p and T_p, the NLLS is more reliable at all noise levels. The NLLS is also preferred for the permeability parameters PS and T_e, except in the high-noise limit of protocol 1 where the WLLS is the optimal.

Regarding the calculation time, the LLS method is faster than the NLLS method by a factor of 200, i.e. two orders of magnitude. In absolute terms, for an MR image of 256×256 pixels the computation time on a laptop PC is 3 sec and 9 min for the LSS and NLLS methods, respectively.

Figure 3.8: The error distribution of the 2CFM for protocol 3 under ideal conditions of low noise level (CNR=10000) and high temporal resolution (TR=1.25s) . Results are shown for each method (LLS - top row, WLLS - middle row, NLLS - lower row) and for each parameter (F_p - column 1, T_p - column 2, PS - column 3, T_e - column 4, goodness-of-fit - column 5).

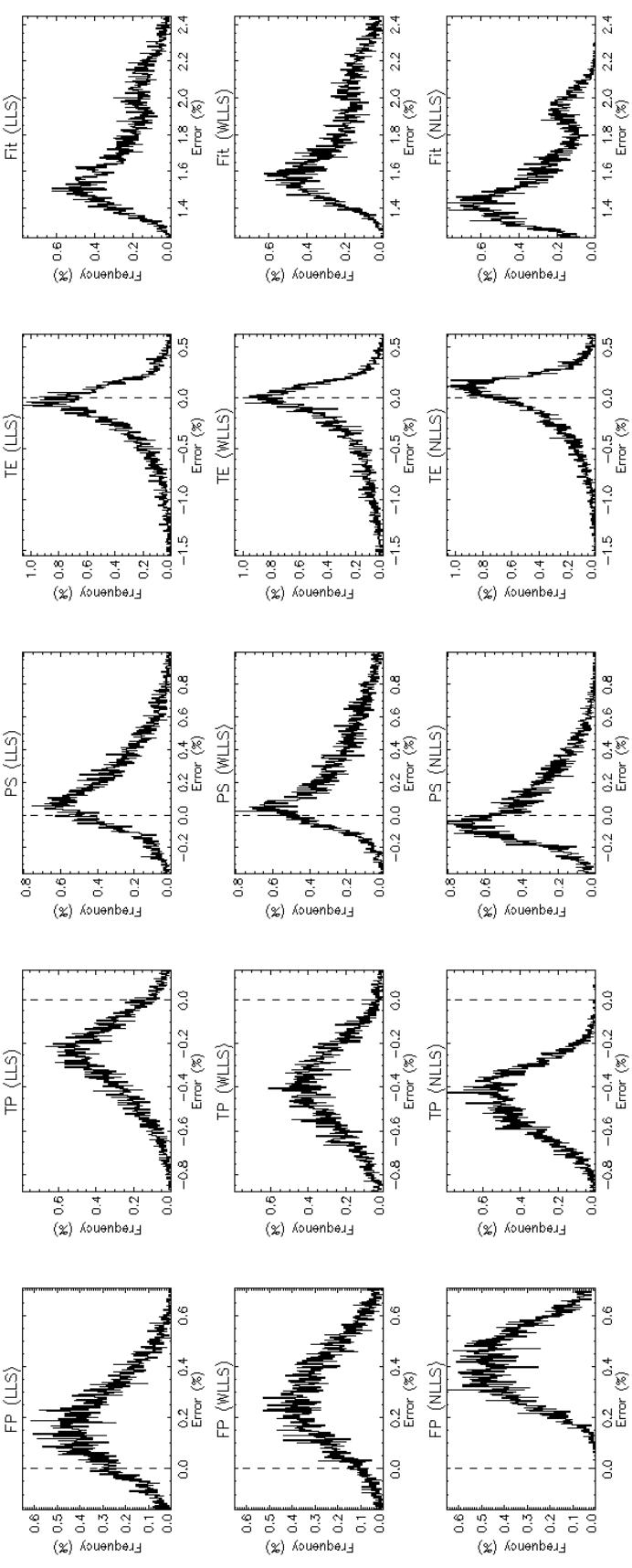

Figure 3.9: The error distribution of the 2CXM for protocol 3 under ideal conditions of low noise level (CNR=10000) and high temporal resolution (TR=1.25s) . Results are shown for each method (LLS - top row, WLLS - middle row, NLLS - lower row) and for each parameter (F_p - column 1, T_p - column 2, PS - column 3, T_e - column 4, goodness-of-fit - column 5).

Figure 3.10: Error distribution of the 2CFM at fixed CNR=10000 (low noise level) but variable TR. The circles indicate the median error and the error bars represent the 90% confidence interval. Results are shown for each method (LLS - top row, WLLS - middle row, NLLS - lower row) and for each parameter (F_p - column 1, T_p - column 2, PS - column 3, T_e - column 4, goodness-of-fit - column 5).

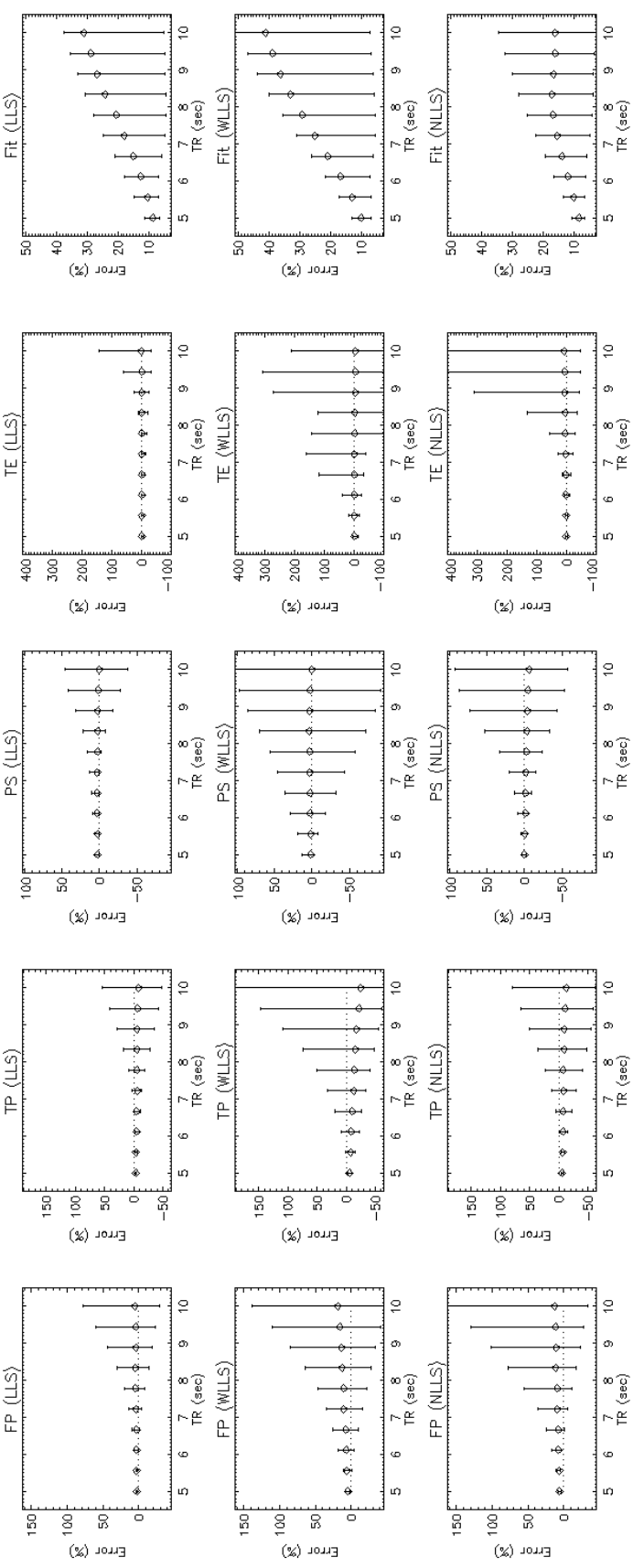

Figure 3.11: Error distribution of the 2CXM at fixed CNR=10000 (low noise level) but variable TR. The circles indicate the median error and the error bars represent the 90% confidence interval. Results are shown for each method (LLS - top row, WLLS - middle row, NLLS - lower row) and for each parameter (F_p - column 1, T_p - column 2, PS - column 3, T_e - column 4, goodness-of-fit - column 5).

Figure 3.12: Error distribution of the 2CFM at fixed TR=1.25s (high temporal resolution) but variable CNR with a minimum of CNR=50 . The circles indicate the median error and the error bars represent the 90% confidence interval. Results are shown for each method (LLS - top row, WLLS - middle row, NLLS - lower row) and for each parameter (F_p - column 1, T_p - column 2, PS - column 3, T_e - column 4, goodness-of-fit - column 5).

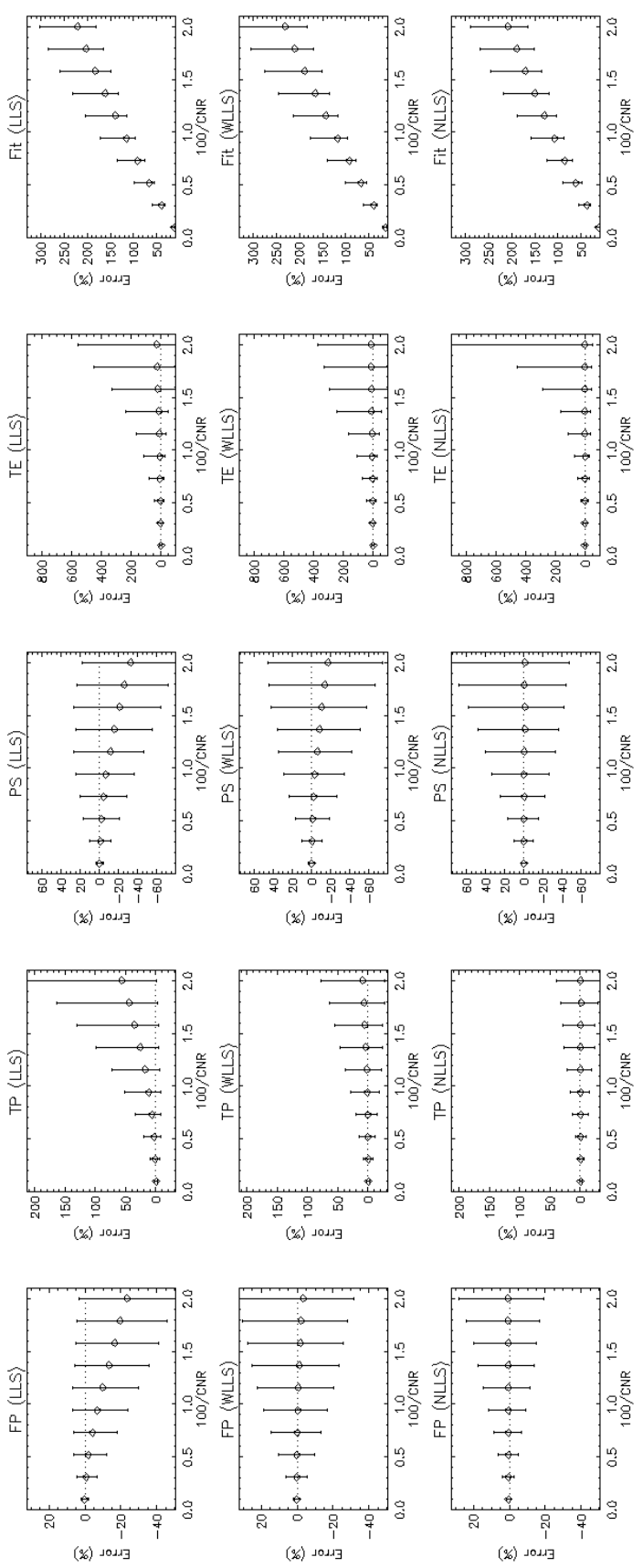

Figure 3.13: Error distribution of the 2CXM at fixed TR=1.25s (high temporal resolution) but variable CNR with a minimum of CNR=50 . The circles indicate the median error and the error bars represent the 90% confidence interval. Results are shown for each method (LLS - top row, WLLS - middle row, NLLS - lower row) and for each parameter (F_p - column 1, T_p - column 2, PS - column 3, T_e - column 4, goodness-of-fit - column 5).

3.7 Discussion

As expected, the LLS leads to a massive reduction in computation time with a factor 200. The current study showed a reduction from 9 min to 3 sec for a 256×256 matrix, but the total saving depends on computing hardware, implementation details, and the number of time points in the data. It also depends on the implementation of the NLLS. In this study a fixed initial value was used rather than a grid of initial values, and in that sense the estimate of NLLS calculation time represents a best case scenario. The improvement in calculation time is not of practical significance for a ROI-based analysis, where other steps in the analysis form the main bottlenecks (e.g. data transfer, segmentation). However for a pixel-based analysis the improvement may have significant implications for clinical practice. The effect may also be important for other methods that use pixel-based tracer-kinetic modeling as an intermediate step, such as model-based segmentation or registration techniques, or data undersampling strategies using the temporal structure as a constraint.

Overall the results from the preliminary work were consistent with Murase [52] linearising the modified-Tofts model. Our results suggested that the LLS for the linearised modified Tofts and Tofts model can estimate the kinetic parameters faster than the NLLS with no distortion in accuracy and precision, as expected based on previous studies [52, 64]. In the case of the Tofts model, Figure 3.2 shows that for the parameters T_T and v_T the median values for the relative error is very close to zero showing that the inversion with either the LLS or NLLS method produces very accurate results. This study showed a reduction in computation time when the LLS used, as expected. From 1.6 min to 1.7 sec for the modified Tofts model and from 1.3 min to 1.6 sec for the Tofts model for a 256×256 matrix. The total saving depends on the reasons stated above.

The effect of LLS on accuracy and precision is more ambiguous for the 2CFM and 2CXM. Key observations are summarised in Figure 3.14. As a general rule, the LLS is preferred at low-noise conditions and the NLLS at high temporal resolution. In the ideal conditions where these two regimes meet (protocol 3), their performance is comparable and both can be used interchangeably. The NLLS is slightly more reliable as the gain in precision offsets the loss in accuracy, but the differences are small and not likely to be significant for clinical applications. In that sense, the LLS may be preferred in view of its computational benefit. There is no benefit of adding a weighting with $W(t) = c_a(t)$ except for the leakage parameters under conditions

of very high noise and high temporal resolution (protocol 1). This regime is less relevant as all measurements are unreliable under these conditions. For the same reasons the regime of low temporal resolution and high noise level is not of practical interest (upper right corner of Fig.3.14).

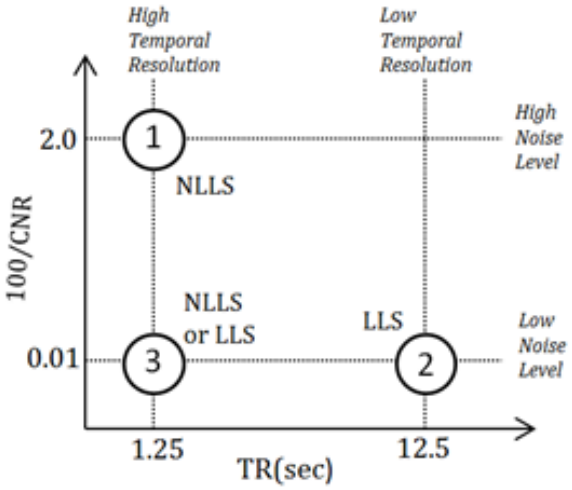

Figure 3.14: Summary of the observations regarding accuracy and precision. The figure maps different experimental conditions in the TR - CNR plane showing the location of the three protocols for which the Figures-of-Merit have been simulated (circles) and the different limiting regimes of high/low noise level and high/low temporal resolution (dotted lines). Optimal choices of methods (NNLS, LLS) are indicated next to the respective protocols.

The systematic error of the LLS at higher noise levels is unexpected from an MRI perspective as previous experiences with the linearised modified Tofts model have shown an improved accuracy at higher noise levels [52, 64]. In part, this discrepancy may be due to implementation differences in the NLLS between the current and previous studies [52]. However, it is likely that the effect is mostly due to the added complexity of a 2nd-degree linear model. A key difference with the modified Tofts model is that the linearised equation of the 2CXM or 2CFM contains a second-order derivative. This leads to the double integrals in Eq.(3.26) which effectively add a strong weight on the later time points where little temporal structure is available. As a result the solution becomes less well determined than in the NLLS, where the

first-pass data carry a strong weight due to the high signal values in this regime. This is also consistent with the observation that a weighting factor $W(t) = c_a(t)$ reduces the systematic errors significantly: at high temporal resolution the function $c_a(t)$ is dominated by the first pass where most of the temporal structure can be found. The chosen weighting does not remove the error completely, but alternative weighting strategies have not been explored and could lead to further improvement. An alternative solution that may be worth considering is the use of the differential form combined with temporal filtering to reduce the noise sensitivity [64]. However, it is not clear whether this remains beneficial in second order.

In the nuclear medicine literature it is well-known that LLS methods for 4-parameter 2-compartment models cause a bias in the parameters [49, 59, 58, 57, 65, 66]. There is no a priori guarantee that these observations translate to DCE-MRI (or DCE-CT). Noise levels, temporal resolutions and acquisition times generally lie in entirely different regimes. A more fundamental difference lies in the typical data structure of first-pass DCE-MRI or -CT, where all high-frequency information is stored in a narrow and early time interval. This explains why the weighting effect of the double integration is more significant in DCE-MRI. Nevertheless, our study confirms that LLS at high noise levels causes a bias in all DCE-MRI parameters.

This raises the question of whether the solutions proposed for PET could help to reduce the bias. Feng et al. [57, 49] proposed a generalized linear least-squares (GLLS) method, which has found some use in pixel-based parameter estimation for PET [67]. However, a more recent comparative study indicated that it still exhibits large bias and poor precision at higher noise levels [59]. Zeng et al. [61] proposed a more general weighted integration method to address the problem. Instead of integrating the linear equation (Eq.(3.19)) twice over time, it is multiplied with wavelets $g(t, T)$ on a support $t \in [0, T]$, and integrated once over that interval. Despite appearances, this method is not fundamentally different from double integration, and it is identical when the wavelets are chosen as $g(t, T) = T - t$. This follows from the identity:

$$\int_0^T dt\,(T-t)f(t) = \bar{\bar{f}}(T). \tag{3.38}$$

Hence, one would not expect an improved performance. Zeng et al. [61] did not observe a bias, but the scope of their simulations was limited and restricted to data with low temporal resolution and relatively low noise levels. This corresponds roughly to the low-noise regime where we have also observed that the LLS is more

robust (lower right corner of Fig.3.14). The wavelet-based method does have the advantage that different families of wavelets can be used, but there is no evidence that this would eliminate the observed bias.

Another question that could be asked is whether the LLS problem suffers from ill-posedness and could benefit from regularisation. At first glance, the strong noise sensitivity of a parameter like T_e could be seen as an indication thereof, but the problem appears in the NLLS as well. In this case the sensitivity of T_e most likely reflects a limitation of the data: the "population" contains a case (patient 4) with a T_e-value (214s) that is relatively close to the acquisition time Tacq (300s). In that case the washout of tracer is not well-resolved and its transit time cannot be determined reliably except with ideal noise-free data.

This work also raised a number of issues that require further study. One important point is the effect of weighting, Eq.(3.33), and the choice of a suitable weight $W(t)$. Our purpose here was to demonstrate that adding a weight may have a significant effect on the results, but the choice of an optimal weighting strategy is a non-trivial issue that deserves a more in-depth study. Possibly a sensitivity analysis involving partial derivatives may be used in selecting an optimal weight [68]. Experience in other areas has demonstrated that a suitable weighting strategy may have a significant impact on the results [69], but it is currently unclear whether these conclusions apply here. A second issue is the risk of data or model errors leading to a situation where no exact solution to Eq.(3.30) exists. In that case the best solution is one with equal transit times (Eq.(3.31)) which is not physiological. It is currently unclear under what conditions exactly this problem may arise. To get some insight we counted the number of times the problem occurred and found that it never happened in any of our simulated data. Possibly the problem may arise when significant model errors are present, but this requires further investigations. A third issue is the role of a delay between artery and tissue. It is a limitation of the method as discussed here that a delay parameter was not included in the model. This is often added to correct for a shift due to upstream AIF sampling [47]. In NLLS approaches a delay is typically determined from a separate procedure at the cost of significant computation times [70]. These methods can easily be adapted to apply to LLS methods as well.

3.8 Conclusion

The LLS method for Tofts model and modified Tofts model is more efficient than the NLLS and has comparable accuracy. The LLS method for solving the 2CXM or 2CFM reduces the computation times by two orders of magnitude, and is at least as accurate and precise as the NLLS at low noise levels. At higher noise levels the LLS becomes exceedingly inaccurate compared to the NLLS, but this may be improved by using a suitable weighting strategy.

Chapter 4

Model-based Motion Correction in DCE-MRI

4.1 Introduction

As outlined in Chapter 2, a major challenge of the image registration in DCE-MRI is related to the contrast variations between image pairs or among temporal sequences caused by the passage of contrast agent. This chapter addresses the challenge of image registration in renal DCE-MRI data. Following a presentation of the existing registration methods for DCE-MRI data, a novel fully-automated pixel-based non-rigid method for registration of free breathing 2D DCE-MRI data is introduced. One problem with non-rigid pixel-based registration algorithms is their high computational cost. Hence, this study aimed to increase computational efficiency of the proposed algorithm by precomputing the gradients of the cost function as well as the coefficients of B-splines. A systematic evaluation of the algorithm using simulated and clinical 2D renal DCE-MRI data is also presented.

4.2 Registration of DCE-MRI Data

4.2.1 Existing Methods

A number of registration methods have been proposed to correct the motion and produce well-aligned features over the time series. Several rigid registration methods are reported in the literature to address the problem of renal DCE-MRI registration. In an early study, Lee et al. [71] manually aligned the contours defined around each kidney. Sun et al. [72] proposed a multi-step approach, where image gradient information was initially used to roughly align the images, followed by a level-set based segmentation of the kidney. Fine registration is then applied onto the segmented images by incorporating regional inhomogeneity of pixel intensities. Zikic et al. [73] explored the use of normalised gradient fields in a template-matching method to correct for rigid motion. The authors here concluded that motion correction based on template matching method was superior to deformable method with a large number of degrees of freedom. A fully automatic registration that corrects for rigid motion was introduced by Song et al. [74]. The authors applied an edge-preserving anisotropic diffusion to pre-process the images, followed by an edge-detection using a 3D dyadic wavelet expansion. Registration is then applied based on Fourier transform. More recently, Positano et al. [75] performed a two-step rigid registration algorithm: first a pre-registration to perform an initial alignment of the image sequences by minimising the sum of the squares of errors between the reference and current images; and second, a registration step by maximising the mutual information between consecutive image frames.

In contrast to the above rigid registration techniques, Sance et al. [76] and other investigators [77] proposed an intensity-based non-rigid registration method. Their registration algorithm consists of two steps: initially, a simple rigid algorithm to correct global geometrical differences, followed by a non-rigid registration algorithm where the transformation is defined by a deformation model based on a grid of control points described by B-splines basis functions to correct also local geometrical differences. A slight adaptation of the deformable non-rigid method by Wang et al. [78] has been applied to renal 3D data by Yang et al. [79]. Work by Merrem et al. [80] modified a non-rigid registration method originally posed for multi-modal image matching [81]. In order to smooth the estimated deformation field at each step, the authors introduced an isotropic Gaussian kernel in combination with the

cross-correlation as a similarity measure. However, this method is sensitive to the size of the smoothing kernel and may lead to misregistration if not selected properly.

Another class of methods are those based on geometric features rather than image intensities. Khalifa et al. [82] proposed a two-step registration method: after affine registration and kidney segmentation, the authors applied a non-rigid registration algorithm which involves a Laplace-based search for point-to-point correspondences between the boundaries of the segmented kidneys. Liu et al. [83] developed a multiscale non-rigid shape-based registration scheme consisting of two steps: (i) segmented geometries of interest with a level set method, (ii) estimated non-rigid deformation by minimizing the shape discrepancy in the vicinity of geometry of interest. More recently, [84] proposed an edge-based image registration method which manually highlights the kidney contour and uses it as a target for aligning all other frames.

None of the above motion correction methods consider the behavior of the time-intensity curves of contrast enhancement. The registration is performed in a pairwise fashion with the selection of the first (or any other) image as the target image, and then register all the other images to the target image. Another variation of pairwise registration is to register temporally adjacent frames: the second image is registered to the first one, the third image is then registered to the previously registered second image and so on. Such an approach is very sensitive to the choice of target image, as images at early time points have very different contrast from images at later time points.

Melbourne et al. [85] proposed a non-rigid technique that does not rely upon the use of segmentation. Principal components analysis was used to create a set of enhancing target images from the unregistered data using a limited number of components. Registration is then performed time-point by time-point to these target images generated using the principal components of the unregistered data. After registration, a new set of synthetic target images were created using the newly registered data. An iterative process of target images generation and registration occurs until stopping criteria are met. This method has been used to register data acquired using repeat breath-hold protocols. However, the authors found that this method depends on the nature of motion and it may fails in the presence of periodic motion as it appears in the principal components along with the contrast changes. Similar to [85], an application in free breathing DCE-MRI has been done by Wollny et al. [86] using

the independent component analysis to decompose data prior registration. More recently, Hamy et al. [87] investigated the use of robust principal component analysis for data decomposition before registration. In this method, contrast changes are assumed to appear in the sparse component and motion in the low rank component of the input data. The algorithm was demonstrated to successfully register liver data acquired using single breath-hold followed by shallow breathing protocol. However, the assumption that motion should appear in the low rank component may be limited when motion elements occur locally over a short period of time [87].

A further approach is to incorporate a pharmacokinetic model into the motion correction process. Adluru et al. [53] developed a work on enhancement-driven registration and tested it in segmented breath hold cardiac MRI. The 3-parameter modified Tofts model is initially fit to the unregistered data to generate target images for registration. Similar to [85], a new set of target images were constructed using the registered data, followed by an iterative process of synthetic targets generation and registration. Buonaccorsi et al. [88] proposed a similar approach based on the 3-parameter modified Tofts model for use on manually delineated tumor volumes of interest. In both studies, registration was simplified by considering only translational motion corresponding to an assumption of tissue rigidity. More recently, Likhite et al. [89] combined the use of a rigid and deformable model based image registration in segmented cardiac perfusion MR images. Similar to [53, 88] the authors used the 3-parameter modified Tofts model to generate target images. The method uses a preliminary rigid registration step where for each frame the previous and next frames are averaged together to generate the target image. This preliminary step corrects for sudden motion between frames. A deformable registration is then followed by the generation of synthetic target images using the modified-Tofts model, as described above.

4.2.2 Aim and Objectives

While the existing tracer-kinetic model-driven registration methods [53, 88, 89] successfully registered DCE-MRI data, they employed a 3-parameter modified-Tofts model without a F_p term. This model is therefore unsuitable for renal DCE-MRI studies. The motivation for this is given by previous studies showing that the 3-parameter modified-Tofts model does not fit the renal data very well [11, 13]. The purposes of the study were to generalize existing tracer-kinetic model-driven regis-

tration methods [53, 88, 89], by using a 4-parameter 2-compartment tracer-kinetic model to generate synthetic target images, followed by non-rigid registration using FFD; and to improve the efficiency of the proposed registration algorithm by precomputing steps to avoid redundant calculations.

4.3 Tracer-Kinetic Model-Driven Registration

4.3.1 Registration Algorithm - Architecture

At a spatial location $\mathbf{x} \in \Omega \subset \mathbb{R}^{2,3}$ on the image domain Ω and time $t \in \{t_1, t_2, \ldots, t_N\}$, the measured tissue concentration is defined by $C(\mathbf{x}, t)$ and the arterial concentration by $c_a(t)$. As stated previously in Chapter 3, the standard method of fitting tracer-kinetic models to the data is the NLLS method. However, this method requires considerable computation time. Therefore, it is impractical in image-wide pixel-by-pixel based parameter estimation. An alternative rapid fitting method is the use of LLS method [44] as introduced in Chapter 3:

$$C(\mathbf{x}, t) = -\alpha(\mathbf{x})\bar{\bar{C}}(\mathbf{x}, t) - \beta(\mathbf{x})\bar{C}(\mathbf{x}, t) + \gamma(\mathbf{x})\bar{\bar{c}_a}(t) + F_p(\mathbf{x})\bar{c_a}(t). \tag{4.1}$$

For more details about the notation of the above equation we refer the reader to Section 3.3.2.

As outlined in Chapter 2, a deformation field is formally a vectorial function $\mathbf{d}_t : \Omega \rightarrow \mathbb{R}^{2,3}$ which typically stores the information on how to transform pixel coordinates $\mathbf{x}$ in measured source image $I_{\text{source}}(\mathbf{x}, t)$ to coordinates in the motion corrected image $I_{\text{corr}}(\mathbf{x}, t)$, defined as:

$$I_{\text{corr}}(\mathbf{x}, t) = I_{\text{source}}(\mathbf{x} + \mathbf{d}_t(\mathbf{x}), t). \tag{4.2}$$

Although the signal intensities (I) are not directly proportional to contrast agent concentration C (see Section 2.3.1), here we assumed a linear relation between I and C. Therefore conversion of I to C is obtained as:

$$C(\mathbf{x}, t) = I(\mathbf{x}, t) - I(\mathbf{x}, 0). \tag{4.3}$$

4.3.2 Registration Algorithm - Implementation

The process of tracer-kinetic model-driven registration algorithm can be described as follows: the breathing induced deformation field is initialized to be zero, i.e. $\mathbf{d}_t(\mathbf{x}) = 0$ and the following steps are iterated. The registration algorithm architecture can be found in Appendices B.1.1 - B.1.3.

Step 1: Create I_{corr} by applying Eq.(4.2).

Step 2: Apply Eq.(4.3) to I_{corr} to get the corrected concentrations

$$C_{\text{corr}}(\mathbf{x}, t) = I_{\text{corr}}(\mathbf{x}, t) - I_{\text{corr}}(\mathbf{x}, 0). \tag{4.4}$$

The $I_{\text{corr}}(\mathbf{x}, 0)$ is estimated as an average over the baseline:

$$I_{\text{corr}}(\mathbf{x}, 0) \cong \frac{1}{n_b} \sum_{t=0}^{n_b} I_{\text{corr}}(\mathbf{x}, t), \tag{4.5}$$

where n_b defines the number of I_{corr} constituting the baseline.

Step 3: Fit Eq.(4.1) time-point by time-point to $C_{\text{corr}}(\mathbf{x}, t)$ to determine estimates of $\alpha_{\text{fit}}(\mathbf{x})$, $\beta_{\text{fit}}(\mathbf{x})$, $\gamma_{\text{fit}}(\mathbf{x})$ and $F_{p_{\text{fit}}}(\mathbf{x})$.

Then, calculate the fit using the C_{corr}, namely,

$$C_{\text{fit}}(\mathbf{x}, t) = -\alpha_{\text{fit}}(\mathbf{x})\bar{\bar{C}}_{\text{corr}}(\mathbf{x}, t) - \beta_{\text{fit}}(\mathbf{x})\bar{C}_{\text{corr}}(\mathbf{x}, t) + \gamma_{\text{fit}}(\mathbf{x})\bar{\bar{c}}_a(t) + F_{p_{\text{fit}}}(\mathbf{x})\bar{c}_a(t). \tag{4.6}$$

The 2CFM fit is performed using a LLS algorithm to produce parameter estimates, as described in Chapter 3. For more details we refer the reader to Appendix B.3.3.

Step 4: Generate time series of target images from the fitted parameters (from Step 3) which include the signal variations due to contrast enhancement, but display no motion from time-point to time-point, see Appendix B.3.2. The time series of target

images is obtained using Eq.(4.6):

$$I_{\text{target}}(\mathbf{x}, t) = I_{\text{corr}}(\mathbf{x}, 0) + C_{\text{fit}}(\mathbf{x}, t). \tag{4.7}$$

Step 5: Proceeding time-point by time-point, each I_{corr} frame is registered to its corresponding I_{target} frame using FFD non-rigid registration. The process of registration can be formulated as a minimization problem:

$$\hat{\mathbf{d}}_t(\mathbf{x}) = \arg\min_{\mathbf{d}} \mathcal{C}\big(I_{\text{target}}(\mathbf{x}, t), I_{\text{corr}}(\mathbf{x}, t)\big), \tag{4.8}$$

where $\hat{\mathbf{d}}_t$ denotes the optimal solution and the cost function $\mathcal{C}$ is the similarity metric. The implementation details of cost function can be found in Section 4.3.2.1.

4.3.2.1 Cost Function

The cost function, $\mathcal{C}$, in Eq.(4.8) equals the sum of squared difference similarity metric, namely SSD:

$$\mathcal{C}\big(I_{\text{target}}(\mathbf{x}, t), I_{\text{corr}}(\mathbf{x}, t)\big) = \frac{1}{2} \sum_{\mathbf{x} \in \Omega} \big(I_{\text{target}}(\mathbf{x}, t) - I_{\text{corr}}(\mathbf{x}, t)\big)^2. \tag{4.9}$$

The deformation is obtained by minimizing the similarity measure between the I_{target} and I_{corr} using a gradient-descent method as introduced in Section 2.6.3, with analytically calculated gradients and a backtracking line search. The explicit derivation of the analytical gradients will be explained below in Section 4.3.2.2. The backtracking routine attempts to find a step size for reducing the value of the function $\mathcal{C}$ given the current point and a direction. At each optimization cycle, the backtracking is terminated if the step to the new point is so small that it triggers termination in the main algorithm. In the default implementation, iterations are repeated until the step size falls in precision of 1 pixel. Failing that, the algorithm will terminate when a certain number of iterations is reached, say 300. We refer the reader to Appendix B.3.6 for more details of this process.

4.3.2.2 Gradient Computation

Let us denote the image domain as the rectangle $\Omega = \{(x, y) \,|\, 0 \leq \ x < L_x, 0 \leq y < L_y\}$. Let $n_x \times n_y$ be a mesh of control points with uniform spacing Δ overlaid on image Ω, see Figure 4.1. The resolution of the image is defined as $\frac{L_x}{\delta_x} \times \frac{L_y}{\delta_y}$ where δ is the uniform space between the pixels, and the resolution of the deformation field is defined as $\frac{L_x}{\Delta_x} \times \frac{L_y}{\Delta_y}$. The $\mathbf{d}_t$ at any given location $\mathbf{x}$ can be defined as:

$$\mathbf{d}_t^c(\mathbf{x}) = \sum_{i \in I_d} \mathbf{d}_{t_{(i)}}(\mathbf{x}) B_i^d(\mathbf{x}), \tag{4.10}$$

where $\mathbf{d}^c$ is a continuous version of the deformation field, I_d is a 2-dimensional array representing the set of all control points coordinates in the deformation field, and B^d is a tensor product of linear B-splines at the current resolution of the deformation field grid, as introduced earlier in Section 2.6.1.3.

In a similar way, we can define I_{source} as:

$$I_{\text{source}}^c(\mathbf{x}, t) = \sum_{j \in \mathbf{I}_\text{s}} I_{\text{source}_{(j)}}(\mathbf{x}, t) B_j^s(\mathbf{x}), \tag{4.11}$$

where I_{source}^c is a continuous version of the source image, $\mathbf{I}_\text{s}$ is an N-dimensional discrete set of all pixel coordinates in the source image, and B^s is a tensor product of linear B-splines at the current resolution of the deformation field grid.

For the analytical calculation of the gradients the first step is to rewrite Eq.(4.2). Substituting Eqs. (4.10) and (4.11) into Eq.(4.2) yields:

$$I_{\text{corr}}^c(\mathbf{x}, t) = \sum_{j \in \mathbf{I}_\text{s}} I_{\text{source}_{(j)}}(\mathbf{x}, t) B_j^s\Big(\mathbf{x} + \sum_{i \in \mathbf{I}_d} \mathbf{d}_{t_{(i)}} B_i^d(\mathbf{x})\Big), \tag{4.12}$$

where I_{corr}^c is a continuous version of the corrected image I_{corr}.

The gradient is with respect to the optimisation variables, i.e. the control points of $\mathbf{d}_t$. For reasons of clarity and ease of presentation, let us write $\mathbf{d}_t$ in terms of its coordinates $(d_{x,t}, d_{y,t})$. To compute the gradient we take the derivative of the cost function Eq.(4.9) with respect to the parameters of $\mathbf{d}_t$ in the x-direction to get:

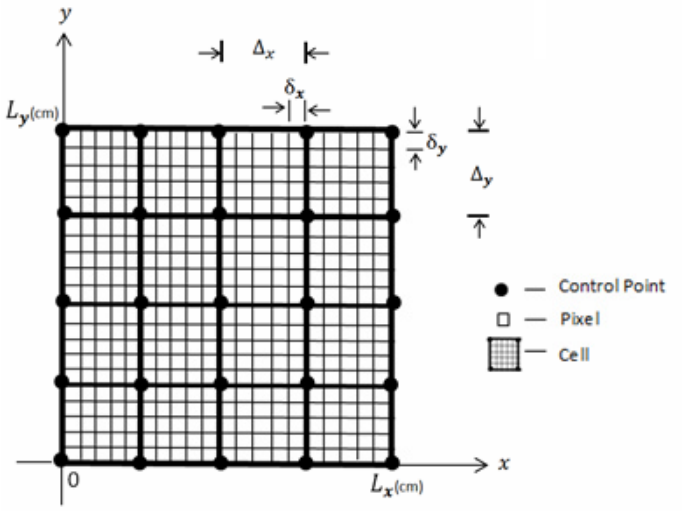

Figure 4.1: Example showing high-resolution pixels that contribute to a low-resolution pixel. The grid in light font represents the true underling high-resolution image (I_{source}) and the grid in bold font is the low-resolution $\mathbf{d}_t$. Note the different grid sizes for light font grid and bold font grid.

$$\frac{\partial \mathcal{C}}{\partial d_{x_i,t}} = -\sum_{\mathbf{x}\in\Omega} \left(I_{\text{target}}(\mathbf{x},t) - I^c_{\text{corr}}(\mathbf{x},t)\right) \frac{\partial I^c_{\text{corr}}(\mathbf{x},t)}{\partial d_{x_i,t}}. \tag{4.13}$$

The partial derivative of I^c_{corr} can be calculated from Eq.(4.12) as:

$$\begin{aligned}
\frac{\partial I^c_{\text{corr}}(\mathbf{x},t)}{\partial d_{x_i,t}} &= \sum_{j\in\mathbf{I}_s} I_{\text{source}_{(j)}}(\mathbf{x},t) \frac{\partial B^s_j}{\partial x}\Big(\mathbf{x}+\mathbf{d}^c_t(\mathbf{x})\Big) B^d_i(\mathbf{x}) \\
&= B^d_i(\mathbf{x}) \sum_{j\in\mathbf{I}_s} I_{\text{source}_{(j)}}(\mathbf{x},t) \frac{\partial B^s_j}{\partial x}\Big(\mathbf{x}+\mathbf{d}^c_t(\mathbf{x})\Big) \\
&= B^d_i(\mathbf{x}) \frac{\partial}{\partial x} \sum_{j\in\mathbf{I}_s} I_{\text{source}_{(j)}}(\mathbf{x},t) B^s_j\Big(\mathbf{x}+\mathbf{d}^c_t(\mathbf{x})\Big).
\end{aligned} \tag{4.14}$$

Using Eq.(4.12) the above formula leads to:

$$\frac{\partial I^c_{\text{corr}}(\mathbf{x},t)}{\partial d_{x_i,t}} = B^d_i(\mathbf{x}) \frac{\partial I^c_{\text{corr}}(\mathbf{x},t)}{\partial x}. \tag{4.15}$$

The partial derivatives in y-direction are obtained in a similar fashion.

The gradient in the x-direction for a certain control point, i, is then given by:

$$\frac{\partial \mathcal{C}}{\partial d_{x_i,t}} = -\sum_{\mathbf{x}\in \mathrm{loc}(i)} \big(I_{\mathrm{target}}(\mathbf{x},t) - I_{\mathrm{corr}}(\mathbf{x},t)\big) B_i^d(\mathbf{x}) \, \frac{\partial I_{\mathrm{corr}}^c(\mathbf{x},t)}{\partial x}, \tag{4.16}$$

where the $\mathrm{loc}(i)$ defines the neighborhood around the control point i. Similarly the gradient in the y-direction for a certain control point, i, is then given by:

$$\frac{\partial \mathcal{C}}{\partial d_{y_i,t}} = -\sum_{\mathbf{x}\in \mathrm{loc}(i)} \big(I_{\mathrm{target}}(\mathbf{x},t) - I_{\mathrm{corr}}(\mathbf{x},t)\big) B_i^d(\mathbf{x}) \, \frac{\partial I_{\mathrm{corr}}^c(\mathbf{x},t)}{\partial y}. \tag{4.17}$$

Let us define the residual term in the above Eqs. (4.16) and (4.17) as follows:

$$\mathrm{Res}(\mathbf{x},t) = I_{\mathrm{target}}(\mathbf{x},t) - I_{\mathrm{corr}}(\mathbf{x},t). \tag{4.18}$$

Substituting Eq.(4.18) into Eqs. (4.16) and (4.17) leads to:

$$\frac{\partial \mathcal{C}}{\partial d_{x_i,t}} = -\sum_{\mathbf{x}\in \mathrm{loc}(i)} \mathrm{Res}(\mathbf{x},t) B_i^d(\mathbf{x}) \, \frac{\partial I_{\mathrm{corr}}^c(\mathbf{x},t)}{\partial x}, \tag{4.19}$$

$$\frac{\partial \mathcal{C}}{\partial d_{y_i,t}} = -\sum_{\mathbf{x}\in \mathrm{loc}(i)} \mathrm{Res}(\mathbf{x},t) B_i^d(\mathbf{x}) \, \frac{\partial I_{\mathrm{corr}}^c(\mathbf{x},t)}{\partial y}. \tag{4.20}$$

4.3.2.3 Precomputation of Gradient

One of the most demanding parts of the algorithm from a computational point of view is the computation of the gradients of the cost function, Eq.(4.9). However, due to the compact support of the B-spline functions moving any control point of the deformation field affects only its neighborhood. This means that the gradient outside the neighborhood of the certain control point is not affected. Therefore, the gradient computation deals with a small fraction of the image data only and thus has to evaluate the transformation only for a small number of pixels at a time, as stated above in Eqs. (4.16) and (4.17). In addition, the residual term (Eq.(4.18)) does not depend upon the partial derivatives with respect to x nor y. Having precompute this term only once we can further used it later in the computation of the gradients

to avoid redundant calculations. For more details we refer the reader to Appendices B.2.3 and B.2.4.

4.3.2.4 Precomputation of B-spline Coefficients

Another source of redundant calculations caused is the derivation of the dense deformation field. This procedure involves computing the weighted averages of the control point displacements in a neighborhood area around each pixel. This neighborhood consists of two control points in each dimension. The linear B-splines transformation that is to be implemented is restated for convenient reference. For a given control point displacement $\mathbf{d}$, the displacement of a pixel $\mathbf{x} = (x, y)$ in 2D is given by

$$\mathbf{d}_{\text{linear}}(\mathbf{x}) = \sum_{l=0}^{1} \sum_{m=0}^{1} B_l(x - x_i) B_m(y - y_i) \mathbf{d}_{i+l,j+m}, \tag{4.21}$$

where (i, j) is the index of control point cell containing $\mathbf{x}$. As Equation (4.21) has to be evaluated in the whole image domain this cause a source of redundant calculations that can be avoided in a straightforward implementation. At each resolution level the registration process is repeated several times. However, at a particular resolution level the size of the deformation field does not change. As a result, the B-splines basis functions values $B_l(x - x_i)$ and $B_m(y - y_i)$ can be precomputed at first iteration and reused for subsequent iterations. For more detailed information about the implementation of this step we refer the reader to Appendix B.2.2.

The formula for bilinear interpolation (Eq.(2.53)) introduced in Chapter 2 can also be written in terms of I_{corr} and I_{source}. For an arbitrary point (x, y) we then obtain:

$$\begin{aligned} I_{\text{corr}}(x, y) = (1 - u)(1 - v)\, I_{\text{source}_{(i,j)}} + u(1 - v)\, I_{\text{source}_{(i+1,j)}} \\ + (1 - u)v\, I_{\text{source}_{(i,j+1)}} + uv\, I_{\text{source}_{(i+1,j+1)}}. \end{aligned} \tag{4.22}$$

The displacement of an arbitrary point (x, y) on the motion corrected image, I_{corr}, is given by:

$$\begin{aligned} I_{\text{corr}}(x,y) = I_{\text{source}}(x_i,y_i) + (x-x_i)\frac{\Delta I_{\text{source}}}{\Delta x}(x_i,y_i) + (y-y_i)\frac{\Delta I_{\text{source}}}{\Delta y}(x_i,y_i) \\ +(x-x_i)(y-y_i)\frac{\Delta^2 I_{\text{source}}}{\Delta x \Delta y}(x_i,y_i). \end{aligned} \tag{4.23}$$

One can prove that the Taylor series expansion in Eq.(4.23) is equivalent to bilinear interpolation formula as given in Eq.(4.22) by calculating the numerical derivatives of the source image, I_{source} with finite difference approximation. The derivation is fairly straightforward and thus an explicit proof is not presented.

A last source of redundant calculations that can be avoided to reduce the computational time, is related to the calculation of the numerical derivatives in Eq.(4.23). The source image, I_{source} does not change during the registration process and is independent of the updated deformation field. Consequently, the numerical derivatives of the I_{source} can precomputed only once and can be used for any other point that has to be calculated in the current square cell, see Figure 4.1.

4.3.2.5 Multiresolution Strategy

In order to improve convergence and to reduce the computational cost, we have implemented a multiresolution approach in which the resolution of the $\mathbf{d}_t$ is increased in a coarse-to-fine manner. In our implementation, the image size does not change at each level. The resolution of the $\mathbf{d}_t$ defines the number of degrees of freedom, and, consequently the complexity of the deformation model. The algorithm is initially performed using a coarse deformation field to capture large-scale registration and then progressively increased. The resolution is changed by a factor of two between continuous levels. The default implementation of the algorithm proceeds progressively starting with a deformation field of size $2^1 \times 2^1$ and terminates when $2^5 \times 2^5$ resolution is reached. A deformation field of size $2^2 \times 2^2$ has 5×5 control points as illustrated in Figure 4.1. At each resolution level, the deformation field obtained from the previous level is interpolated to initialize the next level, using bilinear interpolation. Fewer iterations are allowed at finer resolution levels where the computation

is more expensive. The detailed algorithm referred to multiresolution procedure can be found in Appendix B.1.1.

4.4 Registration of DCE-MRI using Tracer-Kinetic Model-Driven Registration

4.4.1 Simulated Data

As mentioned in the introduction, the proposed image registration algorithm has systematically been evaluated in simulated data. A synthetic phantom of the kidneys was used to generate data (120 dynamics, 1.1s intervals, matrix size 135×135). The kidney phantom is generated using the equation of an ellipse, given by:

$$\frac{(x-h)^2}{a^2} + \frac{(y-k)^2}{b^2} \leq 1, \tag{4.24}$$

where a is the radius along the x-axis, b is the radius along the y-axis and h, k are the x, y coordinates of the ellipse's center. For each region of the kidney phantom (see Fig.4.2) the values of a, b and h were varied as shown in Table 4.1.

Region of Kidney Phantom	a	b	h	k
1	15	10	38	64
2	32	20	38	64
3	37	22	38	64
4	41	26	38	64
5	38	21	100	64
6	33	18	100	64
7	16	10	100	64

Table 4.1: Parameter values used in Eq.(4.24) for each region of the synthetic kidney phantom in Figure 4.2.

A literature based AIF was used [23], prepadded with zeroes to create a 15s baseline. Contrast enhancement was applied using the 2CFM and literature pharmacokinetic parameters [62], as summarized in Table 4.2. Gaussian noise and motion were added

to improve the realism of the data. CNR is defined as the ratio of peak arterial concentration to the standard deviation (SD) of the noise, i.e. CNR = $\max(C_a)$/SD. We chose to use CNR because in DCE-MRI this is a better measure of the noise level than SNR as the analysis is performed on signal changes rather than on absolute signal values. Two different types of motion were applied to motion-free synthetic data: sinusoidal vertical shifts (rigid) were added as defined by

$$\mathbf{d}_{(rigid)} = \mathbf{x} + A\sin(2\pi t/T)\hat{\mathbf{y}}, \tag{4.25}$$

where A is the amplitude of motion ($A = 12$), T is the period of breathing ($T = 4$) and $\hat{\mathbf{y}}$ is a unit vector. Non-rigid motion was derived from the inverse deformation fields from clinical data.

Region of Kidney Phantom	F_p (ml/min/100ml)	T_p (sec)	F_T (ml/min/100ml)	T_T (sec)
1	26	6.5	3	110
2	70	7.0	6	117
3	50	9.0	6	125
4	10	9.5	1	130
5	26	7.0	3	110
6	70	9.0	6	117
7	26	9.5	3	132

Table 4.2: Ground truth parameter values for each region of the synthetic kidney phantom in Figure 4.2.

4.4.2 Clinical Data

DCE-MRI was performed using a 3T scanner (Philips Achieva, Best, Netherlands) and a 2D Saturation-Recovery Turbo-Flash sequence with linear encoding of k-space. A 2 channel body transmit coil was employed for homogeneous signal transmission and data were acquired using 18 channel torso coil. Four slices (3 coronal,1 axial) were acquired at a temporal resolution of 1.1 second. Other imaging parameters were as follows: acquisition matrix 116 (phase) × 135 (read), number of dynamics 250, echo time 1.63 milliseconds, repetition time 3.6 milliseconds, bandwidth 900 Hz, inversion time 148 milliseconds, flip angle 12°, slice thickness 7 mm, SENSE

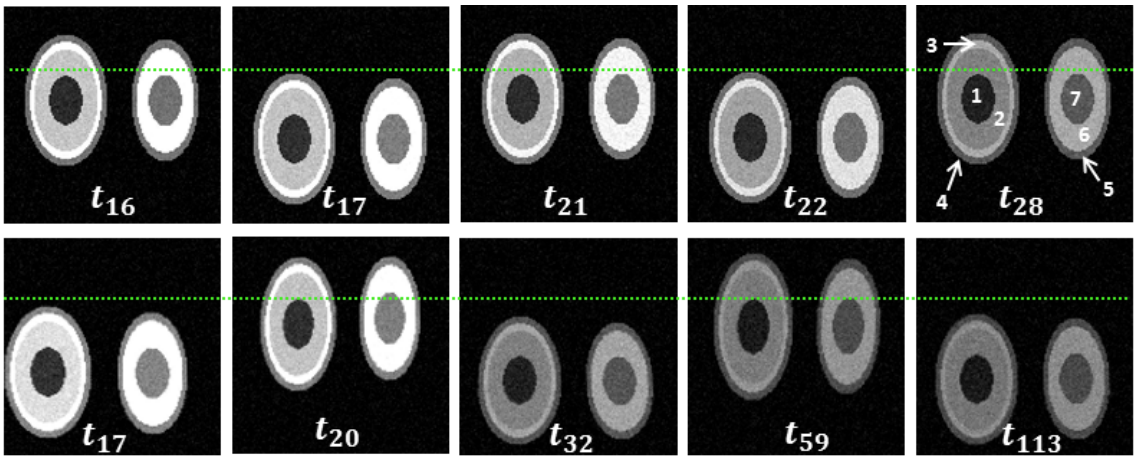

Figure 4.2: **Top row:** Simulated data with rigid motion. **Bottom row:** Simulated data with non-rigid motion.

factor 2.4, field of view 375 × 440 mm^2 with an in-plane resolution of 3.2 × 3.2 mm^2.

Free breathing acquisitions were performed. We examined 5 subjects with Gd-tetraazacyclododecane tetraacetic acid (Gd-DOTA) with a dosage of 0.1ml/kg body weight. In all DCE-MRI data the AIF is measured in the aorta which is stable in the axial slice during breathing motion.

4.4.3 Optimisation

To examine the influence of the registration algorithm as a function of its inputs we varied the settings of the default implementation using simulated and real DCE-MRI data. These inputs comprise the algorithm's free parameters which are : 1) the convergence precision in number of pixels; 2) the maximum number of steps required for gradient-descent method to reach the minimum; 3) the highest resolution level of $\mathbf{d}_t$; and 4) the number of iterations necessary at each resolution level. The precision free parameter tested under various values ranges in between 0.1 and 5. We used a coarse-to-fine approach with the resolution of $\mathbf{d}_t$ ranging between $2^1 \times 2^1$ and $2^5 \times 2^5$ and iterated 5 times each. In the default implementation the input parameters were as follows: 1) convergence precision was set to 1, 2) maximum number of steps was set to 300, 3) highest resolution level was set to $2^5 \times 2^5$ and 4) the number of iterations at each resolution level was set to 5. The appropriate parameter settings

depend on the individual data set and have to be adjusted by the user. It should be mentioned that the free parameters may influence the time complexity of the algorithm.

4.4.4 Evaluation of Registration Algorithm

The assessment of registration accuracy was performed using both synthetic phantom and real DCE-MRI data. For synthetic phantom the registration accuracy is quantitatively assessed by a relative error metric. It is measured between the reconstructed P_i and corresponding known ground truth parameters $P = F_p, T_p, PS, T_e$:

$$E_i(P) = \frac{P_i - P}{P} \times 100 \tag{4.26}$$

For real DCE-MRI data, the registration accuracy was evaluated qualitatively by visual comparison of corrected and uncorrected images. Time-cut images were generated representing the temporal evolution of a pixel-wide line across all time frames as well as time-intensity curves of the signal and the model fit based on manually selected tissue ROI.

The algorithm was implemented in IDL 6.4 (Exelis VIS, Boulder, CO) conducted on a standard desktop PC with a 3.4GHz Intel Core processor and 32GB memory.

4.4.5 Registration Results

4.4.5.1 Effect of Parameter Setting

To examine the influence of the free parameters on image registration and calculation time, we varied the settings of the default implementation of the proposed algorithm in both simulated and clinical data. In study with the simulated data we examined the case when non-rigid motion was added to the data. In study with clinical data we chose to examine the data from Subject 3 as it appeared to be the most challenging case in terms of motion.

4.4.5.1.1 Effect of Precision Value

Figure 4.3 shows the comparison of the effect of registration at a wide range of precision values, ranging from 0.1 to 5.0. For each precision value the registration process was iterated 5 times. The size of the deformation field was fixed and set to $2^2 \times 2^2$. This figure illustrates the error distribution after motion correction for the 4-parameters, namely $F_p, T_p, PSandT_e$. The circles indicate the median relative parameter error for all the pixels in the image, and the error bars correspond to the 75% range. The result shows an increase of the error with respect to ground truths at higher precision values. Improved F_p maps representation can be seen when the precision value was set to 0.1 or 1.0. The effect of computation cost by alternating the precision value of the algorithm is presented in Table 4.3. Smaller precision values led to an increase computation cost as more steps are performed in the optimisation step compared to higher values. Similar observations can be made from registration results of clinical data in Figure 4.4 and Table 4.4. From Figure 4.4 one should notice that organ boundaries are originally strongly blurred because of motion, but sharply delineated after motion correction when the precision value was set to 0.1 or 1.0. The results show an optimal registration in terms of quality and speed when the precision is 1.0. This value was used in all subsequent simulation studies.

Precision Value	No. of Steps	Computational Time (min)
0.1	72	3.50
1.0	53	1.76
2.0	26	0.60
3.0	21	0.48
4.0	20	0.47
5.0	18	0.45

Table 4.3: Comparison of precision values for motion correction using a deformation field of size $2^2 \times 2^2$. The table shows the total number of steps and the computational time (in minutes) at each precision value respectively for the simulated data corrupted with non-rigid motion.

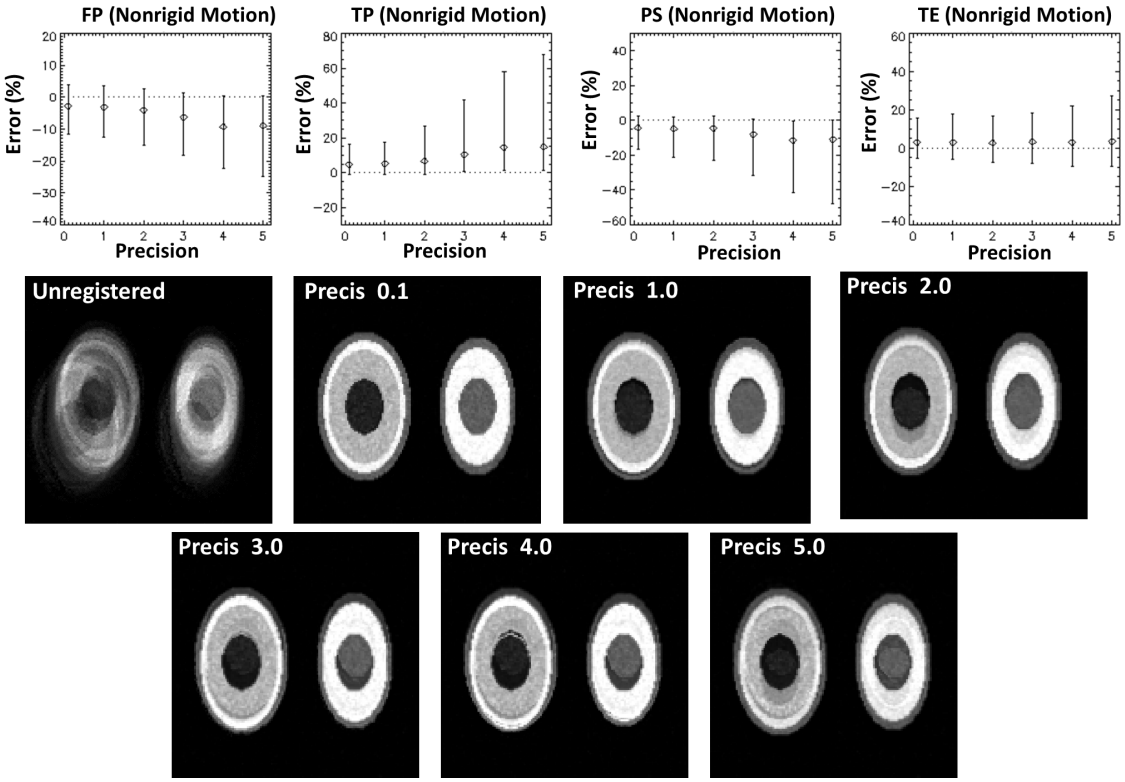

Figure 4.3: **Top row:** Error distribution after motion correction for the 4-parameters at various precision values. The circles indicate the median relative parameter error for all the pixels in the image, and the error bars represent the 75% range. **Subsequent Rows:** Plasma flow (F_p) map of the simulated data before, and, after motion correction for each precision value.

Precision Value	No. of Steps	Computational Time (min)
0.1	114	90.1
1.0	64	31.6
2.0	38	15.5
3.0	23	7.40
4.0	21	7.35
5.0	20	7.30

Table 4.4: Comparison of precision values for motion correction using a deformation field of size $2^2 \times 2^2$. The table shows the total number of steps and the computational time (in minutes) at each precision value respectively for Subject 3.

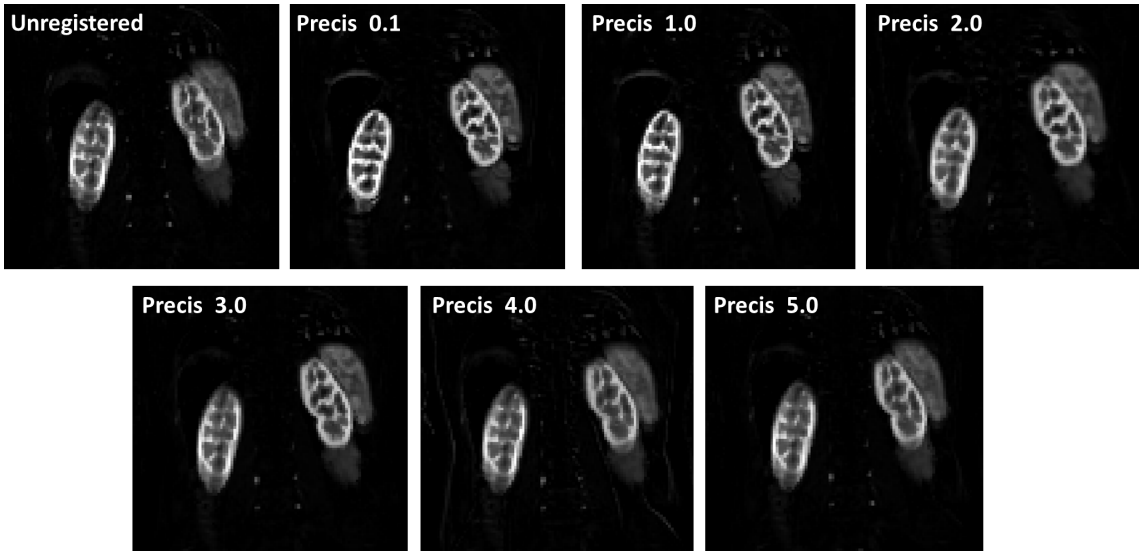

Figure 4.4: F_p map of the Subject 3 data before, and, after motion correction for each precision value. Motion correction was performed on the original image size. Images cropped from 136×136 to 76×76 for visibility.

4.4.5.1.2 Effect of Resolution Level

Performance of the proposed registration algorithm at a wide range of resolution levels was also tested. The convergence precision value was set to 1.0 and 5 iterations performed at each resolution level. Figure 4.5 illustrates the error distribution after motion correction for the 4-parameters at various resolution levels ranging from $2^1 \times 2^1$ (very coarse) to $2^5 \times 2^5$ (very fine). The figure demonstrates that the registration accuracy and precision, as measured by the relative error, improves at finer resolution levels. One can note that both accuracy and precision do not really improve at last resolution level. The figure shows also the F_p maps before and after motion correction at each resolution level. Improved F_p maps representation can be observed at finer resolution levels. Table 4.5 shows the computational time with respect to each resolution level. The table shows that the computational time decreases dramatically as the resolution level decreases. Similar to simulated data the effect of resolution was also tested on clinical data. Qualitative registration results of Subject 3 are presented in Figure 4.6. The registration results show a decrease in blurring caused by breathing motion as the resolution level increases. Similar to simulated data no significant improvement observed in last resolution level. The effect of computation cost by alternating the resolution levels of the registration algorithm is presented in Table 4.6. Similarly to simulated data the total computational time increases as the resolution level increases. The results show an optimal registration in terms of quality and speed when the resolution level was $2^3 \times 2^3$. This value was used in all subsequent simulation studies.

Resolution Level	Computational Time (min)
2^1	1.97
2^2	3.00
2^3	4.45
2^4	9.56
2^5	13.89

Table 4.5: Comparison of resolution levels for motion correction using precision of 1.0. The table shows the total computational time (in minutes) at each resolution level respectively for the **simulated data** corrupted with non-rigid motion.

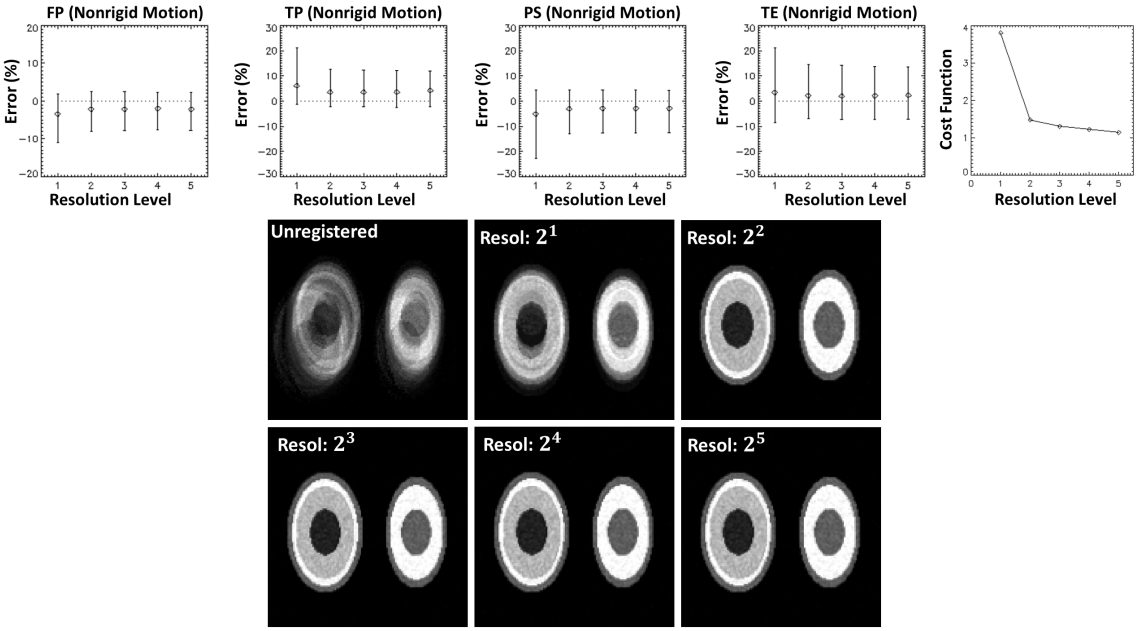

Figure 4.5: **Top row:** Error distribution after motion correction for the 4-parameters at various resolution levels ranging from $2^1 \times 2^1$ (very coarse) to $2^5 \times 2^5$ (very fine). **Subsequent Rows:** Plasma flow (F_p) map of the simulated data before, and, after motion correction for each resolution level.

Resolution Level	Computational Time (min)
2^1	1.7
2^2	7.5
2^3	19.9
2^4	31.6
2^5	150

Table 4.6: Comparison of resolution levels for motion correction using precision of 1.0. The table shows the total computational time (in minutes) at each resolution level respectively for Subject 3.

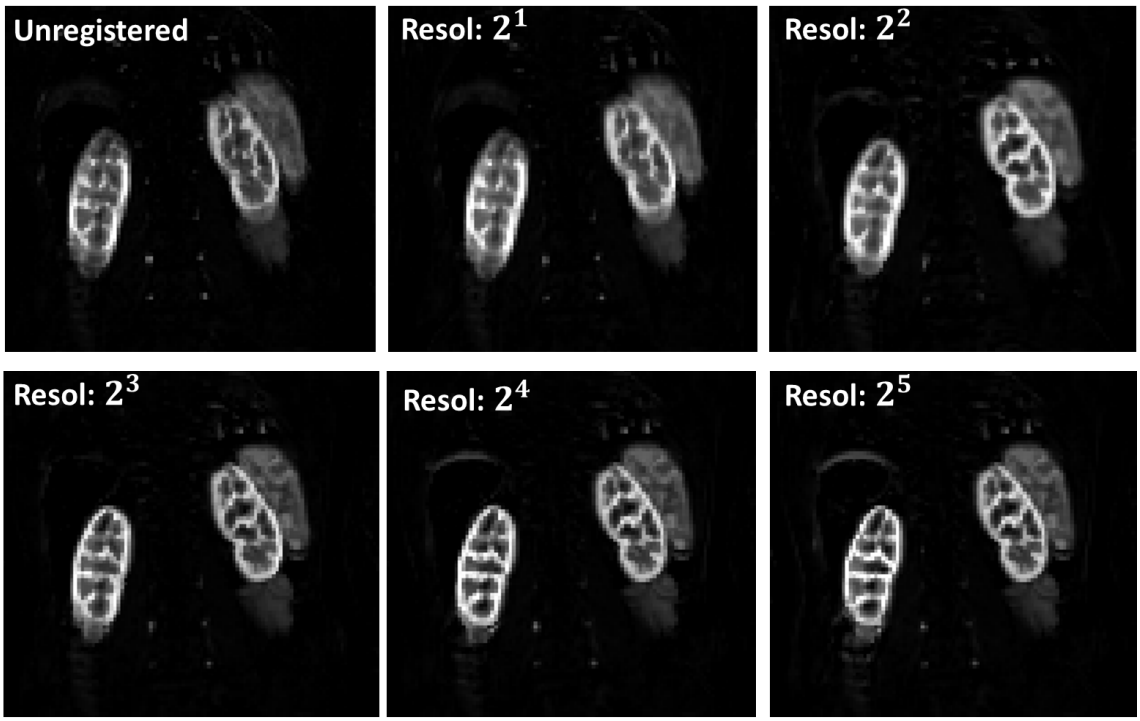

Figure 4.6: F_p map of the Subject 3 data before, and, after motion correction for each resolution level. Motion correction was performed on the original image size. Images cropped from 136×136 to 76×76 for visibility.

4.4.5.1.3 Effect of Number of Iterations

Finally we tested the performance of the proposed algorithm at different number of iterations. In this case, the precision value of 1.0 and the resolution level of $2^3 \times 2^3$ was kept fixed. Figure 4.7 illustrates the comparison of the effect of registration at a wide range of iteration numbers, ranging from 1 to 7. The figure shows that the accuracy and precision of the algorithm improves with increasing iterations in all parameters. The greatest gain occurs in the first 2 iterations where after 5 iterations the relative error does not seem to reduce. One should also notice that F_p parameter maps are not notably improved after the fifth iteration. The effect of number of iterations was also tested on clinical data. Qualitative registration results of Subject 3 are presented in Figure 4.8. The registration results show a decrease in blurring of the F_p maps caused by breathing motion, as the number of iterations increases. Similar to simulated data, no significant improvement is observed on F_p parameter maps after the fifth iteration. Thus, this value was used in all subsequent simulation studies.

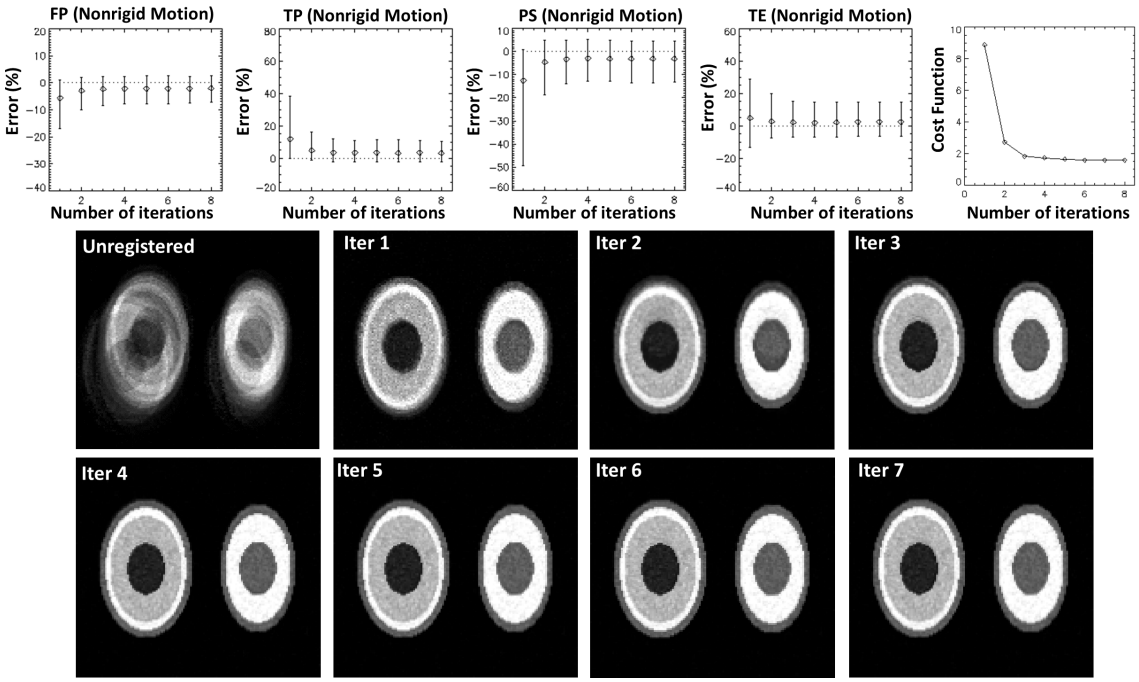

Figure 4.7: **Top row:** Error distribution after motion correction for the 4-parameters with respect to number of iterations, alongside with the cost function $\mathcal{C}$. The circles indicate the median relative parameter error for all the pixels in the image, and the error bars represent the 75% range. **Subsequent Rows:** Plasma flow (F_p) map of the simulated data before, and, after motion correction at each iteration.

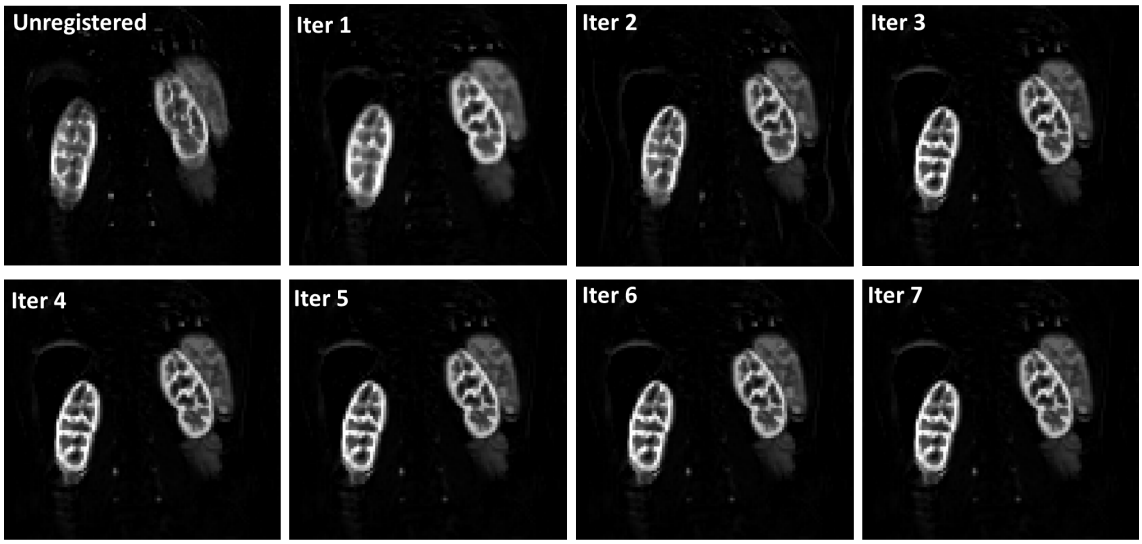

Figure 4.8: F_p map of the Subject 3 data before, and, after motion correction at each iteration. Motion correction was performed on the original image size. Images cropped from 136×136 to 76×76 for visibility.

4.4.6 Evaluation of Registration Performance

Figure 4.9 illustrates the results obtained after registration of the simulated data corrupted with rigid and non-rigid motions. The results show that the algorithm removes the motion without affecting the signal intensities. Similar observation can be made in Figure 4.10. This figure shows that we achieved accurate registration results as demonstrated through the different time frames.

Figure 4.11 shows the relative error of the 4-parameters obtained before motion correction of the simulated data for a wide range of CNRs starting from 50 (very low) to 1000 (very high). The relative error is calculated with respect to ground truths for: no motion, rigid motion and non-rigid motion. The figure shows that the uncorrected motion strongly reduces the accuracy and precision of all parameters in all three cases.

Figure 4.12 shows the relative error of the 4-parameters obtained after motion correction of the simulated data for a wide range of CNRs starting from 50 (very low) to 1000 (very high). The relative error is calculated with respect to ground truths for: no motion, rigid motion and non-rigid motion. In all three cases, the registration algorithm leads to a reduction of the motion induced error.

Figures 4.13−4.17 show the effect of registration in 5 renal DCE-MRI datasets. Time-cut images of the unregistered and registered data demonstrate that misalignments were reduced after registration in all cases. These figures show also the effect of motion correction on the temporal profiles. Original time-intensity curves of the tissue ROI show large respiratory signal changes which showed an increased smoothness after motion correction in all subject cases.

Comparison of the performance of the proposed algorithm using the modified-Tofts model and 2CFM is also presented. Figure 4.18 illustrates the effect of motion correction at different time-points using the modified-Tofts model and 2CFM on simulated data. Similarly, Figure 4.19 illustrates the effect of motion correction at different time-points using the modified-Tofts model and 2CFM on clinical data of Subject 3. From both figures it can be observed that the modified-Tofts model appears to be limited compared to 2CFM during the wash in phase. Comparison of the temporal profiles on both simulated and clinical data using the modified-Tofts model and 2CFM are presented in Figures 4.20 and 4.21, respectively. Original time-intensity curves show large respiratory signal changes which notably reduce

after registration.

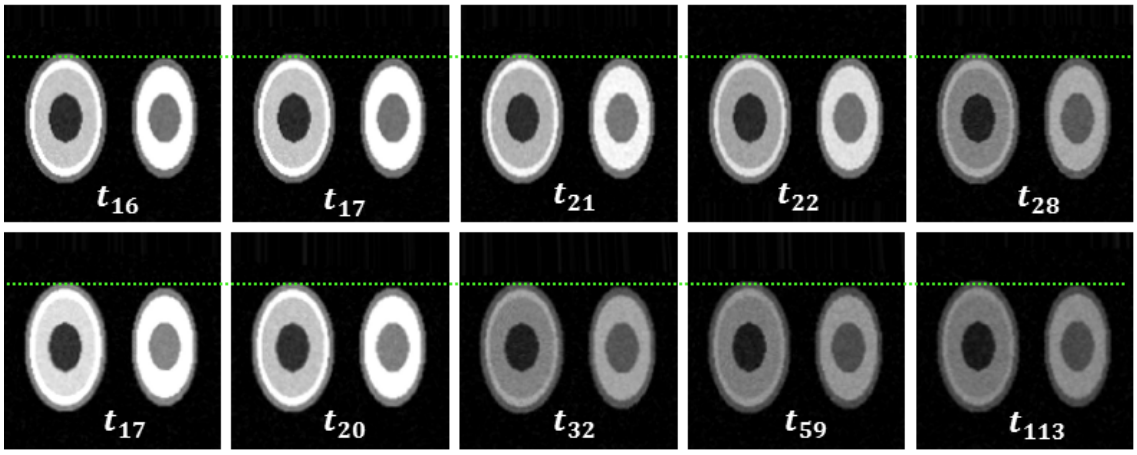

Figure 4.9: Illustration of the effect of motion correction at different time-point, compare with Figure 4.2. **Top row:** Simulated data corrupted with rigid motion after registration. **Bottom row:** Simulated data corrupted with non-rigid motion after registration.

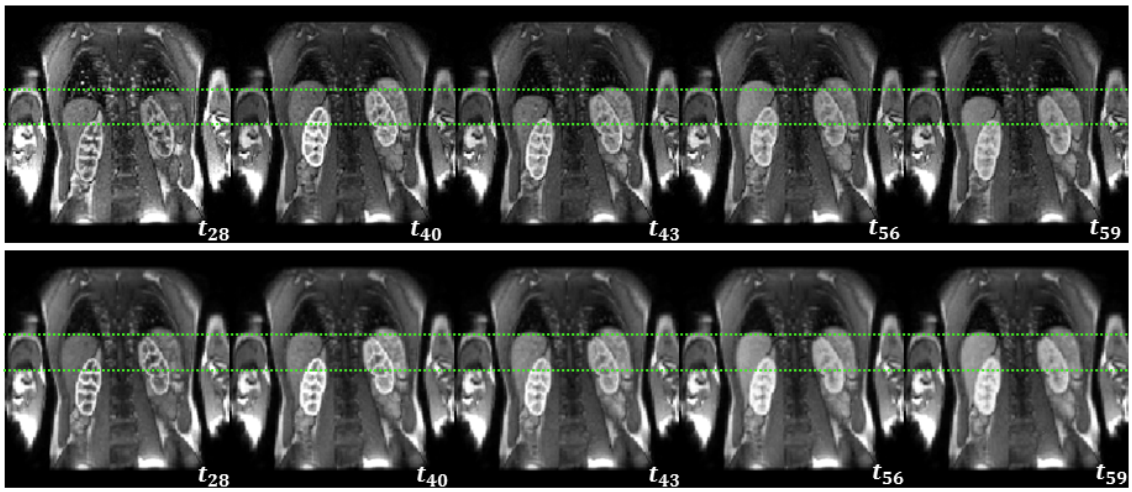

Figure 4.10: Illustration of the effect of motion correction at different time-point. **Top row:** Original data of Subject 3 with frame indices. **Bottom row:** Subject 3 data after motion correction.

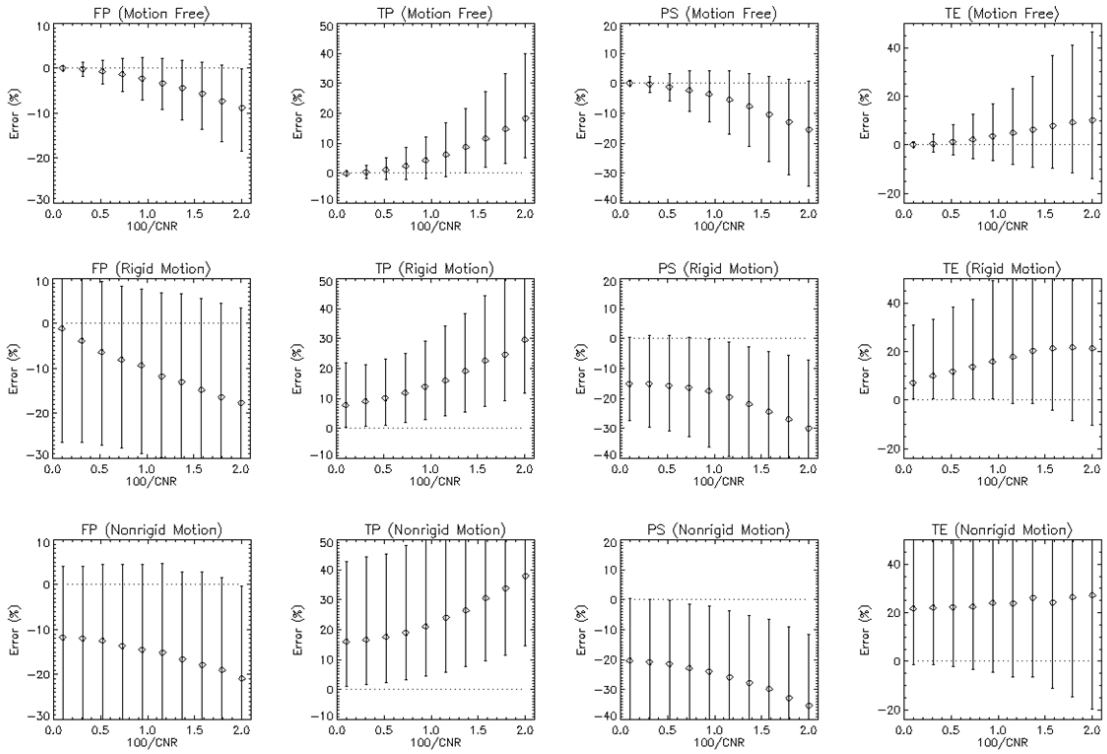

Figure 4.11: Error distribution before motion correction for the simulated data at CNR from 50 (very low) to 1000 (very high). The columns show the 4 parameters and the rows show different motion types: no motion (top row), rigid motion (middle row), non-rigid motion (bottom row). The circles indicate the median relative parameter error for all the pixels in the image, and the error bars represent the 75% range.

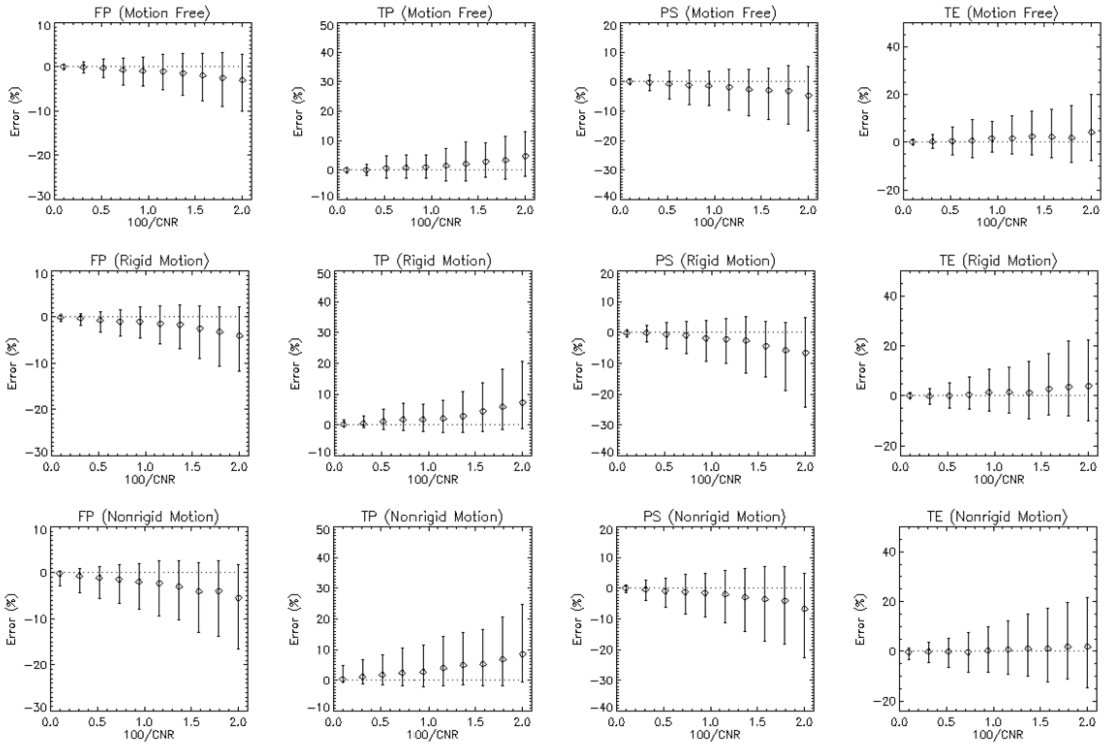

Figure 4.12: Error distribution with motion correction for the simulated data at CNR from 50 (very low) to 1000 (very high). The figure is organized in exactly the same way as Figure 4.11 to allow a direct evaluation of the effect of motion correction (compare corresponding panels in Figures 4.11 and 4.12).

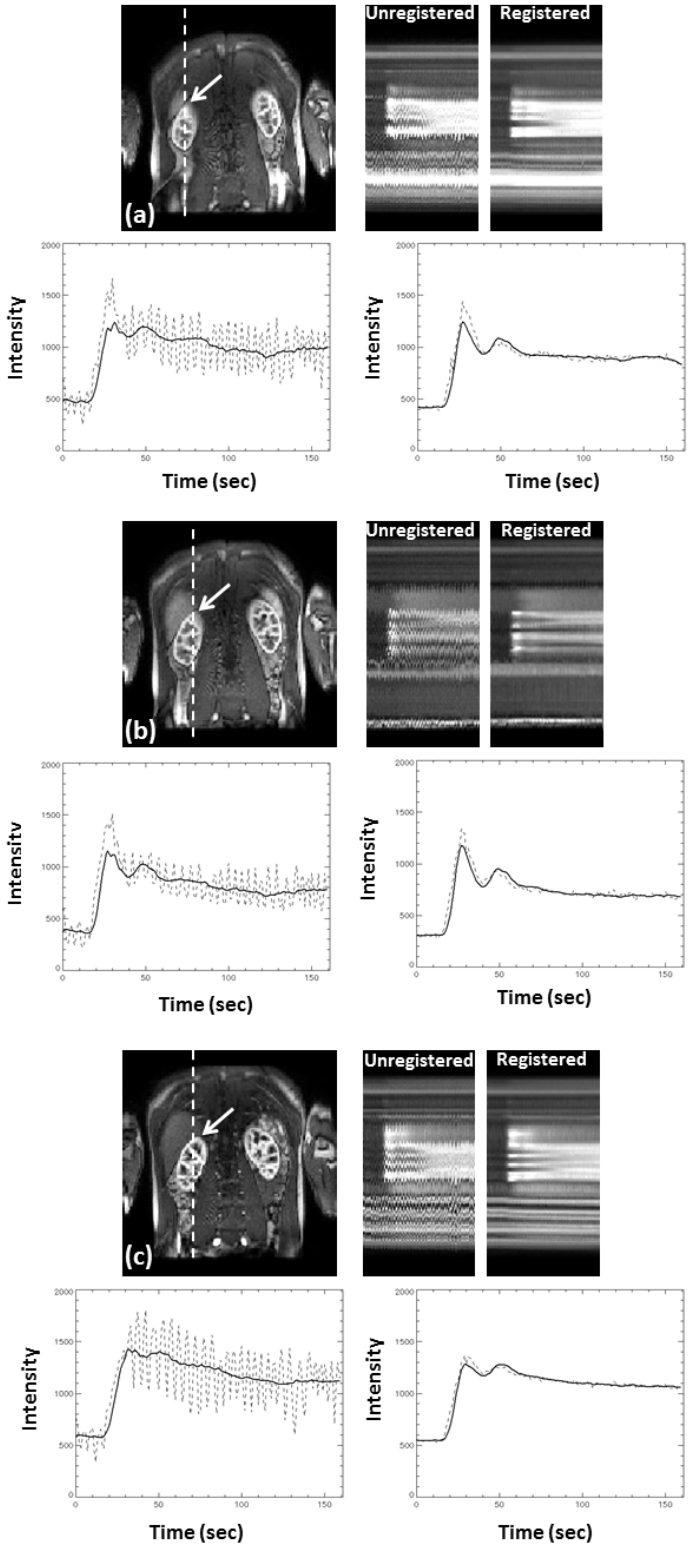

Figure 4.13: Effect of registration in Subject 1 renal DCE-MRI time series, (a)-(c) coronal view for anatomical reference, a dashed line indicates the location of the time-cuts for unregistered and registered data. Arrows indicate the location of the ROI. Time-intensity curves of the signal (dashed line) and the model fit (full line) for unregistered (left) and registered (right) data.

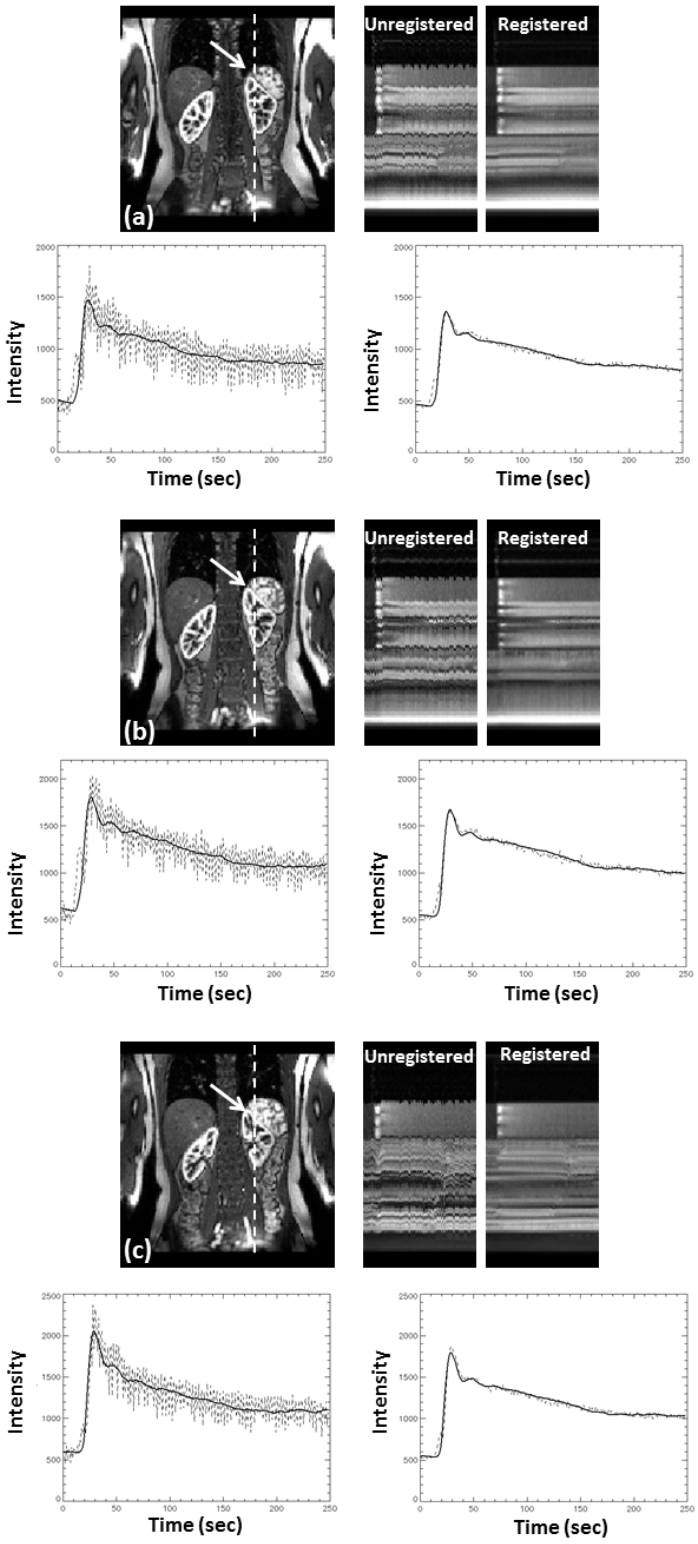

Figure 4.14: Effect of registration in Subject 2 renal DCE-MRI time series, (a)-(c) coronal view for anatomical reference, a dashed line indicates the location of the time-cuts for unregistered and registered data. Arrows indicate the location of the ROI. Time-intensity curves of the signal (dashed line) and the model fit (full line) for unregistered (left) and registered (right) data.

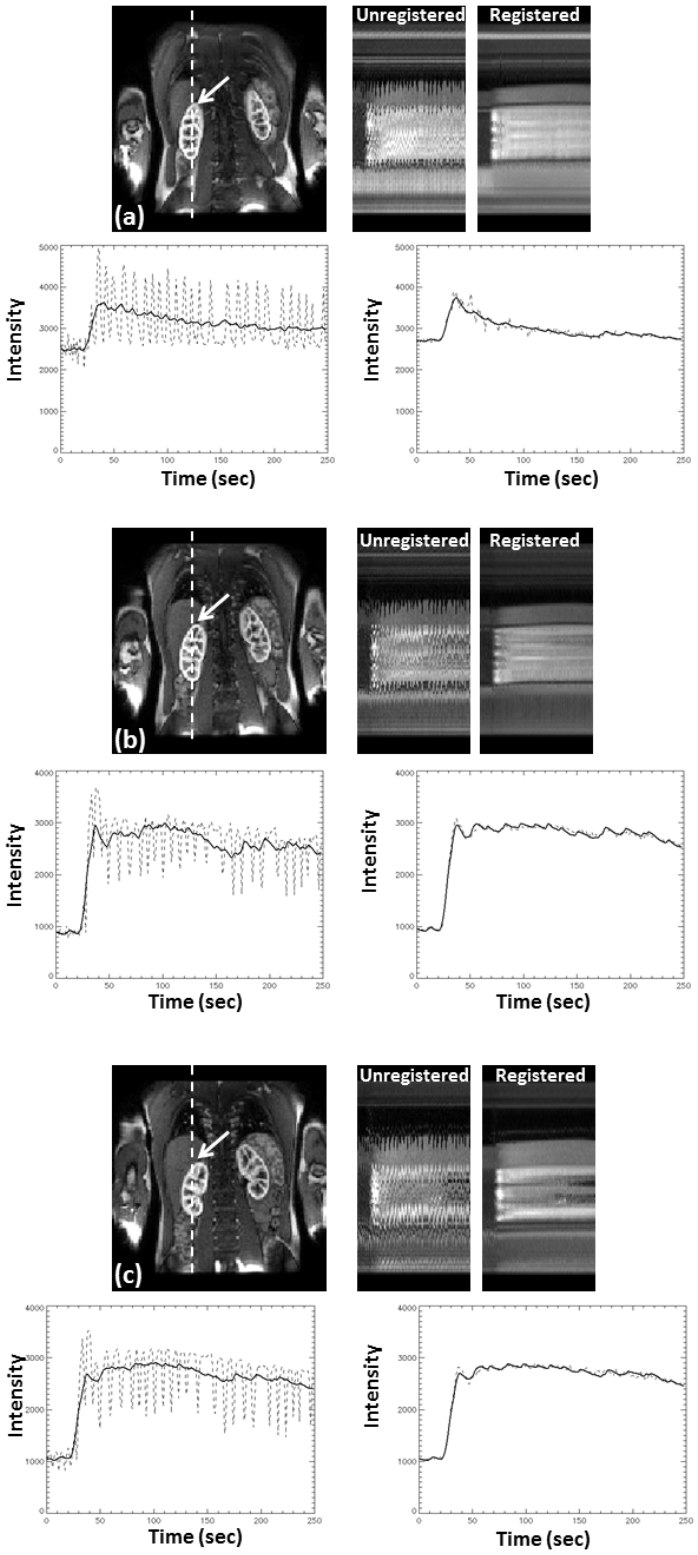

Figure 4.15: Effect of registration in Subject 3 renal DCE-MRI time series, (a)-(c) coronal view for anatomical reference, a dashed line indicates the location of the time-cuts for unregistered and registered data. Arrows indicate the location of the ROI. Time-intensity curves of the signal (dashed line) and the model fit (full line) for unregistered (left) and registered (right) data.

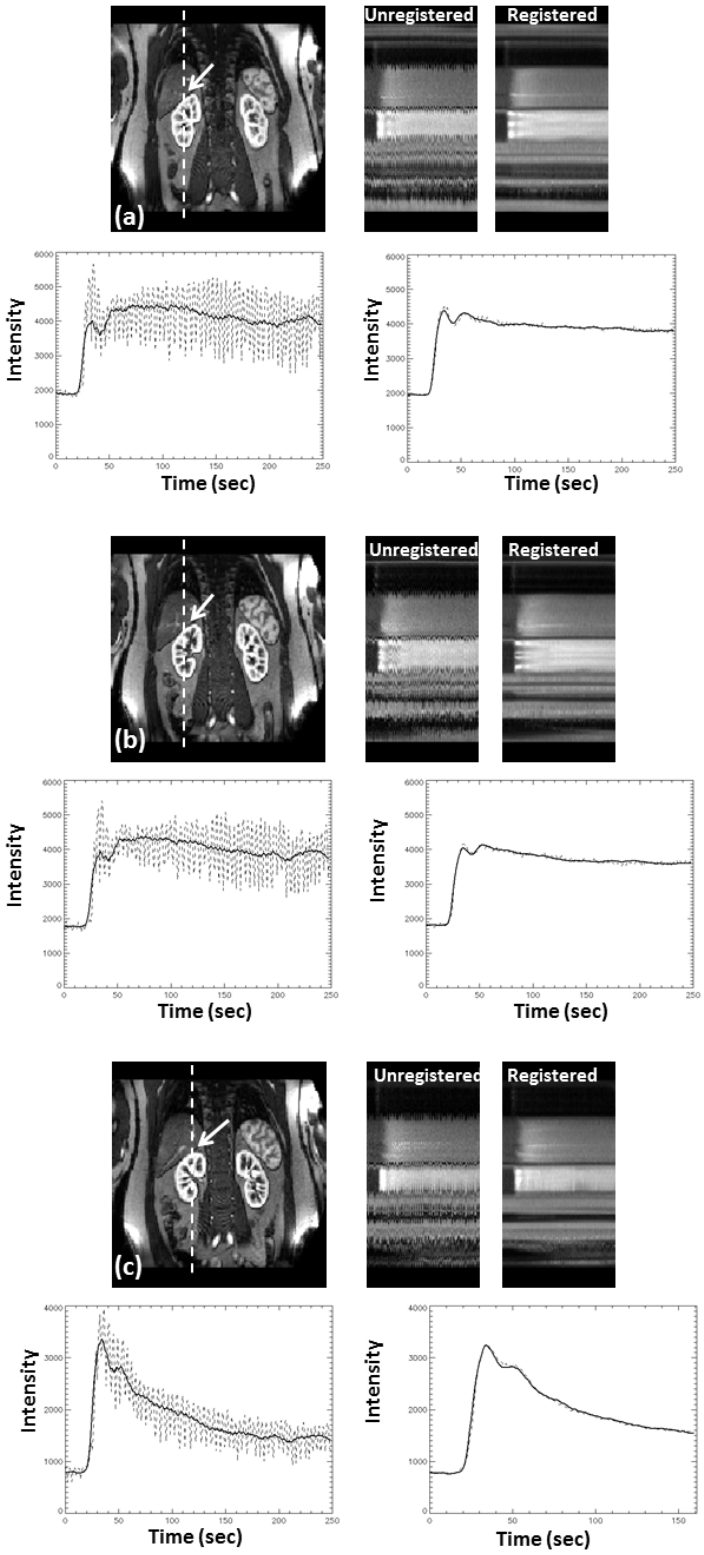

Figure 4.16: Effect of registration in Subject 4 renal DCE-MRI time series, (a)-(c) coronal view for anatomical reference, a dashed line indicates the location of the time-cuts for unregistered and registered data. Arrows indicate the location of the ROI. Time-intensity curves of the signal (dashed line) and the model fit (full line) for unregistered (left) and registered (right) data.

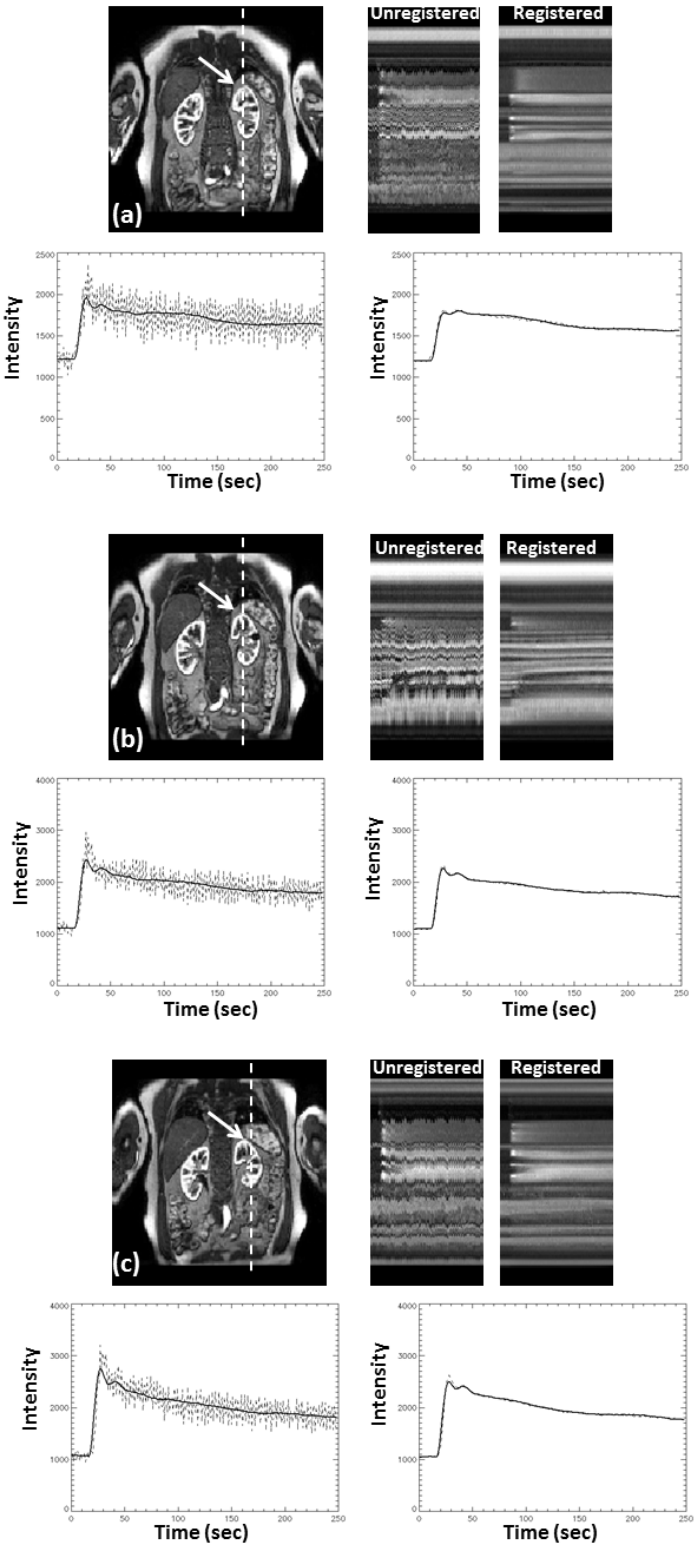

Figure 4.17: Effect of registration in Subject 5 renal DCE-MRI time series, (a)-(c) coronal view for anatomical reference, a dashed line indicates the location of the time-cuts for unregistered and registered data. Arrows indicate the location of the ROI. Time-intensity curves of the signal (dashed line) and the model fit (full line) for unregistered (left) and registered (right) data.

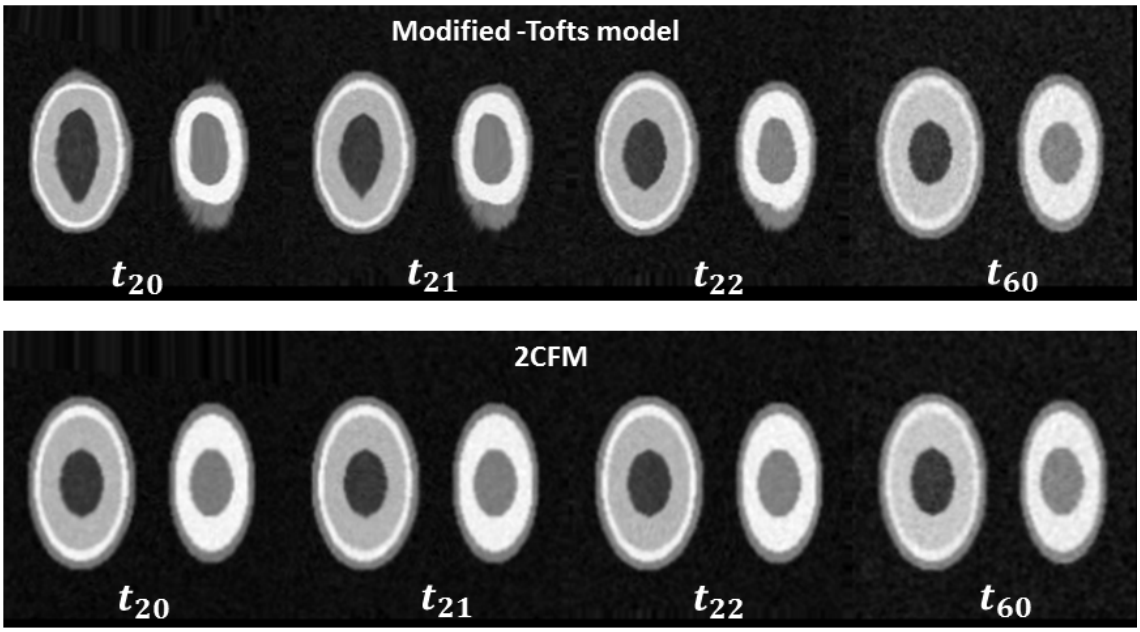

Figure 4.18: Illustration of the effect of motion correction at different time-points using the modified-Tofts model (top row) and the 2CFM (bottom row) for simulated data.

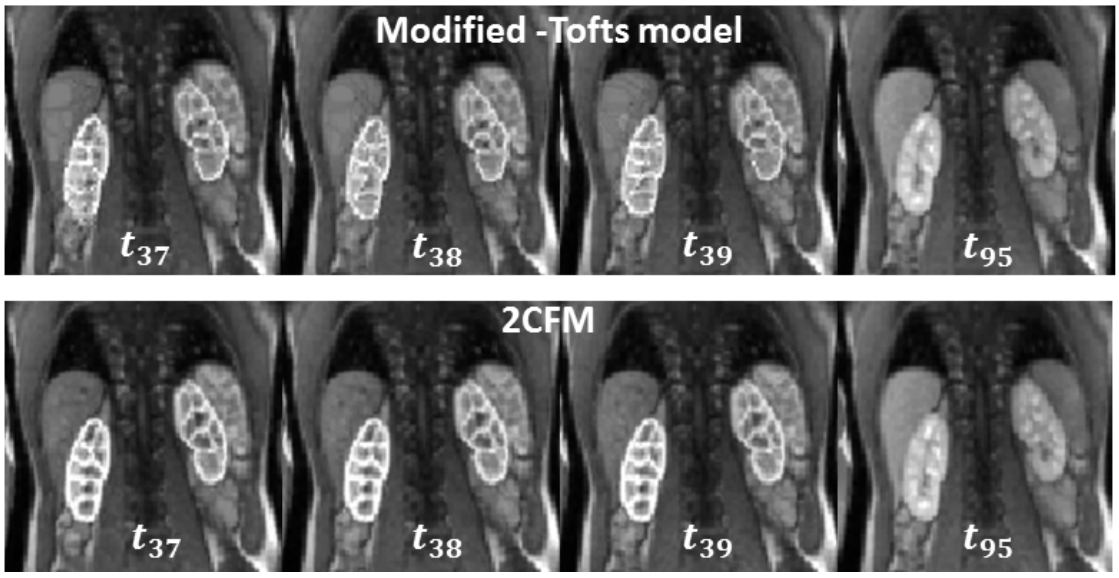

Figure 4.19: Illustration of the effect of motion correction at different time-points using the modified-Tofts model (top row) and the 2CFM (bottom row) for Subject 3 data. Motion correction was performed on the original image size. Images cropped from 136×136 to 76×76 for visibility.

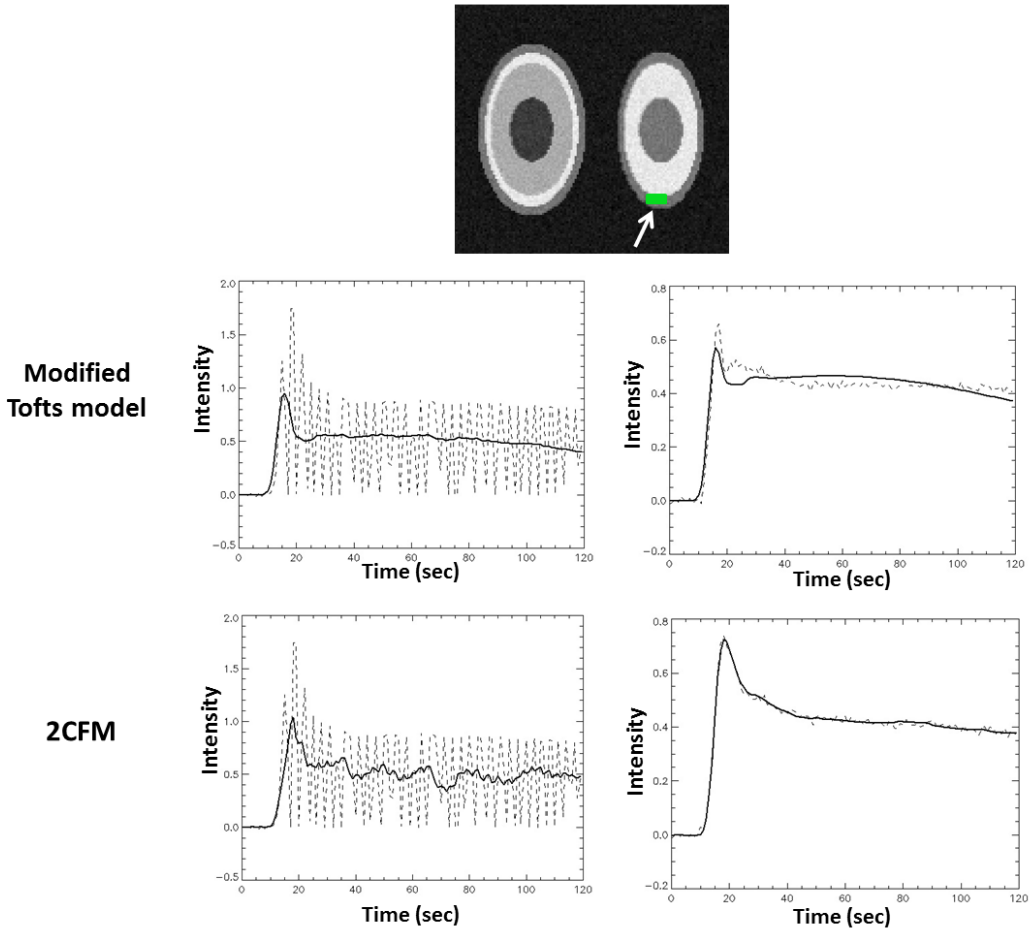

Figure 4.20: time-intensity curves of the signal (dashed line) and the model fit (full line) for the tissue ROI marked with green for simulated data. **Top row:** Unregistered data (left) and registered data (right) fitted with the modified-Tofts model. **Bottom row:** Unregistered data (left) and registered data (right) fitted with the 2CFM.

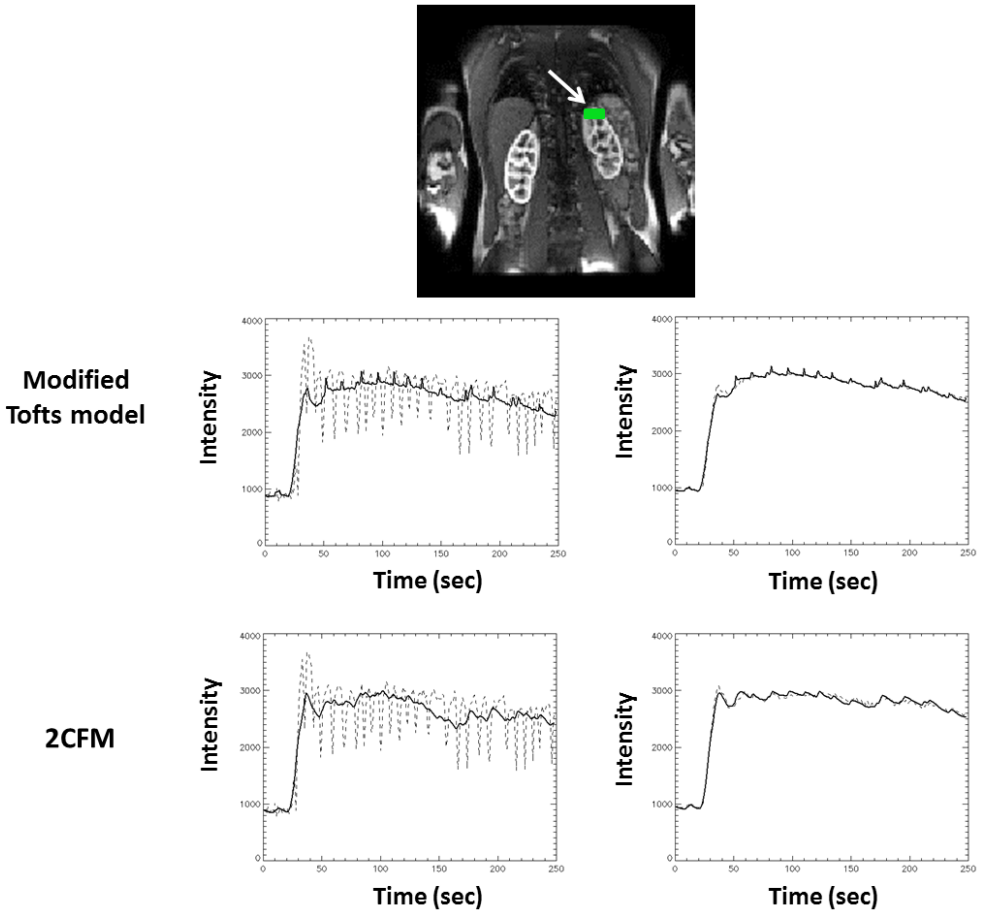

Figure 4.21: time-intensity curves of the signal (dashed line) and the model fit (full line) for the tissue ROI marked with green for Subject 3 data. **Top row:** Unregistered data (left) and registered data (right) fitted with the modified-Tofts model. **Bottom row:** Unregistered data (left) and registered data (right) fitted with the 2CFM.

4.5 Discussion

In this chapter, we have developed a fully automated tracer-kinetic model-driven registration method to remove the motion in DCE-MRI time-series. The method relies on registration of the source motion-corrupted images with reference to synthetic target images resulting from tracer-kinetic model fits. This method allows time-point by time-point registration and gives more control on the computation of the deformation field opposed to existing pairwise registration methods that choose a single target image.

In order to evaluate aspects of the proposed algorithm, we varied the settings of the default implementation. The effect of settings on registration algorithm are demonstrated experimentally using simulated and clinical data. The experiments indicate that the results were as expected in all cases: the relative error decreases with increasing iterations, the finer the resolution level used the smaller the error and the smaller the precision value the smaller the error. In addition to this, the results confirmed our expectations in terms of computational cost of the registration algorithm when we varied the convergence precision value and the resolution level. Smaller convergence precision and finer resolution led to an increase in computational cost.

As previously mentioned, the proposed registration method incorporates the use of a tracer-kinetic model to account for the signal intensity changes due to passage of the contrast agent. To the best of our knowledge, existing model-based registration methods used the modified-Tofts model. However, this model is unsuitable for renal DCE-MRI data where the 2CFM is the model of preference. For this reason, we have also evaluated the performance of the model-based registration method using the two different tracer-kinetic models. Qualitative registration results when using the two models are presented in Figures 4.18 and 4.19. Registration when using the modified-Tofts model tends to incorrectly deform enhancing features during the wash in phase in both simulated and clinical data. This might be explained by the rapid temporal changes in the beginning where the modified-Tofts model does not allow to model. The results suggest that the proposed algorithm when using the 2CFM gives superior registration as it showed a greater robustness to contrast changes. The general improvement of the two model fits after registration can be seen in Figures 4.20 and 4.21 where one can notice that the modified-Tofts model does not fit the data very well in the vascular phase.

Quantitative assessment of the accuracy of the registration algorithm is also presented in Figure 4.12. The validation using simulated data with ground truth at a wide range of noise levels and two types of motion (rigid and non-rigid) demonstrates good quality registration. The algorithm reduces the motion induced parameter error, improving the accuracy and precision of the parameters at all noise levels (Figure 4.12). One should note that the motion correction algorithm decreases the parameter error in motion-free data (Top rows of Figures 4.11 and 4.12). This can be explained by the fact that the proposed algorithm has a smoothing effect that leads to noise reduction and therefore improves the parameter accuracy and precision.

In addition, the proposed registration algorithm was applied to 5 renal DCE-MRI datasets. Evaluation of image registration on clinical data is usually a hard task because no ground truth is available. To assess the impact and performance of non-rigid registration we compared the results before and after motion correction. The results indicate that the motion correction method preserves good consistency in the presence of intensity and contrast variations (see Figure 4.10). Inspecting Figures 4.13−4.17, the registration method corrected in all cases the time-intensity curves compared to corresponding intensity curves before motion correction and also compared to known shapes from literature [87]. Time-cut images showed that our data have more motion compared to [87] and therefore, the motion correction was more challenging. After motion correction time-cut images were almost perfectly corrected where in some cases the time-cut images in [87] showed some residuals due to uncorrected motion. One should note that, in one case the proposed algorithm does not produce very accurate motion correction in few time-points during the wash in phase. This can be seen from time-cut images in Figure 4.15(a) where there are some residuals of uncorrected motion at the early time points. This might be explained by the long delay of the arrival of contrast agent between the artery and the kidney. As mentioned in Chapter 3, it is a limitation of the method that a delay parameter was not included in the 2CFM. The performance of the tracer-kinetic model-driven registration method is difficult to compare to that of Hamy et al. [87] since different kind of data have been used. An explicit comparison with the said method on same data would be of interest but has not been explored in this study. Interestingly, even though a renal cortical model is used (2CFM), the registration algorithm appears to work equally well in liver, spleen and renal medulla, Figure 4.6. The algorithm is also proved robust with respect to default optimisation parameter selection.

The work presented in this chapter also addressed the problem of high computational cost. The inclusion of the precomputation steps described in Section 4.3.2 allowed for a major improvement in the total computational time. In fact, most of the processing time is spent in the gradient computation step, and the precomputation of the gradients can accelerate the convergence of the optimisation algorithm. The precomputation of B-spline coefficients accelerated the FFD registration step since the coefficients only changed when the resolution of the deformation field changed. Using the default implementation precomputation steps reduced the computational times in clinical data (matrix 135×135, 249 dynamics) from 5 hours to less than 20 min and in simulated data (matrix 128×128, 120 dynamics) from 14 min to 3 min.

As mentioned earlier in Section 4.3.1, the linearised 2CFM (Eq.(4.1)) fitted time-point by time-point to C_{corr} (Eq.(4.4)) to determine estimates for $\alpha(\mathbf{x}), \beta(\mathbf{x}), \gamma(\mathbf{x})$ and $F_p(\mathbf{x})$. In order to create I_{target}, first the C_{fit} is calculated using Eq.(4.6). At this point, it is essential to note that the integrals involved in Eq.(4.6) connect all the time-points. Thus, C_{fit} at a given time-point involves C_{corr} at a particular time-point plus all the earlier time points. Consequently, the assumption we made that $\mathbf{d_t}$ can be updated using time-point by time-point co-registration is not truly valid. This is because the cost function, $\mathcal{C}$, in Eq.(4.8) depends on C_{corr} and therefore, $\mathbf{d_t}$ at a particular time-point plus also all earlier time-points. On the other hand this issue does not appear when a NLLS fit is applied since the model fit in Eq.(3.14) involves only the kinetic parameters of the model. However, as pointed previously the standard NLLS method requires considerable computation time and it is therefore, impractical for use in the registration process since requires the application of the 2CFM on a pixel-by-pixel basis. In order to take advantage of fast linearised model, similar to [53, 88, 89] we have used a heuristic approach where we treated Eq.(4.6) as if it is a single time point.

4.6 Conclusion

In summary, we have developed a novel fully automated tracer-kinetic model-based registration method in DCE-MRI time-series. It has been applied to multiple renal DCE-MRI datasets affected by free breathing motion. The proposed algorithm effectively removed between-frame breathing motion. We have also explored the validation of this method using simulated data. The simulation results have provided

evidence for successful motion correction with improved accuracy and precision of the parameters. By using the precomputation steps we avoided redundant calculations and we reduced execution times by a factor of 15.

Chapter 5

Application of Tracer-Kinetic Model-Driven Registration to Renal DCE-MRI Data

The tracer-kinetic model driven motion correction algorithm developed in Chapter 4 is now extended to 3D DCE-MRI data. The algorithm is applied to renal DCE-MRI datasets acquired under free breathing. The translation to 3D has brought additional challenges due to exponential increase in computational complexity and ghosting artefacts caused by within-frame breathing motion. The performance of the motion correction is analysed by visual assessment and by concentration-time curves. The work in this chapter is also aimed to investigate the potential benefit of adding motion correction to the analysis of DCE-MRI in the context of clinical routine.

5.1 Introduction

Atherosclerotic renovascular disease (ARVD) is a progressive condition that affects the renal function because of the inadequate blood supply and downstream damage caused by cytokines and hypertension [62, 90]. ARVD is the most common disease of the renal arteries and is a cause of both chronic kidney disease (CKD) and end stage renal failure (ESRF) [91]. ARVD accounts for 90% of renal artery stenosis (RAS)

in the Western population and is very commonly seen in the aging population [92]. Management of ARVD can be done either by blood pressure control with medical treatment or by renal revascularization with angioplasty and stenting in order to prevent further renal impairment [93].

As mentioned in Chapter 1, GFR is considered to be the most useful index of kidney function. Measurements of the GFR are important for the assessment of renal diseases and their treatment [94]. GFR is traditionally measured by renal scintigraphy using radiolabeled tracers such as Tc^{99}-diethylenetriamine pentaacetic acid (^{99}Tc-DTPA) or ^{99}Tc-dimercaptosuccinic acid (^{99}Tc-DMSA) [95]. However, these type of methods involve ionising radiation exposure and require licensed nuclear medicine facilities. A potential alternative to radioisotope measurement techniques is DCE-MRI which enables measurements of single-kidney glomerular filtration rate (SK-GFR) as well as tissue perfusion and vascularity [96, 97, 98].

Several studies of measuring the kidney function using DCE-MRI have been described in the literature. Early work by Hackstein et al. [95] demonstrated a good correlation (Pearson's correlation coefficient R = 0.86) between MRI derived SK-GFR and the SK-GFR measured by iopromide. In this study the authors employed a Rutland-Patlak plot to estimate kidney function in 28 patients. A subsequent study performed in rabbits by Annet et al. [47] suggested that better results could be obtained using a cortical-compartment model which can be thought of as equivalent to 2CFM. A substantial correlation (R = 0.821) was observed between the GFR measured with MR and the gold standard radioisotope technique. Buckley et al. [99] used both Rutland-Patlak plot and modified Tofts model to estimate GFR in individual kidneys in 36 patients with ARVD using DCE-MRI. To further test whether DCE-MRI has the potential to be a one-stop diagnostic and prognostic tool, the authors assessed the SK-GFR derived from DCE-MRI using a radioisotope measurement as reference measures. The results from this study suggested that estimates of SK-GFR using both techniques correlated well with radioisotope-assessed SK-GFR (Rutland-Patlak: Spearman's $\rho = 0.81$ and compartmental model: $\rho = 0.71$). Lee et al. [100] used a three-compartment, six-parameter model for MR renography analysis. The authors compared the SK-GFR measurements from MR renography with the reference measurements from ^{99}Tc-DTPA clearance and scintigraphy. The results showed that SK-GFR from MR renography agreed well with the reference measurements (r= 0.84). Bland-Altman analysis showed an average difference of 11.9 ml/min between the two methods. Another work to assess the

GFR measurement with MR renography has been done by Vivier et al. [101] in 20 patients with liver cirrhosis. All patients here underwent routine MR imaging, with urinary clearance of ^{99}Tc-DTPA to obtain a reference GFR measurements. Comparisons to results produced by the reference standard technique yield accurate and precise measurements of GFR with MR renography ($R^2 = 0.87$). In work by Lim et al [62] a good correlation was also found between SK-GFR values from DCE-MRI and radioisotopes with correlation coefficient R = 0.91. Bland-Altman analysis showed an average difference of 1.5 mL/min between the two methods. It has been also pointed out that the correlation can improve further by adding motion correction to the analysis. Further work on measurement of SK-GFR using DCE-MRI was made by Bokacheva et al. [102]. The authors compared different methods for calculating the SK-GFR from T1-weighted MR renography against reference radionuclide measurements. Correlations with reference GFRs ranged from R = 0.74 to R = 0.85. In a recent study Eikefjord et al. [103] investigated the accuracy and precision of MRI derived SK-GFR using the 2CFM compared to iohexol-GFR. Twenty healthy volunteers were undertaken two DCE-MRI examinations. With reference to iohexol-GFR Pearson correlations and also the test-retest measurements were $r = 0.57$ and $r = 0.29$. Compared to the other studies the correlations in [103] were substantially weaker. However, their results were in good agreement with Hackstein et al. [104] examining healthy participants, reporting Pearson correlation $r = 0.36$. An overview of the results obtained from previous studies stated above are summarised in Table 5.1.

The aims of this study were to extend the previously developed tracer-kinetic model driven motion correction algorithm to 3D data and to test whether DCE-MRI measurement of SK-GFR was improved by adding motion correction to the analysis. For the latter, we wish to investigate the accuracy and precision of motion corrected DCE-MRI measurement of SK-GFR compared to SK-GFR derived from DCE-MRI without motion correction. Radioisotope measurements of SK-GFR were used as gold standards.

	Correlation	**Slope**	**Intercept**	**Mean Difference** MR - Reference
Hackstein et al. (n = 28)	0.86	0.70	24.2	-
Annet et al. (n = 10)	0.82	-	-	0.4 mL/min/kg
Buckley et al. (n = 38)	0.82 (Comp. model) 0.90 (R-P plot)	2.21 1.52	30.07 -3.80	- -
Lee et al. (n = 10)	0.84	0.76	-1.14	11.9 mL/min
Bokacheva et al. (n = 10)	0.74−0.85	0.32−0.92	-1.14−7.36	-
Vivier et al. (n = 20)	0.87	-	-	-7.7− -4.1 mL/min/1.73m^2
Lim et al. (n = 15)	0.91	0.96	0.15	1.5 mL/min
Eikefjord et al. (n = 20)	0.57 (Test) 0.29 (Re-test)	1.51 0.47	-50.78 61.10	1.5 mL/min/1.73m^2 6.1 mL/min/1.73m^2

Table 5.1: Table summarises the results obtained from previous studies where n defines the number of patients examined in each study.

5.2 Tracer-Kinetic Model Driven Registration Modifications

The application of tracer-kinetic model driven registration algorithm to 3D dynamic renal images is slightly different from the initial application to 2D DCE-MRI data presented in Chapter 4. Thus, an adjustment is required. In particular, as the difference lies in the image data geometries, the transformation function must be changed. This can be done by generalising the deformation field of the already existing 2D algorithm, given in Eq.(4.21). Using the notation introduced in the previous chapter, for a given control point the displacement of a voxel $\mathbf{x} = (x, y, z)$ in 3D is defined as:

$$\mathbf{d}_{\text{linear}}(\mathbf{x}) = \sum_{l=0}^{1}\sum_{m=0}^{1}\sum_{n=0}^{1} B_l(x - x_i)B_m(y - y_j)B_n(z - z_k)\,\mathbf{d}_{i+l,j+m,k+n}, \tag{5.1}$$

where (i, j, k) is the index of control point cell containing $\mathbf{x}$ and B is a weighting function based on linear B-splines determining the contribution of the control point displacement $\mathbf{d}_{i,j,k}$ of an image voxel $\mathbf{x}$.

Another difference between the two applications lies in the interpolation method. The obvious extension of bilinear interpolation to 3D is the so called trilinear interpolation. For an arbitrary point (x, y, z) the motion corrected image, I_{corr}, can be obtained from:

$$\begin{aligned} I_{\text{corr}}(x,y,z) = {} & I_{\text{source}}(x_i,y_i,z_i) + (x-x_i)\frac{\Delta I_{\text{source}}}{\Delta x}(x_i,y_i,z_i) + (y-y_i)\frac{\Delta I_{\text{source}}}{\Delta y}(x_i,y_i,z_i) \\ & + (z-z_i)\frac{\Delta I_{\text{source}}}{\Delta z}(x_i,y_i,z_i) + (x-x_i)(y-y_i)\frac{\Delta^2 I_{\text{source}}}{\Delta x\Delta y}(x_i,y_i,z_i) \\ & + (x-x_i)(z-z_i)\frac{\Delta^2 I_{\text{source}}}{\Delta x\Delta z}(x_i,y_i,z_i) + (y-y_i)(z-z_i)\frac{\Delta^2 I_{\text{source}}}{\Delta y\Delta z}(x_i,y_i,z_i) \\ & + (x-x_i)(y-y_i)(z-z_i)\frac{\Delta^3 I_{\text{source}}}{\Delta x\Delta y\Delta z}(x_i,y_i,z_i). \end{aligned} \tag{5.2}$$

The numerical derivatives of the I_{source} have been calculated with finite difference

approximations. No further modifications of the motion correction algorithm or additional tuning was required for the application to 3D data.

5.3 Materials and Methods

5.3.1 Clinical Data

A local research ethics committee approved the retrospective use of anonymised patient data. For prospective data, all patients provided written informed consent as part of a protocol agreed by the local research ethics committee.

Participants were amassed from the Renal Department of Salford Royal Hospital. The 8 patients were collected between 2007 and January 2010 from a previously reported research study [62]. All patients who participated had ARVD with significant RAS and were treated by percutaneous transluminal renal angioplasty with stenting. The inclusion criterion was >60% RAS based on MR angiography and one or more of the following: advanced renal dysfunction, deteriorating renal function, or flash pulmonary edema. The patients received both DCE-MRI and radioisotope SK-GFR measurement at baseline and 4 months after the procedure. Inclusion criteria were based on reported results from previous study [62] comparing the difference between SK-GFR values derived from DCE-MRI and the gold standard radioisotope method. We selected 6 cases that showed large difference between the DCE-MRI estimated SK-GFR and the radioisotope measurement, 1 case showed moderate difference and 1 case showed not significant difference.

5.3.2 Radioisotope Measurement

Radioisotope SK-GFR (Iso SK-GFR) measurements were performed with standard nuclear medicine techniques [105, 96]. The global GFR was calculated using ^{51}Cr-ethylenediaminetetraacetic acid (^{51}Cr-EDTA) clearance and differential kidney isotope uptake was measured using ^{99}Tc-DMSA scintigraphy. The individual kidney function was then assessed by dividing the global GFR according to percentage ^{99}Tc-DMSA uptake.

5.3.3 DCE-MR Imaging

DCE-MRI measurements were performed using a 3T whole body scanner (Philips Achieva, Philips Medical Systems) with a phased-array body coil for signal reception. Subjects were imaged using 3D spoiled gradient echo sequence. The following parameters were used for the acquisition: repetition time = 5.0 ms, echo time = 0.9 ms, field of view = 400 × 400 × 100 mm, flip angle = 17°, parallel acquisition using a sensitivity encoding (SENSE) factor = 2, approximate acquisition matrix = 128 × 84 × 10, and reconstructed matrix after zero-filling = 128 × 128 × 20. This resulted in a temporal resolution of 2.1 s/volume. Subjects were given a quarter dose of 0.025 mmol/kg Gd-DOTA (Dotarem, Guerbet, France) at a rate of 3 ml/s. In all cases the acquisition and contrast agent injection were initiated simultaneously.

5.3.4 DCE-MRI Postprocessing

5.3.4.1 Without Motion Correction

Postprocessing was performed offline using PMI 0.4 software (Platform for Research in Medical Imaging) written in IDL 6.3 [11, 106]. Digital Imaging and Communications in Medicine (DICOM) images were imported into the software and the analysis was performed by one operator, who was blinded to the patient information and the treatment status of the kidney (stented or not).

Rectangular ROIs were firstly drawn on different coronal slices of dynamic series between the renal and iliac bifurcations of the aorta in order to avoid smaller arteries and to minimise inflow effects [107]. The bifurcations themselves were avoided as the blood flow there is turbulent. The highest 5% signal intensity of selected voxels was selected to generate a volume of distribution map. Doing this semi-automatically an AIF was extracted. Pixel-by-pixel deconvolution analysis was performed to generate maps of blood flow and volume of distribution [108]. A whole kidney parenchymal ROI was segmented semi-automatically by setting a threshold on the volume of distribution map by adjusting ceiling and floor contrast, where extrarenal pixels were manually excluded. Assuming a linear relationship between signal intensity and the constrast agent concentration, the concentration-time curves for each individual kidney and the aorta were estimated by subtracting the precontrast signal from the dynamic signal, i.e. $C(t) = S(t) - S_0$ where $S(t)$ is the signal at time t and S_0 is the

baseline signal. The concentration-time curves of the selected ROIs were then fitted non-linearly to the 2CFM [11]. A DCE-MRI measurement of SK-GFR was defined as the product of the selected kidney parenchymal ROI volume, E and F_p [11].

5.3.4.2 With Motion Correction

DICOM images were imported into the PMI 0.4 software and then exported in DAT files. The DAT files were imported in IDL 6.4 (Exelis VIS, Boulder, CO) and were then motion corrected using the tracer-kinetic model-driven registration algorithm as described in Section 5.2. The default algorithm parameters were used as stated previously in Section 4.4.3 with the only exception being the maximum resolution level which was set to 2^4. In the motion correction process a fixed AIF has been used which was extracted from the uncorrected data as described above. Motion corrected data including all time frames were then imported into the PMI 0.4 software and then analysed by one operator. At this point it should be noted that the operator of motion corrected data was different from the one who have performed the analysis on data before motion correction. The postprocessing is the same as described above for the uncorrected data. It is essential to mention that for the final parameter fitting a new AIF has been extracted from the motion corrected data in a similar fashion. The SK-GFR in motion corrected data have been measured in two different ways: (1) from DCE-MRI motion corrected data using a measured AIF as described above and (2) from DCE-MRI motion corrected data using the input function measured in data before motion correction, referred to as "Orig AIF". The reason for this will be further clarified later.

5.3.5 Statistical Analysis

To avoid any possible confusion, the gold-standard SK-GFR value derived from the radioisotope measurement is referred to as "Iso SK-GFR" and the SK-GFR value derived from DCE-MRI measurement as "SK-GFR". Linear regression analysis was performed to compare sixteen recorded SK-GFR values to gold-standard Iso SK-GFR values using Excel (Excel 2010, Microsoft). The correlations between recorded DCE-MRI SK-GFR and Iso SK-GFR were assessed using Spearman's rank correlation coefficient (ρ). To test whether motion correction reduces the systematic error., Wilcoxon Signed-Rank test was performed to compare the mean differences in recor-

ded SK-GFR values derived from DCE-MRI data to gold-standard Iso SK-GFR. For testing agreement between measurement of SK-GFR obtained with DCE-MRI and with radionuclide techniques, we also performed Bland-Altman analysis. Wilcoxon Signed-Rank test was also performed in R (version 3.3.1, 2016) and used to compare the differences in renal parameters for two groups: (1) before and after motion correction, and (2) before and after motion correction using Orig AIF. Numerical results are presented as mean $\pm$ standard deviation. Significance level was set at 5%.

5.4 Results

5.4.1 Evaluation of motion correction performance

Figures 5.1 - 5.6 show the effect of motion correction on the measured images in 6 out of 8 patient data, respectively. Accurate motion correction results have been achieved as demonstrated through the different time frames in all cases. One can notice that despite the significant within-frame artefacts, the between-frame motion is effectively removed without affecting the signal intensities or image contrast as demonstrated through the different time frames.

Figures 5.7 - 5.12 show the effect of motion correction on temporal profiles from representative kidney ROIs of 6 out of 8 patient data, respectively. Original time-intensity curves of kidney ROI showed large respiratory signal changes which are are notably reduced after motion correction, resulting in an improved fit to the data in all cases. The figures also show the effect of motion correction in AIF. Original AIF has higher signal intensity than AIF obtained after motion correction. Finally these figures show the effect of motion correction on the F_p parametric maps. The F_p maps before motion correction show strong blurring and artefacts, which are mostly removed after motion correction leading to much clearer organ boundaries and internal structures such as cortex and medulla.

Figures 5.13 and 5.14 show the effect of motion correction in clinical data in both superior-inferior direction and anterior-posterior direction, respectively. Time-cut images of the unregistered and registered data demonstrate that misalignments were reduced after registration in all cases.

Regarding the calculation times, in the original implementation the registration algorithm did not converge within 5 days. However, the precomputation steps described previously in Section 4.3.2 reduced calculation times to 12-13 hrs, where only one case took about 26 hrs.

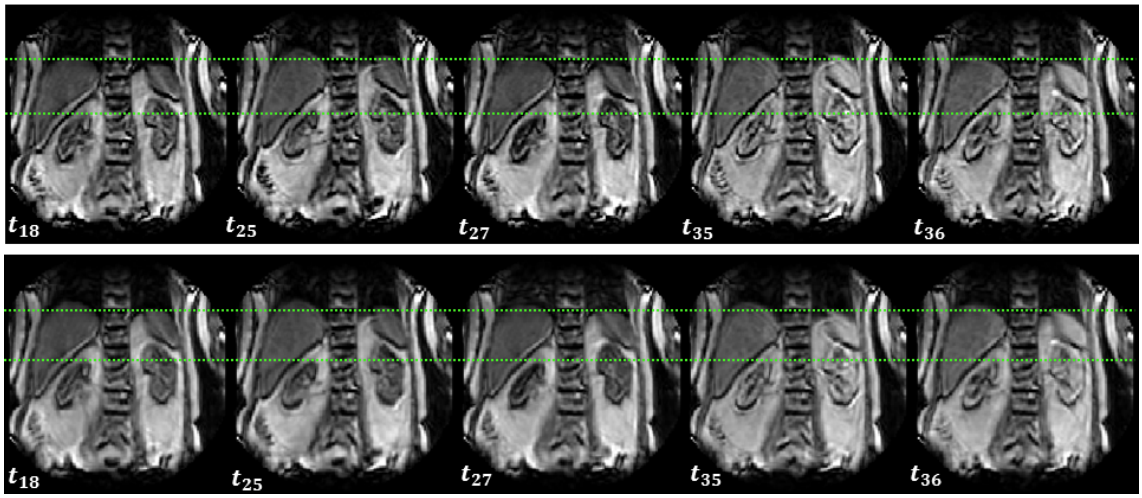

Figure 5.1: Illustration of the effect of motion correction at different time points in Patient 1 data. From top to bottom: Original time-series with frame indices; corresponding time-series after motion correction.

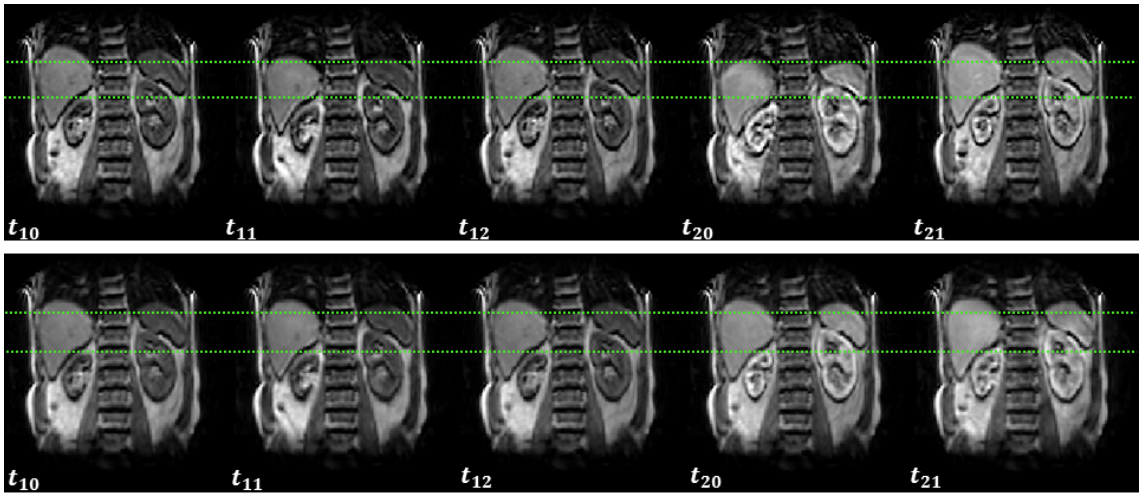

Figure 5.2: Illustration of the effect of motion correction at different time points in Patient 2 data. From top to bottom: Original time-series with frame indices; corresponding time-series after motion correction.

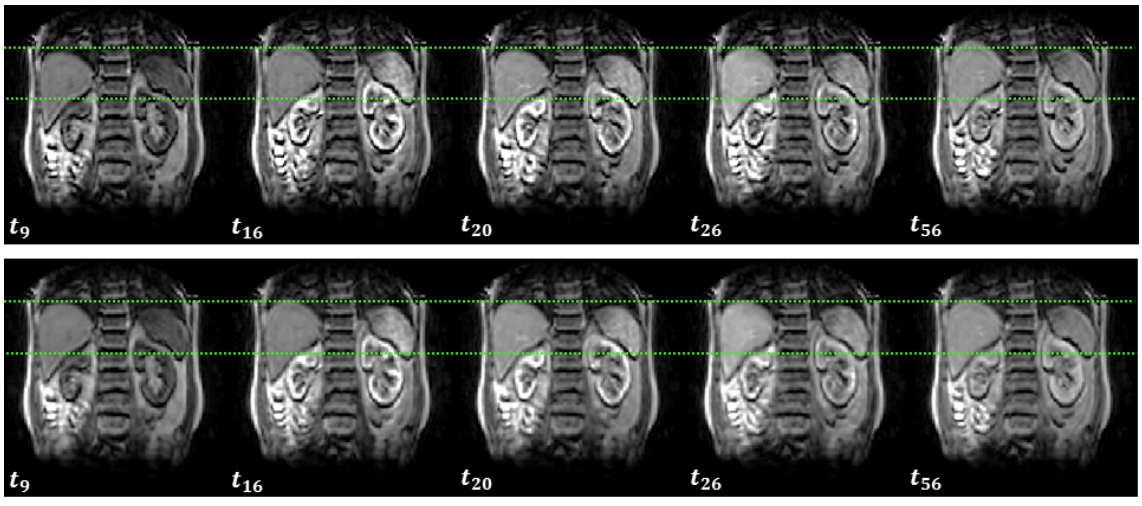

Figure 5.3: Illustration of the effect of motion correction at different time points in Patient 3 data. From top to bottom: Original time-series with frame indices; corresponding time-series after motion correction.

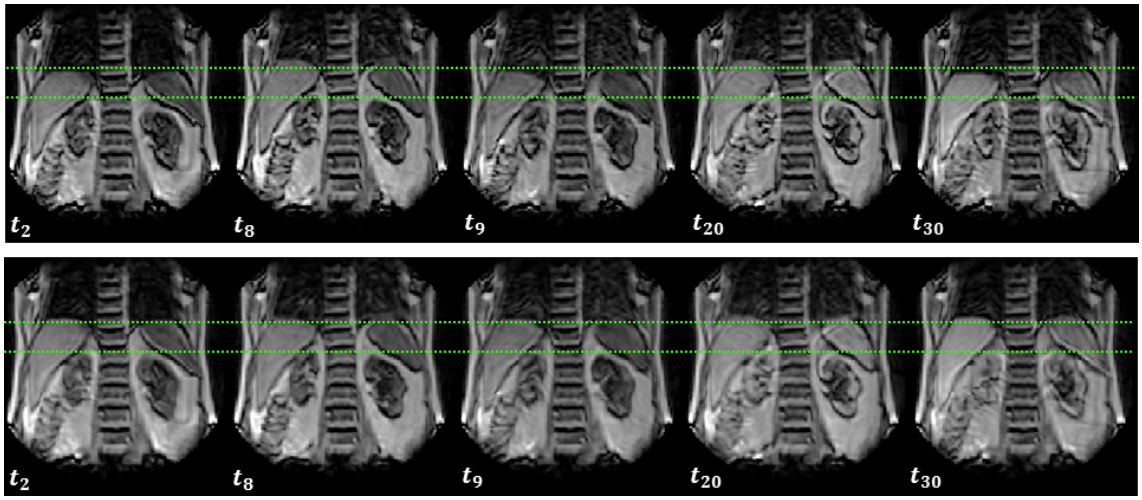

Figure 5.4: Illustration of the effect of motion correction at different time points in Patient 4 data. From top to bottom: Original time-series with frame indices; corresponding time-series after motion correction.

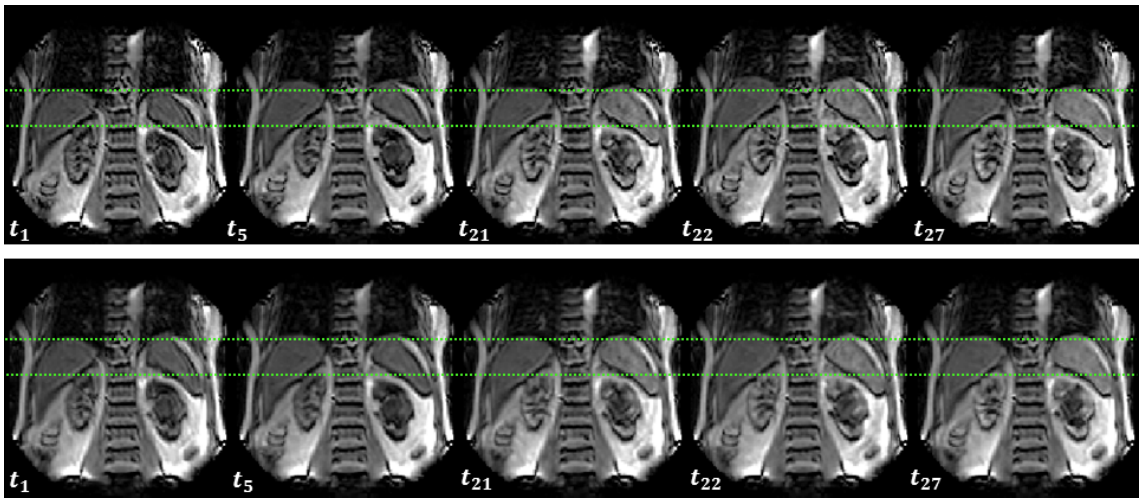

Figure 5.5: Illustration of the effect of motion correction at different time points in Patient 5 data. From top to bottom: Original time-series with frame indices; corresponding time-series after motion correction.

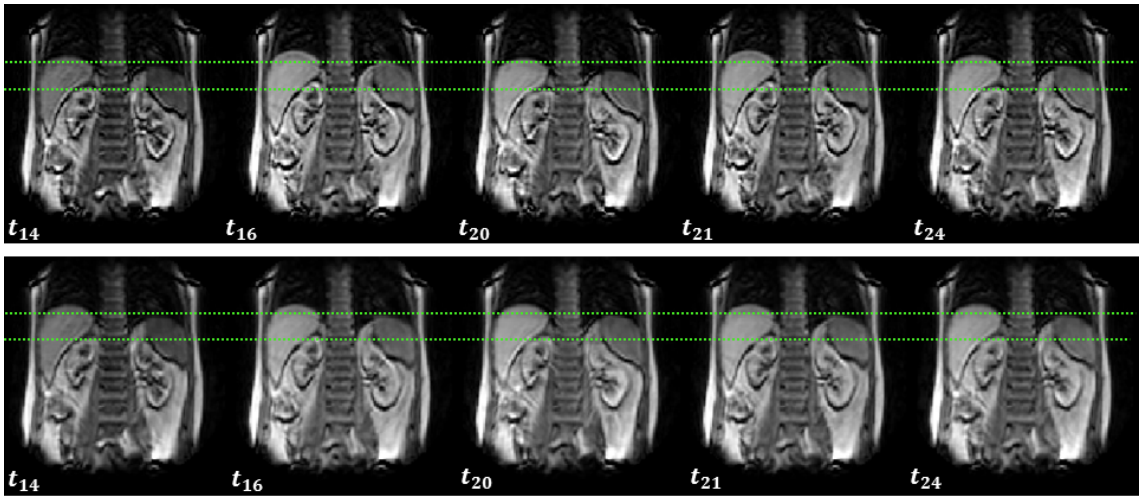

Figure 5.6: Illustration of the effect of motion correction at different time points in Patient 6 data. From top to bottom: Original time-series with frame indices; corresponding time-series after motion correction.

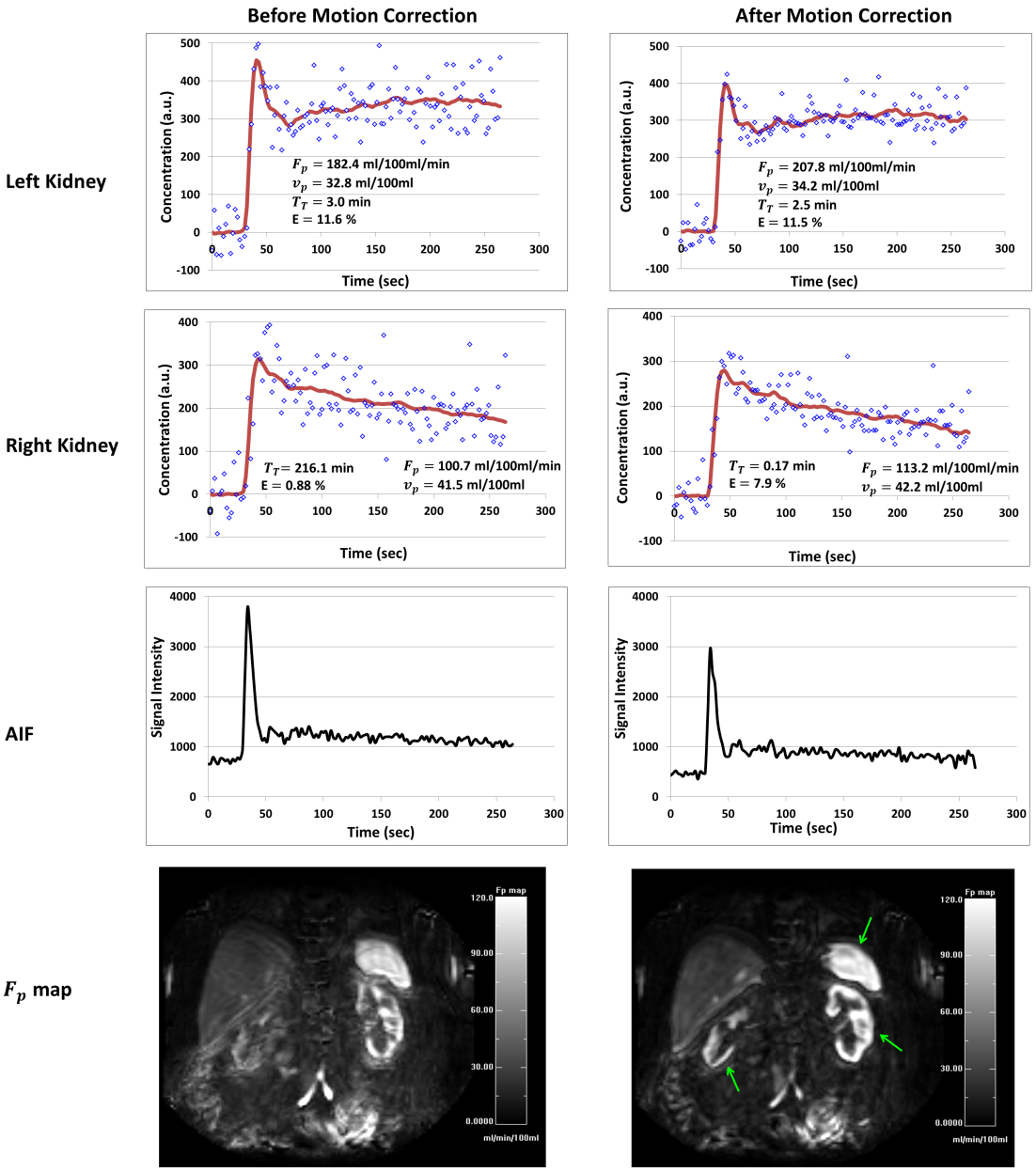

Figure 5.7: Effects of motion correction in Patient 1 data. The first two rows show the plots of the concentration-time curves (blue dots) and the two-compartment filtration model fit (red line) before and after motion correction for each kidney ROI. The third row shows the signal intensity curves of the AIF before and after motion correction. Bottom row shows the plasma flow (F_p) maps before and after motion correction.

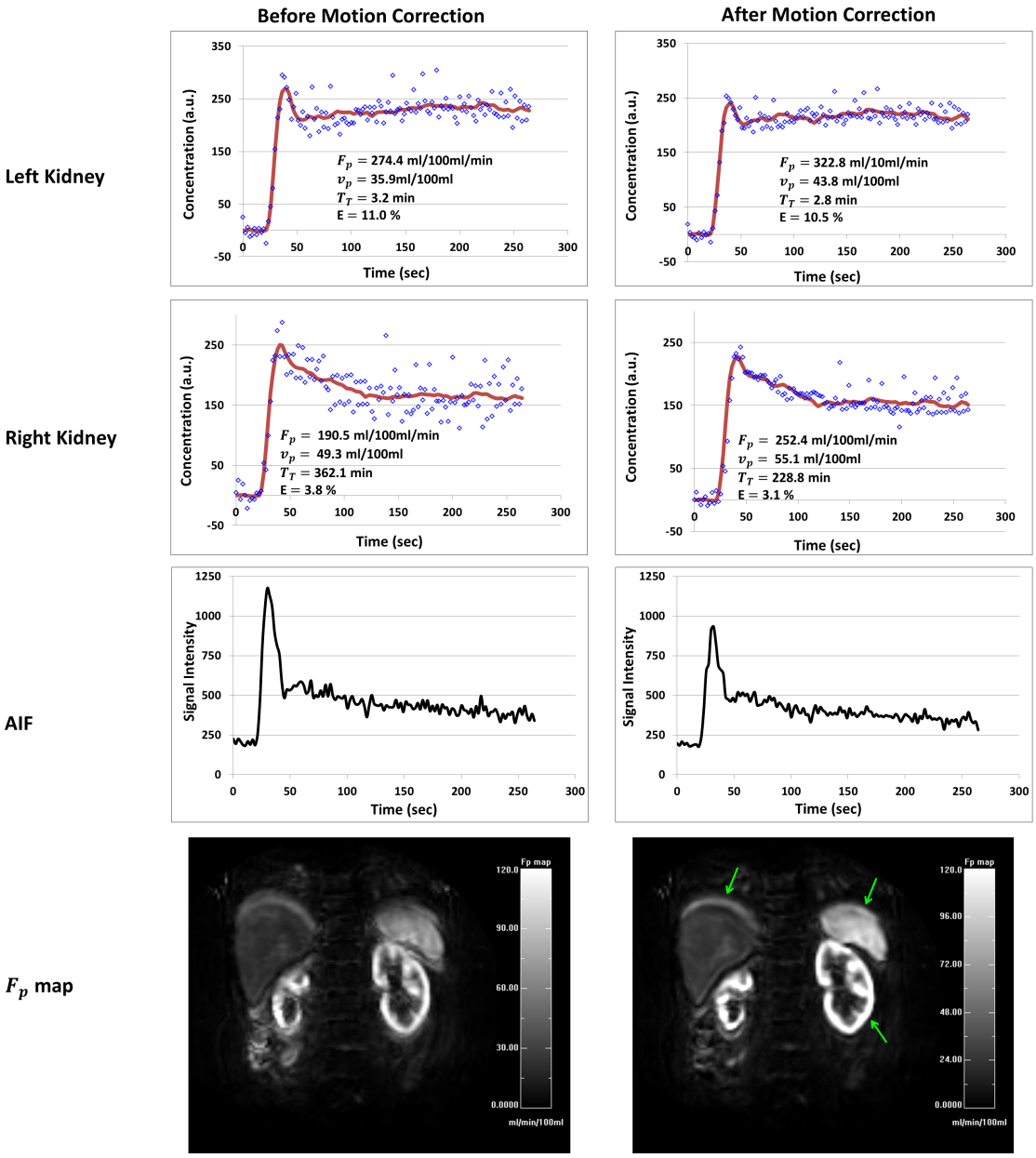

Figure 5.8: Effects of motion correction in Patient 2 data. The first two rows show the plots of the concentration-time curves (blue dots) and the two-compartment filtration model fit (red line) before and after motion correction for each kidney ROI. The third row shows the signal intensity curves of the AIF before and after motion correction. Bottom row shows the plasma flow (F_p) maps before and after motion correction.

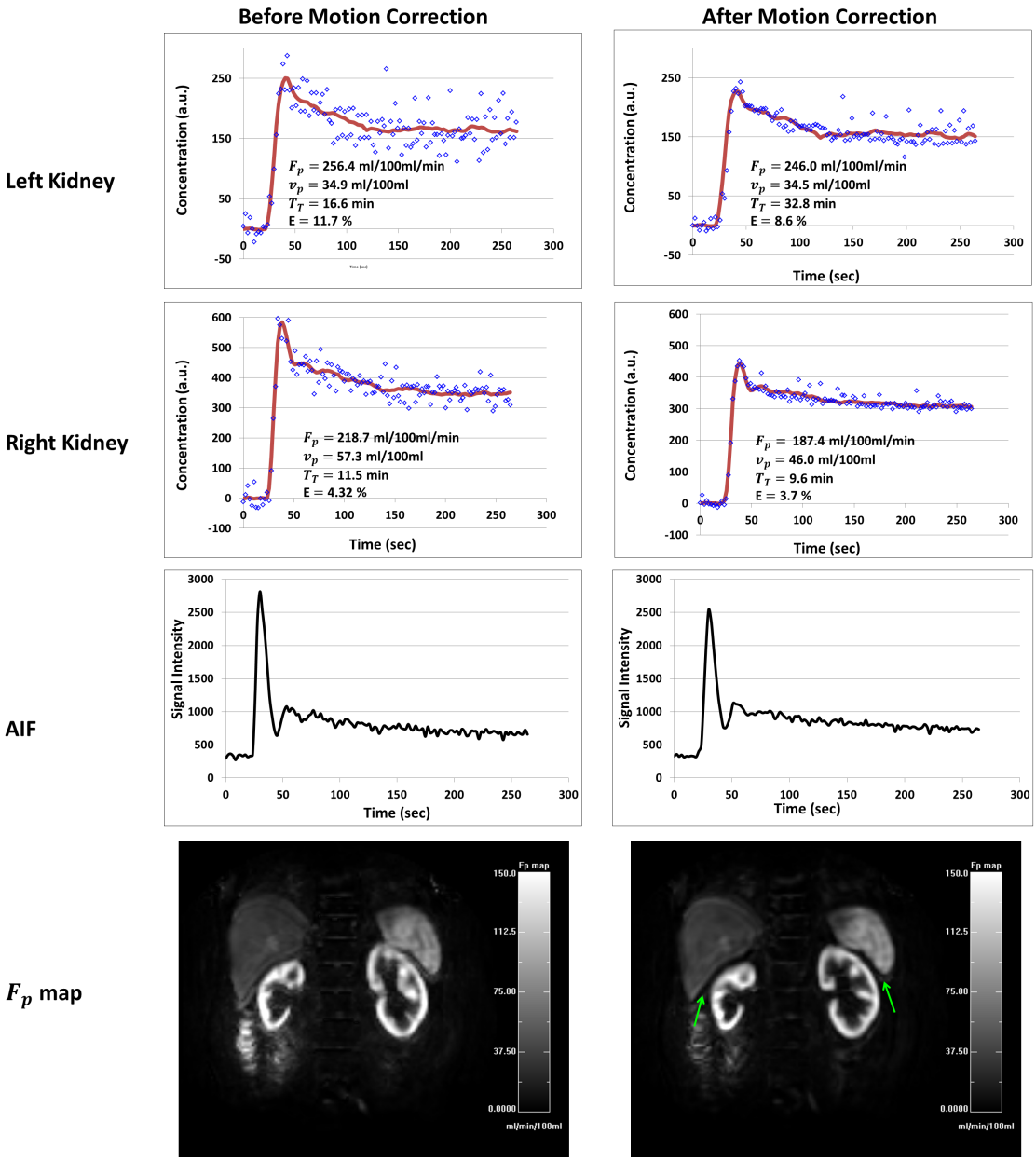

Figure 5.9: Effects of motion correction in Patient 3 data. The first two rows show the plots of the concentration-time curves (blue dots) and the two-compartment filtration model fit (red line) before and after motion correction for each kidney ROI. The third row shows the signal intensity curves of the AIF before and after motion correction. Bottom row shows the plasma flow (F_p) maps before and after motion correction.

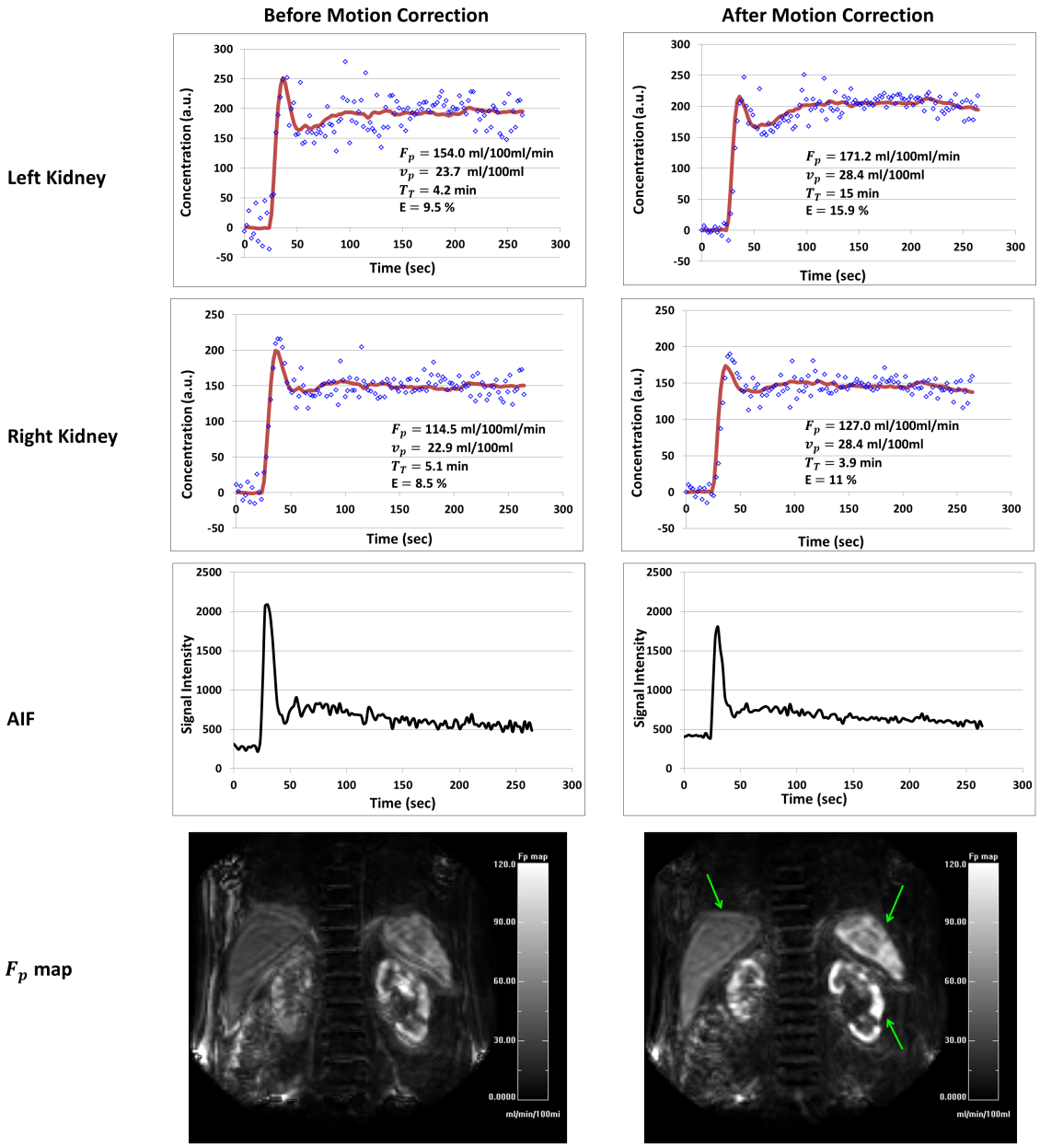

Figure 5.10: Effects of motion correction in Patient 4 data. The first two rows show the plots of the concentration-time curves (blue dots) and the two-compartment filtration model fit (red line) before and after motion correction for each kidney ROI. The third row shows the signal intensity curves of the AIF before and after motion correction. Bottom row shows the plasma flow (F_p) maps before and after motion correction.

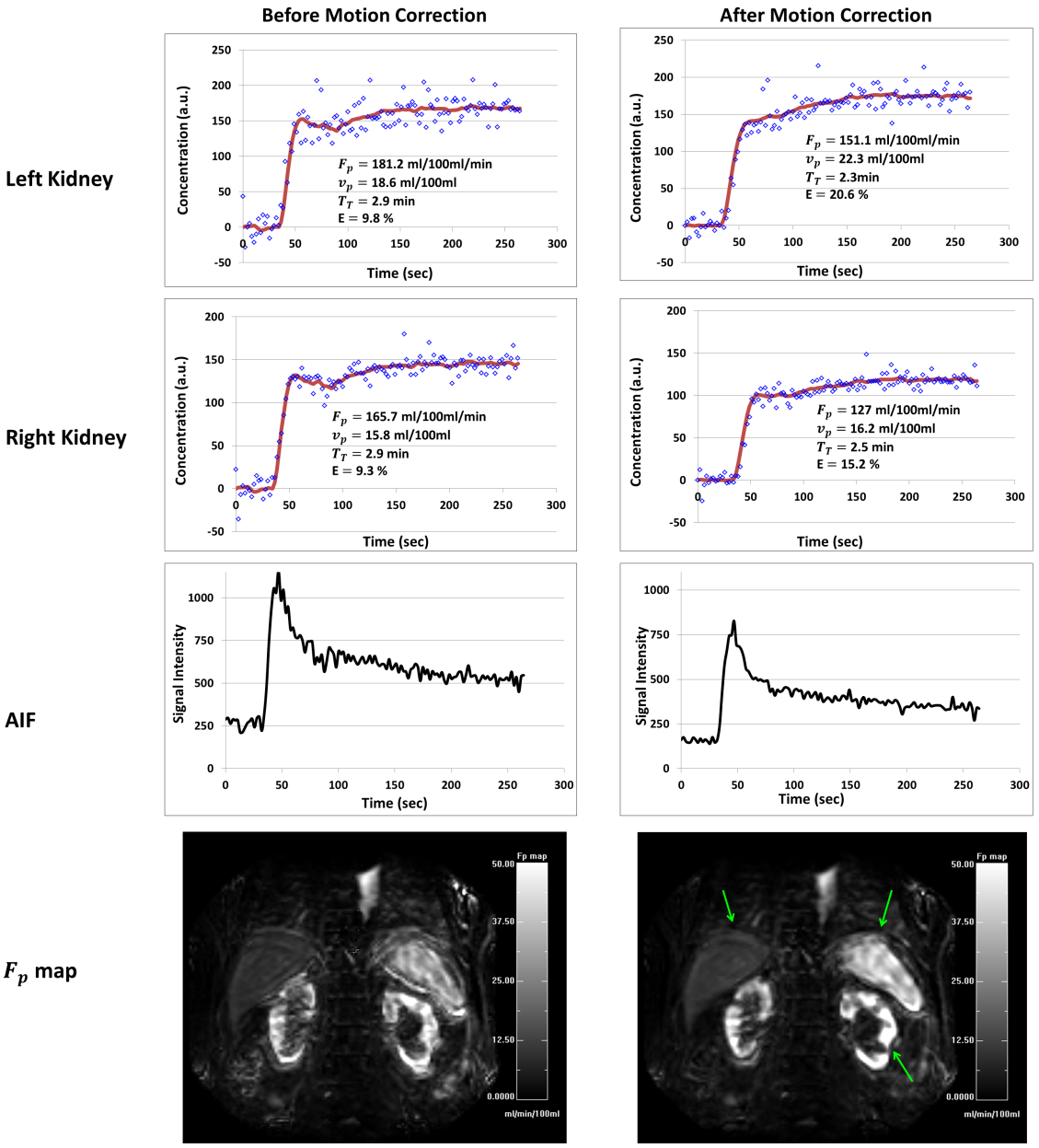

Figure 5.11: Effects of motion correction in Patient 5 data. The first two rows show the plots of the concentration-time curves (blue dots) and the two-compartment filtration model fit (red line) before and after motion correction for each kidney ROI. The third row shows the signal intensity curves of the AIF before and after motion correction. Bottom row shows the plasma flow (F_p) maps before and after motion correction.

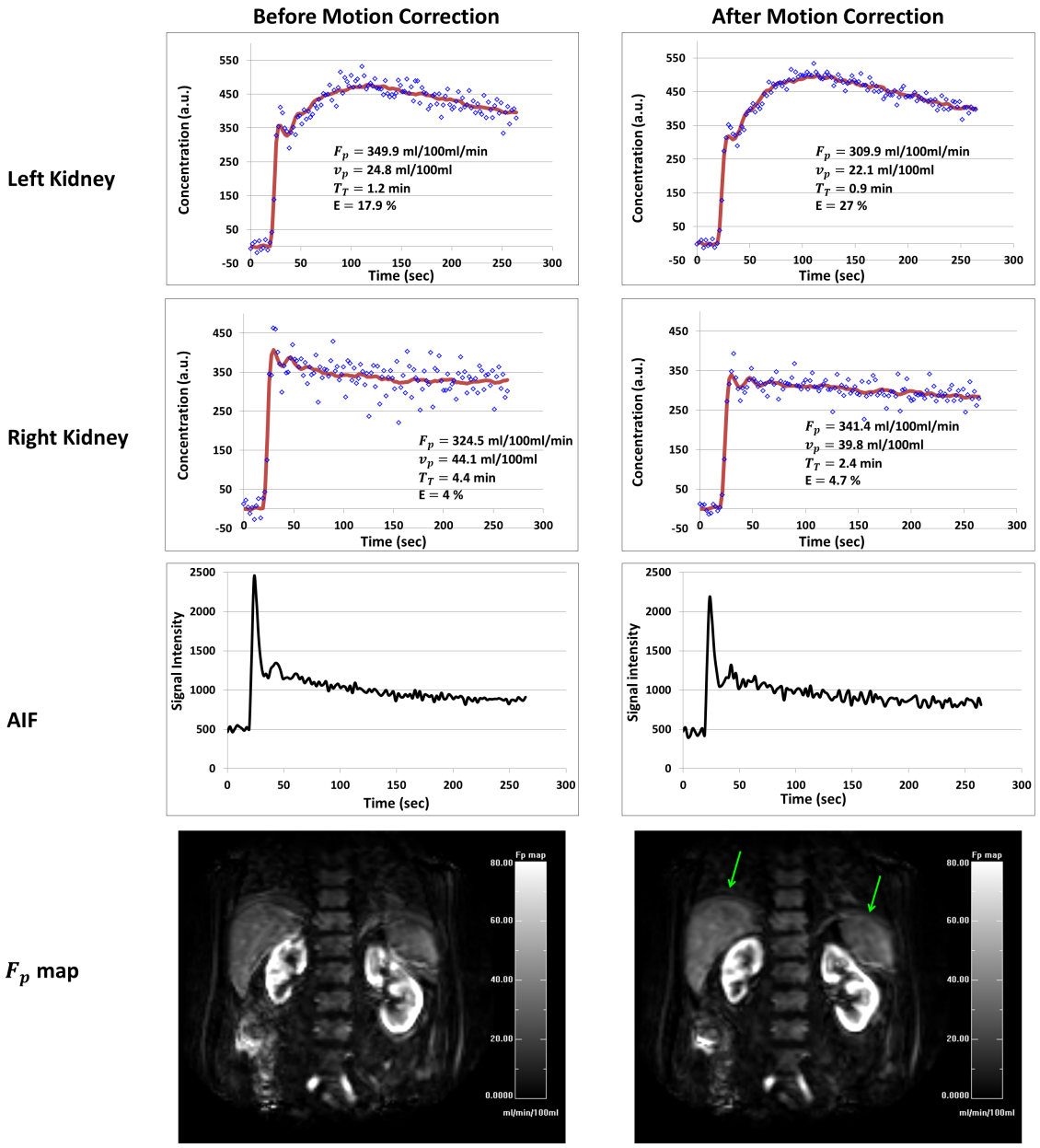

Figure 5.12: Effects of motion correction in Patient 6 data. The first two rows show the plots of the concentration-time curves (blue dots) and the two-compartment filtration model fit (red line) before and after motion correction for each kidney ROI. The third row shows the signal intensity curves of the AIF before and after motion correction. Bottom row shows the plasma flow (F_p) maps before and after motion correction.

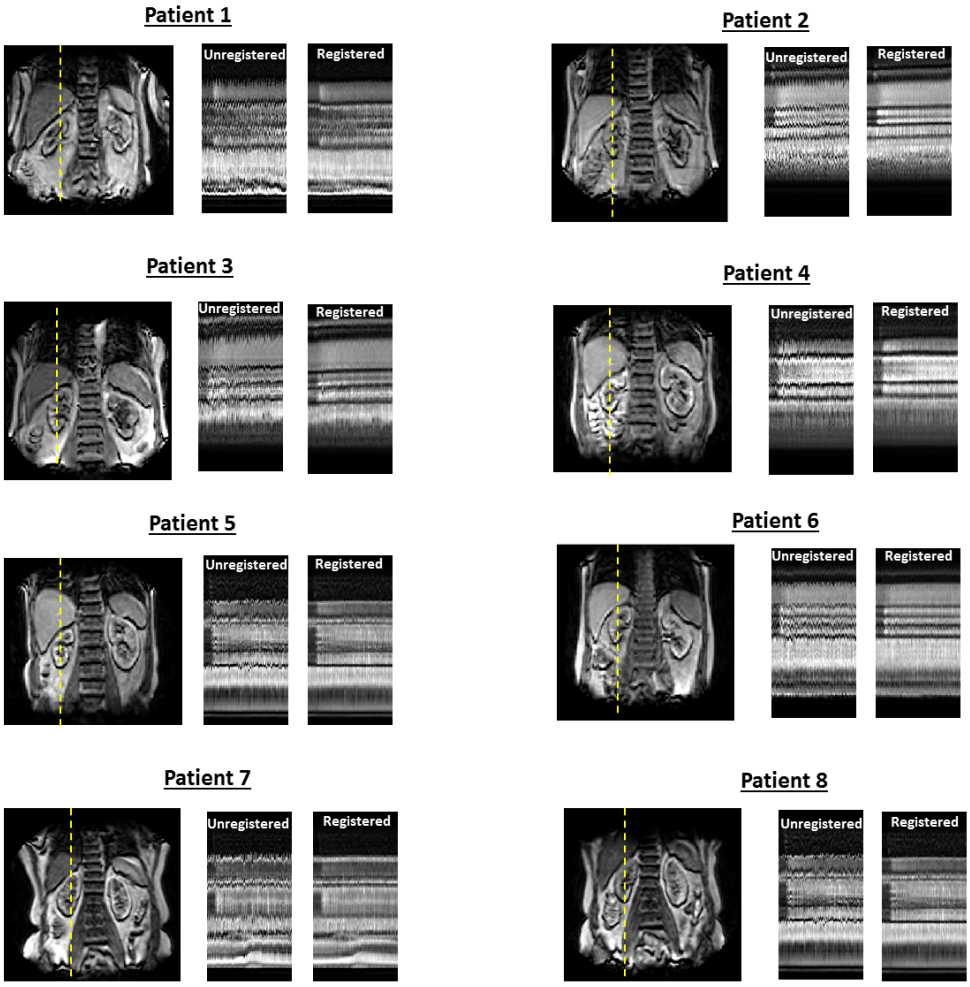

Figure 5.13: Effect of registration in superior-inferior direction in all patients. Coronal view for anatomical reference, a dashed line indicates the location of the time-cuts for unregistered and registered data.

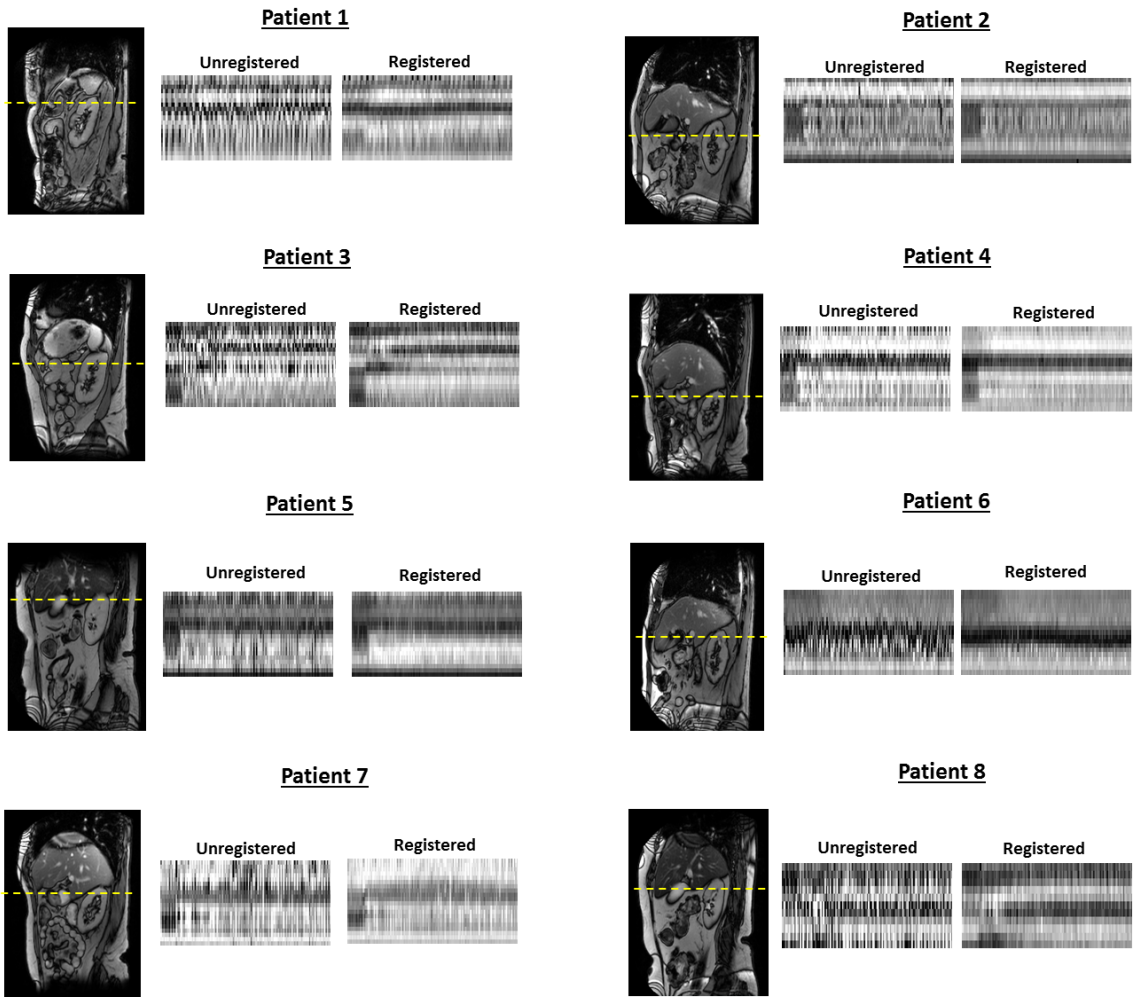

Figure 5.14: Effect of registration in anterior-posterior direction in all patients. Sagittal view for anatomical reference, a dashed line indicates the location of the time-cuts for unregistered and registered data.

5.4.2 Validation

DCE-MRI analysis of data before and after motion correction was compared to the gold-standard Iso SK-GFR values (Figure 5.15). Figure 5.15a shows the gold-standard Iso SK-GFR values compared with the SK-GFR values derived from DCE-MRI data before motion correction. Figure 5.15b shows the gold-standard Iso SK-GFR values compared with the SK-GFR values derived from DCE-MRI data after motion correction. Figure 5.15c shows the gold-standard Iso SK-GFR values compared with the SK-GFR values derived from DCE-MRI data after motion correction using AIF measured in data before motion correction. The results showed that motion correction reduces the systematic error and is most notably in Figure 5.15b. Similar observations can be made from Table 5.2. The results after motion correction showed no evidence of systematic error (after motion correction: P-value = 0.3259 and after motion correction using Orig AIF: P-value=0.0703), whereas results showed significant evidence of systematic error on SK-GFR measurements before motion correction (P-value=0.0262).

Figure 5.16 visualises the accuracy in terms of agreement between Iso SK-GFR and SK-GFR before motion correction (Figure 5.16a), after motion correction (Figure 5.16b) and after motion correction using Orig AIF (Figure 5.16c). Bland-Altman analysis showed a mean difference of 4.6 ml/min with 95% confidence interval of (-10 and +19 ml/min) between Iso SK-GFR and SK-GFR before motion correction, a mean difference of 1.1 ml/min with 95% confidence interval of (-14 and +16 ml/min) after motion correction and a mean difference of 3.3 ml/min with 95% confidence interval of (-10 and +16 ml/min) after motion correction using Orig AIF.

Linear regression analysis gave a slope of 0.96 with an intercept of -3.7 before motion correction, a slope of 1.03 with an intercept of -1.97 after motion correction and a slope of 0.99 with an intercept of -2.96 after motion correction using Orig AIF. Spearman's rank correlation with Iso SK-GFR were comparable for SK-GFR before motion correction ($\rho = 0.89$), after motion correction ($\rho = 0.91$) and after motion correction using Orig AIF ($\rho = 0.90$).

DCE-MRI analysis of four haemodynamic parameters (F_p, v_p, E, T_T) after motion correction was compared to the corresponding DCE-MRI parameters before motion correction. Figure 5.17 shows a graphic comparison of the haemodynamic parameters before and after motion correction.

Table 5.3 shows the gold-standard Iso SK-GFR values for each kidney compared with the SK-GFR values derived from DCE-MRI data before and after motion correction.

Table 5.4 shows the four haemodynamic parameters derived from DCE-MRI before and after motion correction. The parameters derived after motion correction compared with parameters before motion correction. There was no evidence of a significant difference across the F_p, v_p and E parameters after motion correction using Wilcoxon Signed-Rank test (P-value = 0.8, 0.2 and 0.1). However, significant difference showed between T_T parameter values (P-value = 0.027). Significant difference was also demonstrated between F_p, v_p, T_T and E parameter values before and after motion correction using Orig AIF (P-value = 0.002, 0.002, 0.004 and 0.002).

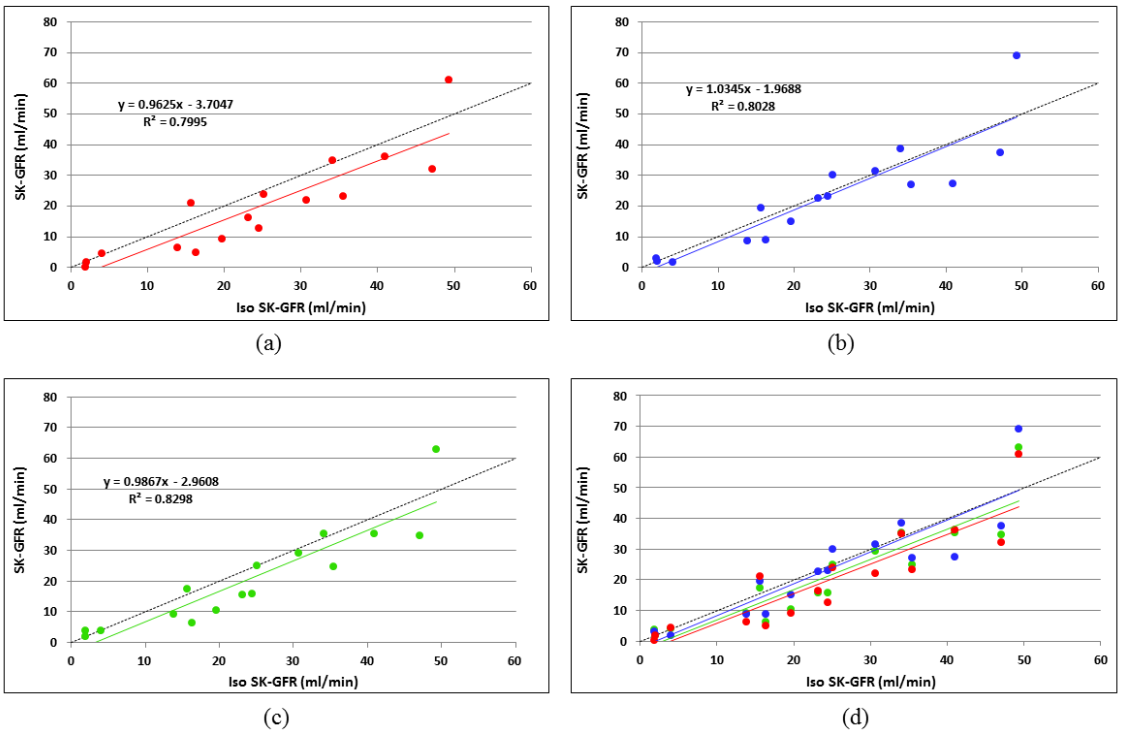

Figure 5.15: (a) Scatter plot shows the gold-standard Iso SK-GFR values compared with the SK-GFR values derived from DCE-MRI data before motion correction. (b) Scatter plot shows the gold-standard Iso SK-GFR values compared with the SK-GFR values derived from DCE-MRI data after motion correction. (c) Scatter plot shows the gold-standard Iso SK-GFR values compared with the SK-GFR values derived from DCE-MRI data after motion correction using AIF measured in DCE-MRI data before motion correction. (d) Scatter plot shows the gold-standard Iso SK-GFR values compared with the SK-GFR values derived from DCE-MRI data as described in (a), (b) and (c) cases.

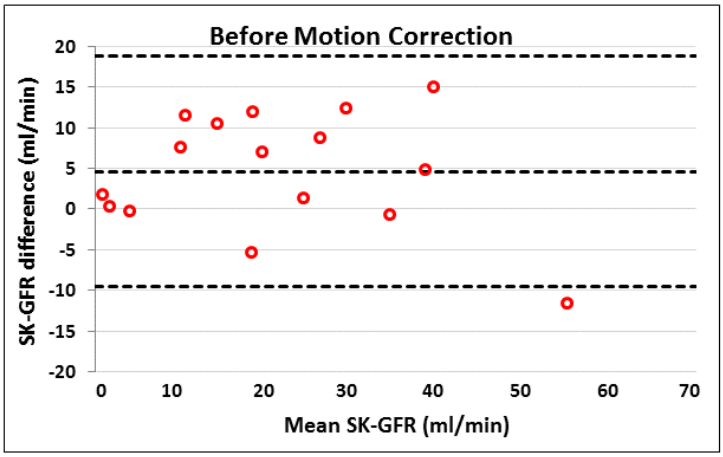

(a)

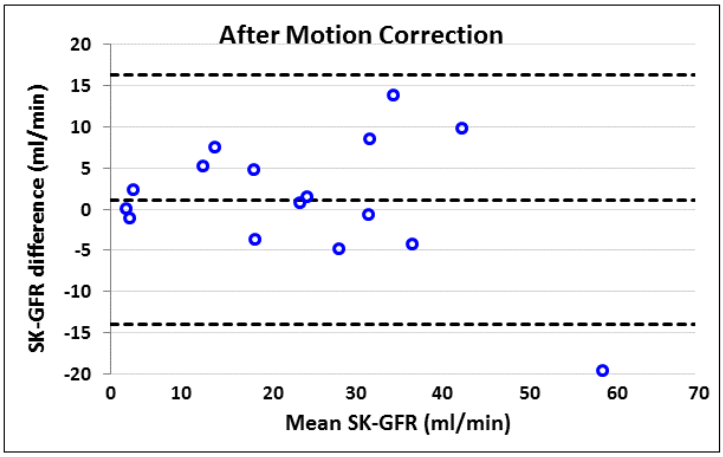

(b)

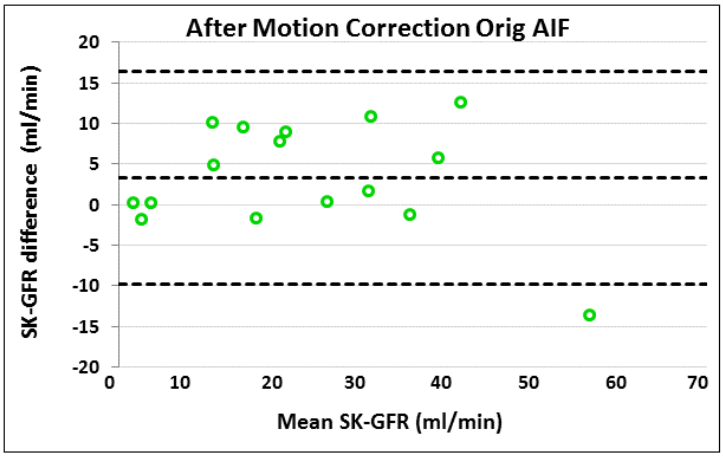

(c)

Figure 5.16: Bland-Altman plot comparing single-kidney glomerular filtration rate (SK-GFR) values derived from DCE-MRI and the gold-standard radioisotope method. DCE-MRI values derived (a) before motion correction, (b) after motion correction, (c) after motion correction using AIF measured in DCE-MRI data before motion correction. The y-axis shows the difference of MRI minus radioisotope. Dashed lines indicate the mean difference and 95% confidence intervals.

	ρ	**Mean Difference**	**95% CI of mean difference**	**P-value**
Before MC−Isotope	0.89	4.6 ml/min	-10 and +19 ml/min	0.0262*
MC−Isotope	0.90	1.1 ml/min	-14 and +16 ml/min	0.3259
MC Orig AIF−Isotope	0.91	3.3 ml/min	-10 and +16 ml/min	0.0703

Table 5.2: Spearman correlations (ρ), Mean difference with 95% Confidence Interval (CI) of SK-GFR measurements derived before motion correction (MC), after MC and after MC using Orig AIF. Mean Difference was considered to be statistically significant at a P-value of less than 0.05.

SK-GFR (ml/min)					
Patient	**Kidney**	**DCE-MRI** Before MC	**DCE-MRI** After MC	**DCE-MRI** After MC Orig AIF	**Isotope**
1	Left	21.04	19.45	17.4	15.63
	Right	0.26	3.09	3.80	1.87
2	Left	32.12	37.48	34.61	47.10
	Right	1.71	2.04	1.90	1.97
3	Left	36.20	27.30	35.28	40.96
	Right	4.38	1.08	3.92	4.02
4	Left	12.66	23.10	15.71	24.49
	Right	4.97	8.88	6.30	16.33
5	Left	16.19	22.56	15.54	23.14
	Right	9.17	15.00	10.30	19.64
6	Left	60.00	69.02	63.00	49.32
	Right	6.32	8.70	9.13	13.86
7	Left	23.88	31.00	24.90	25.10
	Right	22.04	31.47	29.20	30.70
8	Left	34.86	38.50	35.40	34.08
	Right	23.22	27.00	24.80	35.46

Table 5.3: Motion correction performance assessment: DCE-MRI SK-GFR values before and after motion correction and gold standard isotope SK-GFR values of left and right kidney in six clinical data sets.

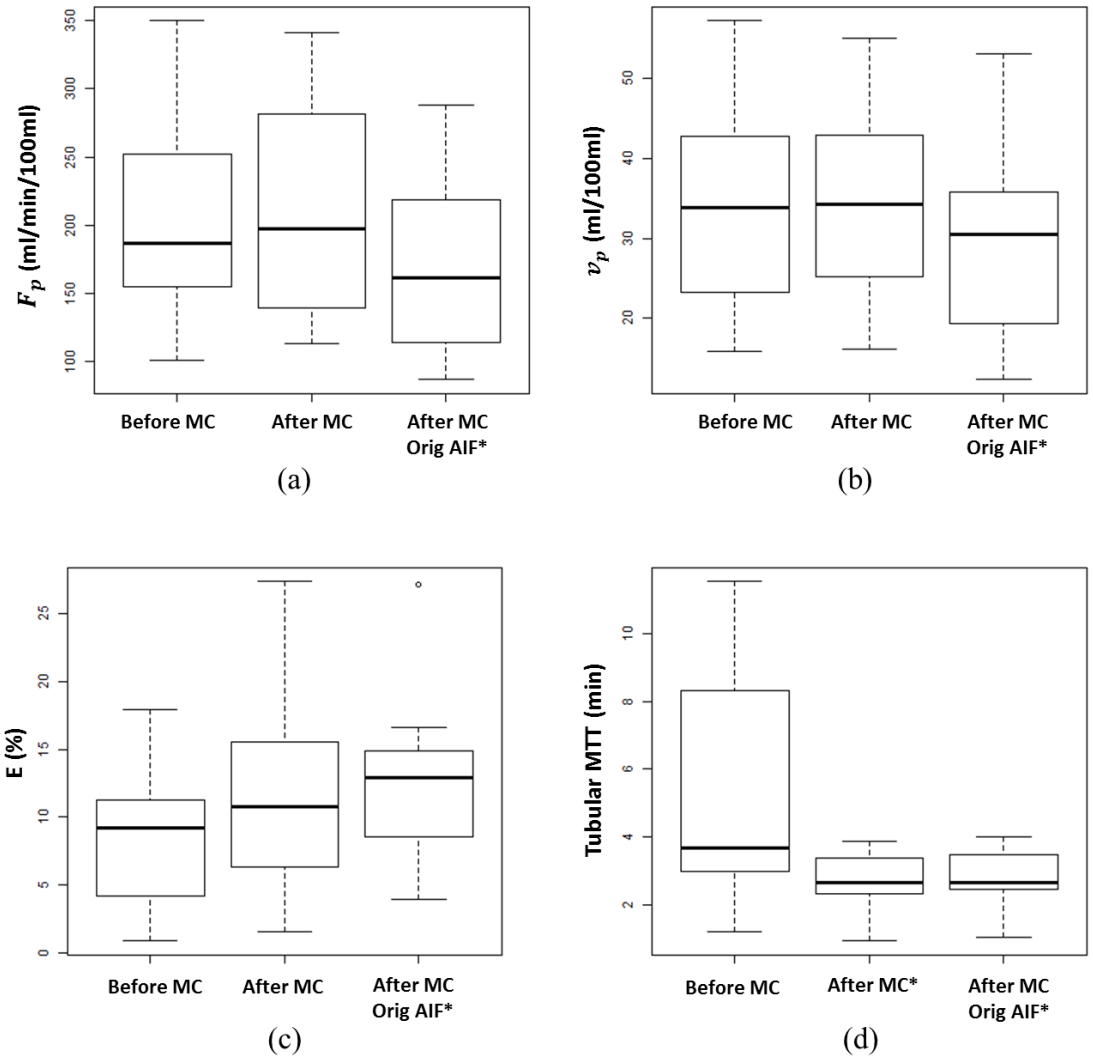

Figure 5.17: Each plot shows: the median (bold line), the 25th and 75th percentile (box), and the full data extent (dashed line). In plot (d) outliers were excluded from the graphical representation of the data for reasons of clarity. Significant difference compared to the before motion correction case is indicated by '*'. Symbol (∘) indicates an outlier.

Parameters	Before MC	After MC	After MC Orig AIF
F_p, ml· min^{-1}·100ml^{-1}	206 ± 78	213 ± 81	171 ± 69*
v_p, ml/100 ml	33± 13	35 ± 12	29±12*
Extraction fraction, %	9 ± 5	12 ± 7	13 ± 6*
Tubular MTT, min	3.6 ± 2	2.5 ± 1*	2.6 ± 1*

Table 5.4: Values are means ± SD for the parameters before and after motion correction. In tubular MTT outliers were excluded from the analysis. *Statistically significant mean difference compared with parameter values before motion correction.

5.5 Discussion

5.5.1 Evaluation of motion correction performance

The work presented in this chapter addresses the problem of motion correction in 3D DCE-MRI time series. The present algorithm is a generalisation to 3D of the previous 2D tracer-kinetic model-driven registration algorithm introduced in Chapter 4.

In this study, the performance of the registration algorithm was tested on 8 ARVD patient data measured under free breathing. As depicted in Figures 5.1 - 5.6, the data suffered from significant ghosting artefacts as the acquisition time is similar in duration to the breathing cycle. The newly proposed algorithm is surprisingly insensitive to significant structured noise caused by within-frame breathing artefacts, as demonstrated through the different time frames. The algorithm generated visually appealing results as the between-frame motion is effectively removed without affecting the signal intensities. The effect of motion correction is also notably in Figures 5.7 - 5.12. Concentration-time curves show an increased smoothness after motion correction. More importantly, there is a visible difference in the resulting maps of plasma flow (F_p). Different organs such as kidneys, liver and spleen are originally strongly blurred because of structural error and actual motion. The parametric maps after motion correction show a decrease of motion artefacts and more notably at the edges of the kidneys, spleen and liver (see the arrows shown on the relevant figures). Furthermore, our results show that the proposed registration algorithm correct the motion in all three dimensions (see Figures 5.13 and 5.14).

Precomputation steps reduce the calculation times to 12 hrs. As the calculation

is easily parallelizable, this implies that convergence within minutes is feasible on multi-core workstations.

5.5.2 Validation

Interestingly, one should note that the motion correction has an effect on the signal intensities of the AIF (see Figures 5.7 - 5.12). This could be explained by the fact that the image registration has been performed on a very low resolution deformation field. The low resolution pixels especially those at the center of the deformation field, most likely contain part of the kidney structure and part of the aorta. Although the aorta is static there is movement in the kidney that needs to be corrected. When an FFD is applied on a low resolution grid, a deformation field can be obtained correcting the motion where it exists. However, at the same time the motion correction affects static structures such as the aorta due to the interpolation that is performed in order to obtain a high resolution deformation field. Given the fact that the aorta is static, its exclusion from the motion correction process could be applied as a potential solution. Another possible solution could be to use a high resolution deformation field in which the interpolation will affect much less the static structures. However, this will lead to significant increase in calculation times. The enhancement of signal due to Gd-based contrast agents is partly dependent on AIF. Therefore, AIF measurement has been found to have an influence on the spread of variability of DCE-MRI data analysis and a major impact on clinical outcomes [109, 110]. To this end, after motion correction SK-GFR values from DCE-MRI data have been derived in two different ways, as discussed in Section 5.3.4.2.

This study aimed to evaluate accuracy and precision in DCE-MRI derived SK-GFR measurements. We wished to test whether DCE-MRI measurements of SK-GFR were improved in the context of clinical routine by adding motion correction to the analysis. Our results showed good correlation between SK-GFR values derived from MRI and isotopes in all three cases that have been examined, we refer the reader to Table 5.2.

Compared to previous studies [99, 100, 101, 62] using radioisotope SK-GFR reference to determine accuracy in MR-derived SK-GFR, our results are in good agreement in terms of the mean difference, see Table 5.1. Our results suggest that there is no significant evidence of systematic error on SK-GFR measurements between MR-

derived measurements after motion correction and Iso SK-GFR. However, evidence of systematic error show on SK-GFR measurements derived from MR before motion correction compared to Iso SK-GFR.

Quantitative assessment showed that tracer-kinetic model-driven registration algorithm removes the residual bias in SK-GFR measurements (Figure 5.15). This is consistent with the fact that breathing motion causes a net displacement of the time curves because expiration has a longer duration than inspiration. With reference to Iso SK-GFR our findings of precision before motion correction are in good accordance with previous DCE-MRI studies of patients with ARVD [99, 62], reporting moderate precision. Compared to a previous study [103] in which DCE-MRI volumes were motion corrected before measurements of SK-GFR, our observations are broadly similar in terms of precision. That is, results suggest that precision has not been improved further after motion correction.

The above observations lead to the conclusion that the limiting factor to clinical utility is currently the lack of precision in SK-GFR rather than accuracy. Although data were motion corrected in the postprocessing phase our findings suggest that correction of between-frame motion does not resolve this problem. This leads to the conclusion that within-frame artefacts are probably the main driver for poor precision. A second potential source for poor precision is the use of simple baseline subtraction to estimate concentrations, although this approach has been previously used in similar studies [62, 103].

Compared to previous DCE-MRI study of patients with ARVD [62], our findings are in good accordance in terms of mean difference of the postprocesure parameters as illustrated in Table 5.4. The observed trend in tubular transit time gives rise to the hypothesis that this parameter is affected by motion error more than other parameters such as plasma flow, plasma volume and extraction fraction, see Figure 5.17. Thus, a potential source of overestimation in the mean transit time parameter is the motion error. The results suggest that there is a significant mean difference in this parameter before and after motion correction (Table 5.4).

5.5.3 Study Limitations

The number of kidneys studied was relatively low. The significance levels were weak, and some effects that appear systematic error on a visual inspection did not reach statistical significance (e.g. Figure 5.15(c)). It is therefore necessary to perform the study on a larger sample size. Another potential limitation of our work is related to the assumption of a linear relationship between signal intensity and contrast agent concentration. The kinetic parameters in the concentration time curves were calculated by subtracting pre-contrast (baseline) signal from post-contrast signal, as discussed in Section 5.3.4.1. However, it is well-known that this relation is nonlinear in MR especially at higher concentrations. In this study a quarter of a standard dose of contrast agent is injected so that the effect is relatively smaller than in typical DCE-MRI studies.

5.6 Conclusion

In conclusion, the motion correction method allows improved registration of multiple free breathing renal DCE-MRI time series. The tracer-kinetic model driven registration algorithm effectively removes between-frame breathing motion. With reference to Iso SK-GFR, SK-GFR derived from DCE-MRI for both before and after motion correction achieved low bias, but only had a moderate precision. Although DCE-MRI appears to be a promising one-stop tool for the determination of SK-GFR, clinical translation will require removal of within-frame artefacts which can only be achieved by integrating motion correction in the image reconstruction process.

Chapter 6

General Conclusions and Future Work

The overall aim of this work in thesis was to develop and evaluate an image registration algorithm which incorporates a 4-parameter 2-compartment tracer-kinetic model to motion correction process to account for signal intensity changes due to the passage of contrast agent. In the work presented in the different chapters a number of challenges were addressed: linearisation of two-compartment models, motion correction, computational complexity of non-rigid registration algorithms, and assessment of SK-GFR after motion correction in patients with ARVD in the context of clinical routine.

6.1 Conclusions

After a preliminary introduction and theoretical background in Chapter 1 and 2, Chapter 3 developed a new LLS fit for the 2CXM and 2CFM. This chapter also presented a LLS method of simpler models such as the Tofts model and modified Tofts model. The results suggested that the LLS method for the Tofts model and modified Tofts model is more efficient than the NLLS method and has comparable accuracy. The LLS method for solving the 2CXM or 2CFM reduces the computation times by two orders of magnitude, and is at least as accurate and precise as the NLLS method at low noise levels. However, at higher noise levels the LLS became

exceedingly inaccurate compared to the NLLS. The results suggested that this may be improved though by using a suitable weighting strategy. A large amount of this work was published in [44].

Chapter 4 introduced a novel image registration technique for correction of misalignments induced by inter frame motion on 2D DCE-MRI data. The proposed method, named tracer-kinetic model-driven registration is inspired by the work of other research groups and combined advantageous approaches into one method. The registration algorithm was initially tested on a contrast enhancement simulated phantom incorporating a rigid and nonrigid motion. Quantitative evaluation against ground truth demonstrated that the algorithm removed the motion induced error. The proposed motion correction method has been tested on 2D renal DCE-MRI data. The results illustrated that the motion correction algorithm allowed significant improvement of tissue time-intensity curves compared to corresponding ones before motion correction. The successful motion correction of multiple datasets using the same algorithm settings suggest the method is robust. This chapter also investigated the inclusion of some computational performance benefits into the tracer-kinetic model-driven registration algorithm. The computational complexity of non-rigid registration algorithms has been addressed by precomputing the gradients of the cost function as well as the coefficients of B-splines to remove redundant calculations. The computational performance of the proposed algorithm has been significantly improved, and in particular it was found that the precomputation steps reduced the calculation times for one slice from 5 hrs to 20 min.

Chapter 5 presented an extension to 3D renal DCE-MRI data in the presence of free breathing of the tracer-kinetic model-driven registration algorithm described in Chapter 4. The translation to 3D has brought an additional challenge due to ghosting artefacts caused by within-frame breathing motion. Visual inspection of plasma flow maps and visual comparison of corrected and uncorrected time frames were used as a method of evaluation. The results suggested that the motion correction algorithm has effectively removed between-frame breathing motion despite the significant within-frame artefacts. In addition, the computational cost has increased to 12-13 hrs. Although the exponential increase in computational complexity was inevitable there is significant room for improvement. Chapter 5 also examined the effect of motion correction on clinical utility. Quantitative evaluation of SK-GFR derived from DCE-MRI against reference measurements showed a reduction of the bias, but precision is limited by within-frame artefacts. This suggests that the clin-

ical translation will require removal of within-frame artefacts, which can only be achieved by integrating motion correction in the reconstruction process. The selection of AIF has been noted to have an influence on the DCE-MRI measures and a more extensive investigation is thus required. Although promising results were obtained with the proposed heuristic method, a complete validation is necessary to fully assess the potential benefit of such a semi-automated technique.

From a general point of view, this thesis aimed at improving the accuracy and reliability of image analysis in quantitative DCE-MRI. The 4-paremeter tracer-kinetic model-driven registration algorithm has been proposed, designed specifically for the motion correction of contrast enhanced data. The inclusion of computational performance benefits have been demonstrated. The proposed algorithm has been demonstrated on clinical data and simulated phantoms with contrast variations. The work undertaken leads to the observation that the said image registration algorithm effectively removes between-frame breathing motion.

6.2 Future Work

A number of possible extensions and future directions might be considered. The use of tracer-kinetic model driven registration is not limited to the application presented in this thesis and can be extended to other application such as liver, spleen or heart. There are no fundamental differences other than those relating to selecting an appropriate tracer-kinetic model for the alternative application.

The 2CFM presented in Chapter 3 does not include a delay parameter. Future work could take into account the delay of the arrival of contrast agent between the artery and the tissue. It is a limitation of the method as discussed in Chapter 3 that a delay parameter was not included in the model. As seen in Figure 4.15(a), the proposed motion correction algorithm does not produce very accurate motion correction in Subject 3 due to the long delay between the artery and the kidney. The inclusion of a delay parameter in 2CFM could possibly also fix this disturbance.

A few refinements of the motion correction algorithm could also be of interest in future work. The time frames are independent of each other and therefore the algorithm is easily parallelizable. Consequently, each time frame can be thought of as an individual registration. The parallel formation of the proposed algorithm

by running each registration on a graphical processing unit (GPU) will make the algorithm converge faster. This implies that convergence of the algorithm within minutes is feasible on a multi-core workstation.

The work in this thesis assumed a linear relation between the signal intensities and the contrast agent concentration. MR signal intensity has been converted to contrast agent concentration using the relation given in Eq.(4.3), as introduced in Chapter 4. However, this is a good approximation only when the concentrations are not too big. For higher concentrations this assumption is not very accurate. A more accurate way to obtain the concentrations is to use Eq.(2.7) which requires an estimate of the precontrast T_1 (i.e. $T_{1,0}$). Recently, Dickie et al. [111] proposed that the joint estimation of T_1 mapping and dynamic data improves the accuracy and precision of tracer-kinetic parameters. In the spirit of the paper by Dickie et al. it may be beneficial to further develop a joint temporal model to account for dynamic data as well as precontrast data. Thus, a natural extension of the work outlined in this thesis is the motion correction of the dynamic data as well as the precontrast data (T_1 mapping). The hypothesis underlying this future work is that the joint motion correction would improve the accuracy and precision of the estimated tracer kinetic parameters, and consequently the assessment of SK-GFR. This would be a good extension of the work presented here and there are no direct theoretical problems other than those relating to joint temporal model which describes both the dynamic and precontrast data.

Appendix A

Numerical Evaluation of the Convolution

The NLLS implementation in this study uses an efficient and accurate iterative algorithm for the evaluation of a convolutions with an exponential factor:

$$f(t) = a(t) \otimes \frac{e^{-t/T}}{T} \equiv \frac{1}{T} \int_0^t d\tau \, a(\tau) \, e^{-(t-\tau)/T}. \tag{A.1}$$

The algorithm applies to situations where the function $a(t)$ is measured and thus only available at discrete times $t_0 = 0, t_1, t_2, \ldots, t_{n-1}$ (not necessarily uniformly spaced).

With $T = 0$ the result is $f(t) = a(t)$. With $T \neq 0$ the integral is evaluated by interpolating linearly between the values $a_i = a(t_i)$, leading to an iterative formula with starting value $f(t_0) = 0$:

$$f(t_{i+1}) = e^{-x_i} f(t_i) + a_i E_0(x_i) + a'_i T E_1(x_i), \qquad i \geq 0, \tag{A.2}$$

where

$$E_0(x) = \int_0^x e^{-(x-u)} du = 1 - e^{-x}, \tag{A.3}$$

$$E_1(x) = \int_0^x u e^{-(x-u)} du = x - E_0(x) \tag{A.4}$$

and

$$x_i \equiv \frac{t_{i+1} - t_i}{T}, \qquad a'_i \equiv \frac{a_{i+1} - a_i}{t_{i+1} - t_i}. \tag{A.5}$$

Compared to standard numerical convolution, Eq. (A.2) is more accurate because the exponential factor is not approximated. It is also more efficient computationally due to its iterative nature.

To prove the results, consider first the case $T = 0$:

$$\lim_{T\to 0} \frac{e^{-t/T}}{T} * a(t) = \delta(t) * a(t) = a(t) \tag{A.6}$$

For any other T, note that the initial value is $f(t_0) = 0$ since $t_0 = 0$. Now given $f(t_i)$, the value $f(t_{i+1})$ can be determined by splitting up the integral and substituting $u = (\tau - t_i)/T$:

$$\begin{aligned}
& \frac{1}{T}\int_0^{t_{i+1}} d\tau\, a(\tau)\, e^{-(t_{i+1}-\tau)/T} \\
= \;& \frac{1}{T}\int_0^{t_i} d\tau\, a(\tau)\, e^{-(t_{i+1}-\tau)/T} \\
+ \;& \frac{1}{T}\int_{t_i}^{t_{i+1}} d\tau\, a(\tau)\, e^{-(t_{i+1}-\tau)/T} \\
= \;& \frac{1}{T}\int_0^{t_i} d\tau\, a(\tau)\, e^{-x_i-(t_i-\tau)/T} \\
+ \;& \int_0^{x_i} du\, a(t_i + Tu)\, e^{-(x_i-u)} \\
\approx \;& e^{-x_i} f(t_i) + \int_0^{x_i} du\, (a_i + a'_i T u)\, e^{-(x_i-u)}
\end{aligned}$$

Eq. (A.2) then follows directly from the definitions (A.3) and (A.4). The linear interpolation between data points is made in the second term of the last line, and is the only approximation made.

Appendix B

Tracer-Kinetic Model-Driven Registration Algorithm Source Code

B.1 Algorithm Architecture

B.1.1 Multiresolution Procedure

```
This function performs a multiresolution strategy for image registration.
The default implementation proceeds progressively from coarse-to-fine
resolution as described in Section 4.3.2.5.
-------------------------------------------------------------------------

FUNCTION pkreg_mres, Time, Ca, Source, Baseline

  Nt = n_elements(Source[0,0,*])
  step = 1.0  ;precision value see the Optimisation Section 4.4.3
  nd = [2L, 4L, 8L, 16L, 32L] ;resolution levels of the deformation field
  itmax =[5L, 5L, 5L, 4L, 4L] ;max number of iter at each resolution level
  it = 0L
  d = fltarr(2,nd[it],nd[it],Nt)  ;initialise deformation field

 ;Perform registration at lowest resolution level
  pkreg, Time, Ca, Source, Baseline, d=d, itmax=4., step=step

 ;Perform registration at contiguous resolution levels
  FOR it=1L,n_elements(nd)-1 DO BEGIN  ;looping over resolution levels
      d = ffd_interpol(d, [nd[it],nd[it]])
      pkreg, Time, Ca, Source, Baseline, d=d, itmax=itmax[it], step=step
```

```
  ENDFOR

;Return Corrected image
RETURN, ffd_dynamic(Source, d)

END
```

B.1.2 Tracer-Kinetic Model-Driven Registration

```
This function performs time point by time point registration. Each measured
source image (I_source) is registered using FFD to its corresponding target
image (I_target). The deformation field is then applied to source images
creating the corrected images, (I_corr).
-------------------------------------------------------------------------

PRO pkreg, Time, Ca, Source, Baseline, d=d, itmax=itmax, step=step

 ;max number of iter at each resolution level
 if n_elements(itmax) eq 0 then itmax=5

 Nt = n_elements(Source[0,0,*])

 ;Initialise the Corrected image
 Corr = ffd_dynamic(Source, d)

 ;Register
  FOR it=1L,itmax DO BEGIN
    ;Create Target images
    Target = pkfit(Time, Ca, Deformed, Baseline) ;fit the 2CFM pixel-by-pixel

    FOR t=0L, Nt-1 DO BEGIN
      ffd_precompute, REFORM(Source[*,*,t]), size(REFORM(d[0,*,*,0]), $
                                                  /dimensions)
      d[*,*,*,t] = ffd_reg(REFORM(Source[*,*,t]), REFORM(Target[*,*,t]),  $
                                            REFORM(d[*,*,*,t]), step=step)
      Corr[*,*,t] = ffd(REFORM(Source[*,*,t]), REFORM(d[*,*,*,t]))
    ENDFOR

  ENDFOR

END
```

B.1.3 FFD Image Registration

```
This function performs FFD image registration. After image registration
is done the function returns the deformation field that is to apply later
on I_corr.
-------------------------------------------------------------------------

FUNCTION ffd_reg, Source, Target, d, step=step, itmax=itmax
```

```
 ;See Optimisation Section 4.4.3
 if n_elements(itmax) eq 0 then itmax = 300. ;max iter
 if n_elements(step) eq 0 then step = 1.0 ;precision value

 dreg = d

 ffd_precompute,Source,size(REFORM(d[0,*,*]), /dimensions)
 ffd_grad_precompute, size(REFORM(d[0,*,*]), /dimensions)

  FOR it=1L, itmax DO BEGIN
      G = ffd_grad(Source, Target, dreg) ;calculate gradients
      ;perform line search
      Breg = ffd_lsearch(Source, Target, dreg, G, conv=converged, step=step)
      if converged then return, dreg
  ENDFOR

RETURN, dreg

END
```

B.2 Precomputation Steps

B.2.1 FFD

```
This function calculates the displacement of an arbitrary point (x,y) of
the I_corr using the Taylor expansion series as illustrated in Eq.(4.23)
in Chapter 4.  It gives as output the I_corr at the given deformation field
(d) using the I_source.
-------------------------------------------------------------------------------


FUNCTION ffd, Source, d, Corr_x, Corr_y

;load precompute matrices
COMMON ffd_const, pi, qi, ri, si, p, q, r, s, xs, ys, S_x, S_y, S_xy

 dx = REFORM(d[0,*,*])
 dy = REFORM(d[1,*,*])

  ;For a Source image with (Nx, Ny) pixels, the xs and ys are (Nx, Ny)
  ;arrays with x and y locations of pixels centers assuming x=0 and y=0
  ;in the corner of the lower left pixel.
  ;xs and ys correspond to x- and y-pixel locations in the Source
  ;pi is the index of the lower left corner of the unit square
  ;p is the weight correspond to pi
  ;See Fig.4.1 where xs, ys are the locations of the high resol grid
  ;and pi,qi,ri,si are the indices of the nodes of the lower resol grid
  x = xs + p*dx[pi] + q*dx[qi] + r*dx[ri] + s*dx[si]  ;Eq.(2.54)
  y = ys + p*dy[pi] + q*dy[qi] + r*dy[ri] + s*dy[si]
```

```
  ns = size(Source, /dimensions)
  Corr = fltarr(ns)
  ;Identify the locations inside the bounds of the image domain
  interior = where((x GE -0.5E) AND (x LE ns[0]-0.5E) AND (y GE -0.5E) $
                                          AND (y LE ns[1]-0.5E), cnt)
  if cnt eq 0 then begin
    if arg_present(Corr_x) then Corr_x = fltarr(ns)
    if arg_present(Corr_y) then Corr_y = fltarr(ns)
    return, Corr
  endif

  xi = x[interior]
  yi = y[interior]
  i = long(xi)
  j = long(yi)
  u = xi - i ;the horizontal distance of the def. field cell,see Fig 2.18
  v = yi - j ;the vertical distance of the def. field cell
  ;The following formula is equivalent to Eq.(4.23)
  Corr[interior] = Source[i,j] + u*S_x[i,j] + v*S_y[i,j] + u*v*S_xy[i,j]

  if arg_present(Corr_x) then begin
    Corr_x = fltarr(ns)
    Corr_y = fltarr(ns)
    Corr_x[interior] = S_x[i,j] + v*S_xy[i,j]
    Corr_y[interior] = S_y[i,j] + u*S_xy[i,j]
  endif

RETURN, Corr

END
```

B.2.2 Precomputation of B-spline Coefficients

```
This function precomputes the B-spline coefficients of Eq.(2.54) and calculates
the numerical derivatives of the source image so can be use later in FFD
procedure. Look at Figure 4.1 for direct comparisons.
-------------------------------------------------------------------------------

PRO ffd_precompute, Source, nd

  COMMON ffd_const, pi, qi, ri, si, p, q, r, s, xs, ys, S_x, S_y, S_xy

  ns = size(Source, /dimensions)
  nx = ns[0]
  ny = ns[1]
  xind = findgen(nx)
  yind = findgen(ny)

  ds = (nd-1E)/ns ;(x,y)-distance between pixels (Deformation field pixelsize=1)
  x = ds[0]/2 + ds[0]*xind  ;x-coord of image pixels
```

```
  y = ds[1]/2 + ds[1]*yind  ;y-coord of image pixels
  x = rebin(x, nx, ny)
  y = rebin(transpose(y), nx, ny)
  ;round off x- and y-coord to get the closest lower left corner of
  ;the unit square
  i = long(x)
  j = long(y)
  u = x - i
  v = y - j

  pi = i + j*nd[0] ;index of lower left corner of a unit square
  qi = pi + 1 ; lower right corner
  ri = pi + nd[0] ;upper left corner
  si = pi + nd[0] + 1 ;upper right corner

  ;See example of bilinear interpolation in Section 2.6.1.4
  p = (1-u)*(1-v) ;weight correspond to pi
  q = u*(1-v) ;weight correspond to qi
  r = (1-u)*v ;weight correspond to ri
  s = u*v ;weight correspond to si

  xs = rebin(xind, nx, ny) ;x-coord of image pixels (image pixelsize=1)
  ys = rebin(transpose(yind), nx, ny) ;y-coord of image pixels

  ;Calculate the numerical derivatives of the I_source
  S_x = Source[xind[1:nx-1],*] - Source[xind[0:nx-2],*]
  S_y = Source[*,yind[1:ny-1]] - Source[*,yind[0:ny-2]]
  S_xy = S_x[*,yind[1:ny-1]] - S_x[*,yind[0:ny-2]]

END
```

B.2.3 Gradient Computation

```
This function calculates the analytical gradient at the nonzero locations of
the image which were precomputed and stored in the function called
ffd_grad_precompute.
-------------------------------------------------------------------------------

FUNCTION ffd_grad, Source, Target, d

  dx = REFORM(d[0,*,*])
  dy = REFORM(d[1,*,*])

  n = size(Bx, /dimensions)

  n = n[0]*n[1]
  if n_elements(Gx) eq 0 then Gx = fltarr(n)
  if n_elements(Gy) eq 0 then Gy = fltarr(n)
  Res = Target - ffd(Source, d, Corr_x, Corr_y)   ;Calculate the residual

 ;Weight is an array with weighted averages of the control point
```

```
 ;displacements in a neighborhood area around each pixel
 ;Calculate the gradient at nonzero locations (loc) of the image
 ;Load precomputing matrices
 ;Weight_cnt is an array which stores the locations with nonzero weights
 ;Weight_loc is an array which is 1 at a certain location and 0 elsewhere
  COMMON ffd_grad_const, Weight, Weight_cnt, Weight_loc

  i0=0L
  FOR i=0L,n-1 DO BEGIN
      Bi_cnt = Weight_cnt[i]
      Bi_loc = Weight_loc[i0:i0+Bi_cnt-1]
      Bi = Weight[i0:i0+Bi_cnt-1]
      i0 = i0+Bi_cnt
      Bi = Bi*Res[Bi_loc] ;Compute Residual before hand
      Gx[i] = - total(Bi*Corr_x[Bi_loc])  ;gradient at x-direction Eq.(4.19)
      Gy[i] = - total(Bi*Corr_y[Bi_loc])  ;gradient at y-direction Eq.(4.20)
  ENDFOR

  ;Normalised Gradients
  Gnorm = max(sqrt(Gx^2+Gy^2))
  Gx = Gx/Gnorm
  Gy = Gy/Gnorm

  G = d
  G[0,*,*] = Gx
  G[1,*,*] = Gy

RETURN, G

END
```

B.2.4 Precomputation of Gradient

```
The Weights here correspond to the linear B-spline functions (B). We create
a dummy deformation field (d_dummy) which is 1 at one particular location and
0 elsewhere.The nonzero locations are stored in an array called Bi_loc so that
can be used later in the gradient computation.
-------------------------------------------------------------------------------

PRO ffd_grad_precompute, nd

  ;define precomputing matrices
  COMMON ffd_grad_const, Weight, Weight_cnt, Weight_loc
  COMMON ffd_const, pi, qi, ri, si, p, q, r, s

  n = nd[0]*nd[1]
  ns = n_elements(p)
  Weight_cnt = lonarr(n)
  Weight_loc = lonarr(4*ns)
  Weight = fltarr(4*ns)
  d_dummy = fltarr(n)
```

```
  i0=0L
  FOR i=0L,n-1 DO BEGIN
    d_dummy[i] = 1 ;dummy deformation field set to 1 at particular location
    ;We get the weighting function (Bi)
    Bi = p*d_dummy[pi] + q*d_dummy[qi] + r*d_dummy[ri] + s*d_dummy[si]
    d_dummy[i] = 0
    ;We find the locations where the Bi is nonzero
    Bi_loc = where(Bi ne 0, Bi_cnt)
     Weight_cnt[i] = Bi_cnt
    ;We store the nonzero locations
    Weight_loc[i0:i0+Bi_cnt-1] = Bi_loc
    Weight[i0:i0+Bi_cnt-1] = Bi[Bi_loc]
    i0 = i0+Bi_cnt
  ENDFOR

END
```

B.3 Supplementary Functions

B.3.1 Initialise FFD Registration

```
This function apply an FFD to all Source images and returns the motion
corrected images.
-------------------------------------------------------------------------
FUNCTION ffd_dynamic, Source, d

Nt = n_elements(Source[0,0,*])

;Initialise
  Corr = Source

;Apply the FFD at all time points
 FOR t=0L, Nt-1 DO BEGIN
     ffd_precompute, REFORM(Source[*,*,t]), size(REFORM(d[0,*,*,0]), $
                                                        /dimensions)
     Corr[*,*,t] = ffd(REFORM(Source[*,*,t]), REFORM(d[*,*,*,t]))
 ENDFOR

RETURN, Corr
END
```

B.3.2 2CFM Fit

```
This function computes the 2CFM fit via a linear least-squares method. For
details see Flouri et al MRM (2016).
-------------------------------------------------------------------------
FUNCTION pkfit, Time, Ca, St, n0, params=params

 ;St: signal intensity of measured data
 ;n0:  number of baseline time points
 ;params : 4-element floating point array with the values [FP, TP, PS, TE]

  n = size(St, /dimensions)
  S0 = total(St[*,*,0:n0-1],3)/n0   ;estimate baseline
  S0 = rebin(S0,n[0],n[1],n[2])
  Ct = St - S0    ;conversion from signal to concentration (Eq.(4.3))

  Fit = S0
  params  = fltarr(n[0],n[1],4)

  FOR i=0L, n[0]-1 DO BEGIN
    FOR j=0L, n[1]-1 DO BEGIN
        params [i,j,*] = LLS_2CFM(Time, REFORM(Ct[i,j,*]),Fit=Cfit_ij,ca)
        Fit[i,j,*] += Cfit_ij
    ENDFOR
  ENDFOR

  RETURN, Fit
END
```

B.3.3 Linear Least-Squares Method

```
This function calculates the 4-parameters of the 2CFM via a linear least-
squares method as introduced in Chapter 3.
-------------------------------------------------------------------------
FUNCTION LLS_2CFM,  t, ct, ca, FIT=fit, WEIGHTS=w

 ;WEIGHTS: weigthing function which performs weighthed LLS method
 ;if set to 1, then the linear least squares method will be performed

    IF ARG_PRESENT(fit) THEN fit = fltarr(n_elements(ct))

    IF norm(ct) EQ 0. THEN BEGIN
      ;fit = 0.*ct
       RETURN, [0.,0.,0.,0.]
    ENDIF

    IF n_elements(w) EQ 0 THEN w=1+0*ct

    ct1 = INT_TRAP(t, ct)
    ct2 = INT_TRAP(t, ct1)
    ca1 = INT_TRAP(t, ca)
    ca2 = INT_TRAP(t, ca1)
```

```
    X = LINFIT_SVD(ct*w, -ct2*w, -ct1*w, ca1*w, ca2*w)
    if (X[2] EQ 0) OR (X[0] EQ 0) then return, [0,0,0,0.] ;Case Fp=0

    ;Extract physical parameters

    FP = X[2]
    TT = X[3]/(X[0]*X[2])  ;TOTAL TRANSIT TIME

    prod = X[0]
    sum = X[1]
    det = sum^2 - 4*prod

    IF det LE 0 THEN root=0 ELSE root = sqrt(det)
    TP = (sum-root)/(2*prod)
    TE = (sum+root)/(2*prod)

    if (TE EQ 0) then return, [0,0,0,0.]

    PS = FP*(TT-TP)/TE

    params = [FP, TP, PS, TE]

    IF ARG_PRESENT(fit) THEN fit = - X[0]*ct2 - X[1]*ct1 + X[2]*ca1 + X[3]*ca2

    RETURN, params
END
```

B.3.4 Singular Value Decomposition (SVD)

```
This function calculates the values [a,b,c, d] for the coefficients in
Eq.(4.1).
--------------------------------------------------------------------------
FUNCTION LINFIT_SVD, v, x, y, z, t

;v system of equations to be solved
;x, y, z, t: n-element arrays
;v=ax+by+cz+dt

A= TRANSPOSE([[x],[y],[z],[t]])

;A: matrix to decompose
;Wsvd: n-element vector containing singular values
;Usvd, Vsvd: orthogonal arrays used in the decomposition of A

SVDC, A, Wsvd, Usvd, Vsvd  ;computes the SVDC of matrix A

Xlls = TRANSPOSE(Usvd) ## TRANSPOSE([v])
for K=0,n_elements(Wsvd)-1 DO IF Wsvd[K] GT 0 then Xlls[k] = Xlls[k]/Wsvd[k]

RETURN, Vsvd ## Xlls
```

```
END
```

B.3.5 SSD

```
This function computes similarity measure of SSD between target image and
motion corrected image.
------------------------------------------------------------------------

FUNCTION ffd_chisq, Source, Target, d

  ffd_precompute, Source, size(REFORM(d[0,*,*]), /dimensions)
  Corrected = ffd(Source, d)

  RETURN, 100*total((Target-Corrected)^2.)/total(Target^2.)

END
```

B.3.6 Backtracking Line Search

```
This function performs the backtracking subroutine,
The subroutine requires the following input:

alpha_init = the initial step size,
d =  the current position,
G = the direction of search,
ChiSq_init = the current function value.
------------------------------------------------------------------------

FUNCTION ffd_lsearch, Source, Target, d, G, conv=converged, step=step

  if n_elements(step) eq 0 then step = 1.0 ;precision in pixel-sizes

  converged = 0
  alpha_init = 10.0 ;initial step size in number of pixels

  Gnorm = G/sqrt(total(G^2))
  ChiSq_init = ffd_chisq(Source, Target, d)

  ;backtrack until smaller chisq

  alpha_try = alpha_init
  d_try = d - alpha_try*Gnorm
  ChiSq_try = ffd_chisq(Source, Target, d_try)

  while ChiSq_try GE ChiSq_init do BEGIN
        converged = alpha_try LT step
        if converged then return, d
        alpha_try = alpha_try/10E
        d_try = d - alpha_try*Gnorm
```

```
      ChiSq_try = ffd_chisq(Source, Target, d_try)
  ENDWHILE

  ;forward until increase in chisq

  ChiSq_curr = ChiSq_try
  d_curr = d_try
  alpha_try += step
  d_try = d - alpha_try*Gnorm
  ChiSq_try = ffd_chisq(Source, Target, d_try)

  while ChiSq_try LT ChiSq_curr do BEGIN
      ChiSq_curr = ChiSq_try
      d_curr = d_try
      alpha_try += step
      d_try = d - alpha_try*Gnorm
      ChiSq_try = ffd_chisq(Source, Target, d_try)
      if alpha_try GT 1E+2 then break
  ENDWHILE

  return, d_curr

END
```

B.3.7 Interpolation of the Deformation Field

```
This function interpolates the current low resolution deformation
field (d) so that it has the same dimensions as the I_corr. Bilinear
interpolation is performed using the IDL function INTERPOLATE().
-------------------------------------------------------------------

FUNCTION ffd_interpol, d, nint

  n = size(d, /dimensions)
  n = n[1:*]

  X = (n[0]-1)*findgen(nint[0])/(nint[0]-1E)
  Y = (n[1]-1)*findgen(nint[1])/(nint[1]-1E)

  dint = fltarr(3,nint[0],nint[1],nint[2],125)

  dint[0,*,*,*] = INTERPOLATE(reform(d[0,*,*,*]), X, Y, /GRID)
  dint[1,*,*,*] = INTERPOLATE(reform(d[1,*,*,*]), X, Y, /GRID)

  return, dint

END
```

Bibliography

[1] McRobbie, D. W., Moore, E. A., Graves, M. J., and Prince, M. R. (2007) *MRI: From Picture to Proton*. No. 4, Cambridge: Cambridge University Press.

[2] Jackson, A., O'Connor, J. P. B., Parker, G. J. M., and Jayson, G. C. (2007) Imaging tumor vascular heterogeneity and angiogenesis using dynamic contrast-enhanced magnetic resonance imaging. **13**, 3449–3459.

[3] Yankeelov, T. E. and Gore, J. C. (2009) Dynamic Contrast Enhanced Magnetic Resonance Imaging in Oncology: Theory, Data Acquisition, Analysis, and Examples. *Current Medical Imaging Reviews*, **3**, 91–107.

[4] Song, T., Laine, A. F., Chen, Q., Rusinek, H., Bokacheva, L., Lim, R. P., Laub, G., Kroeker, R., and Lee, V. S. (2009) Optimal k-space sampling for dynamic contrast-enhanced MRI with an application to MR renography. *Magnetic Resonance in Medicine*, **61**, 1242–1248.

[5] Lipton, M. L. (2008) *Totally accessible MRI: a user's guide to principles, technology, and applications*. New York: Springer.

[6] Bloch, F. (1946) Nuclear induction. *Physical Review*, **70**, 460–474.

[7] Liney, G. (2007) *MRI in Clinical Practice*. Springer Science & Business Media.

[8] Roberts, C., Issa, B., Stone, A., Jackson, A., Waterton, J. C., and Parker, G. J. M. (2006) Comparative study into the robustness of compartmental modeling and model-free analysis in DCE-MRI studies. *Journal of Magnetic Resonance Imaging*, **23**, 554–563.

[9] Hall, J. E. and Guyton, A. C. (2011) *Guyton and Hall Textbook of Medical Physiology*. Saunders/Elsevier.

[10] Knesplova, L. and Krestin, G. P. (1998) Magnetic resonance in the assessment of renal function. *European Radiology*, **8**, 201–211.

[11] Sourbron, S. P., Michaely, H. J., Reiser, M. F., and Schoenberg, S. O. (2008) MRI-measurement of perfusion and glomerular filtration in the human kidney with a separable compartment model. *Investigative Radiology*, **43**, 40–48.

[12] Tofts, P. S. (1997) Modeling tracer kinetics in dynamic Gd-DTPA MR imaging. *Journal of Magnetic Resonance Imaging*, **7**, 91–101.

[13] Sourbron, S. P. and Buckley, D. L. (2012) Tracer kinetic modelling in MRI: estimating perfusion and capillary permeability. *Physics in Medicine and Biology*, **57**, R1–R33.

[14] Sourbron, S. P. and Buckley, D. L. (2013) Classic models for dynamic contrast-enhanced MRI. *NMR in Biomedicine*, **26**, 1004–1027.

[15] Perl, W., Lassen, N., and Effros, R. (1975) Matrix proof of flow, volume and mean transit time theorems for regional and compartmental systems. *Bulletin of Mathematical Biology*, **37**, 573 – 588.

[16] Jacquez, J. A. (1972) *Compartmental Analysis in Biology and Medicine*. Amsterdam: Elsevier Pub. Co.

[17] Lassen, N. A. and William, P. (1979) *Tracer Kinetic Methods in Medical Physiology*. New York, Raven Press.

[18] Kety, S. S. (1951) The theory and applications of the exchange of inert gas at the lungs and tissues. *Pharmacological Reviews*, **3**, 1–41.

[19] Crone, C. (1963) The permeability of capillaries in various organs as determined by use of the 'Indicator Diffusion' method. *Acta Physiologica Scandinavica*, **58**, 292–305.

[20] Tofts, P. S. and Kermode, A. G. (1991) Measurement of the blood-brain barrier permeability and leakage space using dynamic MR imaging. 1. Fundamental concepts. *Magnetic Resonance in Medicine*, **17**, 357–367.

[21] Brix, G., Kiessling, F., Lucht, R., Darai, S., Wasser, K., Delorme, S., and Griebel, J. (2004) Microcirculation and microvasculature in breast tumors: Pharmacokinetic analysis of dynamic MR image series. *Magnetic Resonance in Medicine*, **52**, 420–429.

[22] Boyce, W. E. and DiPrima, R. C. (2001) *Elementary differential equations and boundary value problems*. Wiley.

[23] Parker, G. J. M., Roberts, C., Macdonald, A., Buonaccorsi, G. A., Cheung, S., Buckley, D. L., Jackson, A., Watson, Y., Davies, K., and Jayson, G. C. (2006) Experimentally-derived functional form for a population-averaged high-temporal-resolution arterial input function for dynamic contrast-enhanced MRI. *Magnetic Resonance in Medicine*, **56**, 993–1000.

[24] Orton, M. R., D'Arcy, J. A., Walker-Samuel, S., Hawkes, D. J., Atkinson, D., Collins, D. J., and Leach, M. O. (2008) Computationally efficient vascular input function models for quantitative kinetic modelling using DCE-MRI. *Physics In Medicine and Biology*, **53**, 1225–1239.

[25] Mouridsen, K., Christensen, S., Gyldensted, L., and Østergaard, L. (2006) Automatic selection of arterial input function using cluster analysis. *Magnetic Resonance in Medicine*, **55**, 524–531.

[26] Peruzzo, D., Bertoldo, A., Zanderigo, F., and Cobelli, C. (2011) Automatic selection of arterial input function on dynamic contrast-enhanced MR images. *Computer Methods and Programs in Biomedicine*, **104**, 148–157.

[27] Crum, W. R., Hartkens, T., and Hill, D. L. G. (2004) Non-rigid image registration: theory and practice. *The British Journal of Radiology*, **77**, S140–S153.

[28] Modersitzki, J. (2003) *Numerical Methods for Image Registration*. Oxford: Oxford University Press.

[29] Sederberg, T. W. and Parry, S. R. (1986) Free-form deformation of solid geometric models. *ACM SIGGRAPH Computer Graphics*, **20**, 151–160.

[30] Rueckert, D., Sonoda, L. I., Hayes, C., Hill, D. L., Leach, M. O., and Hawkes, D. J. (1999) Nonrigid registration using free-form deformations: application to breast MR images. *IEEE Transactions on Medical Imaging*, **18**, 712–721.

[31] Kybic, J. and Unser, M. (2003) Fast parametric elastic image registration. *IEEE Transactions on Image Processing*, **12**, 1427–1442.

[32] Sdika, M. (2008) A fast nonrigid image registration with constraints on the Jacobian using large scale constrained optimization. *IEEE Transactions on Medical Imaging*, **27**, 271–281.

[33] Štava, O. and Beneš, B. (2011) *GPU Computing Gems Emerald Edition*. MA: Morgan Kaufmann/Elsevier.

[34] Lee, S., Wolberg, G., Chwa, K. Y., and Shin, S. Y. (1996) Image metamorphosis with scattered feature constraints. *IEEE Transactions on Visualization and Computer Graphics*, **2**, 337–354.

[35] Szeliski, R. and Coughlan, J. (1997) Spline-based image registration. *International Journal of Computer Vision*, **22**, 199–218.

[36] Fahmy, M. F., Abdel Hameed, T. K., and Fahmy, G. F. (2007) A fast B_spline based algorithm for image zooming and compression. *National Radio Science Conference, NRSC, Proceedings*, p. 35.

[37] Hajnal, J. V., Hawkes, D. J., and Hill, D. L. G. (2001) Medical Image Registration. *Physics in Medicine and Biology*, **46**, R1–R45.

[38] Bertsekas, D. (1999) *Nonlinear Programming*. Athena Scientific.

[39] Nocedal, J. and Wright, S. J. (1999) *Numerical Optimization*. No. 2, New York: Springer.

[40] Klein, S., Staring, M., and Pluim, J. P. W. (2007) Evaluation of optimization methods for nonrigid medical image registration using mutual information and B-splines. *IEEE Transactions on Image Processing*, **16**, 2879–2890.

[41] Sun, W., Niessen, W. J., Van Stralen, M., and Klein, S. (2013) Simultaneous multiresolution strategies for nonrigid image registration. *IEEE Transactions on Image Processing*, **22**, 4905–4917.

[42] Lester, H. and Arridge, S. R. (1999) A survey of hierarchical non-linear medical image registration. *Pattern Recognition*, **32**, 129–149.

[43] Brandner, E. D., Wu, A., Chen, H., Heron, D., Kalnicki, S., Komanduri, K., Gerszten, K., Burton, S., Ahmed, I., and Shou, Z. (2006) Abdominal organ motion measured using 4D CT. *International Journal of Radiation Oncology Biology Physics*, **65**, 554–560.

[44] Flouri, D., Lesnic, D., and Sourbron, S. P. (2016) Fitting the two-compartment model in DCE-MRI by linear inversion. *Magnetic Resonance in Medicine*, **76**, 998–1006.

[45] Patlak, C. S., Blasberg, R. G., and Fenstermacher, J. D. (1983) Graphical evaluation of blood-to-brain transfer constants from multiple-time uptake data. *Journal of cerebral blood flow and metabolism : official journal of the International Society of Cerebral Blood Flow and Metabolism*, **3**, 1–7.

[46] Tofts, P. S., et al. (1999) Estimating Kinetic Parameters From Dynamic Contrast-Enhanced T1-Weighted\tMRI of a Diffusable Tracer: Standardized Quantities and Symbols. *Journal of Magnetic Resonance Imaging*, **10**, 223–232.

[47] Annet, L., Hermoye, L., Peeters, F., Jamar, F., Dehoux, J.-P., and Van Beers, B. E. (2004) Glomerular filtration rate: assessment with dynamic contrast-enhanced MRI and a cortical-compartment model in the rabbit kidney. *Journal of Magnetic Resonance Imaging : JMRI*, **20**, 843–849.

[48] Ahearn, T. S., Staff, R. T., Redpath, T. W., and Semple, S. I. K. (2005) The use of the Levenberg-Marquardt curve-fitting algorithm in pharmacokinetic modelling of DCE-MRI. *Physics in Medicine and Biology*, **50**, N85–92.

[49] Feng, D., Huang, S. C., Wang, Z., and Ho, D. (1996) An unbiased parametric imaging algorithm for nonuniformly sampled biomedical system parameter estimation. *IEEE Transactions on Medical Imaging*, **15**, 512–518.

[50] Chen, H., Li, F., Zhao, X., Yuan, C., Rutt, B., and Kerwin, W. S. (2011) Extended graphical model for analysis of dynamic contrast-enhanced MRI. *Magnetic Resonance in Medicine*, **66**, 868–878.

[51] Leporq, B., Camarasu-Pop, S., Davila-Serrano, E. E., Pilleul, F., and Beuf, O. (2013) Enabling 3D-liver perfusion mapping from MR-DCE imaging using distributed computing. *Journal of Medical Engineering*, **2013**, Article ID 471682.

[52] Murase, K. (2004) Efficient method for calculating kinetic parameters using T1-weighted dynamic contrast-enhanced magnetic resonance imaging. *Magnetic Resonance in Medicine*, **51**, 858–862.

[53] Adluru, G., DiBella, E. V. R., and Schabel, M. C. (2006) Model-based registration for dynamic cardiac perfusion MRI. *Journal of Magnetic Resonance Imaging*, **24**, 1062–1070.

[54] Faranesh, A. Z., Kraitchman, D. L., and McVeigh, E. R. (2006) Measurement of kinetic parameters in skeletal muscle by magnetic resonance imaging with an intravascular agent. *Magnetic Resonance in Medicine*, **55**, 1114–1123.

[55] Li, J., Yu, Y., Zhang, Y., Bao, S., Wu, C., Wang, X., Li, J., Zhang, X., and Hu, J. (2009) A clinically feasible method to estimate pharmacokinetic parameters in breast cancer. *Medical Physics*, **36**, 3786–3794.

[56] Cárdenas-Rodríguez, J., Howison, C. M., and Pagel, M. D. (2013) A linear algorithm of the reference region model for DCE-MRI is robust and relaxes requirements for temporal resolution. *Magnetic Resonance Imaging*, **31**, 497–507.

[57] Feng, D., Ho, D., Chen, K., Wu, L. C., Wang, J. K., Liu, R. S., and Yeh, S. H. (1995) An evaluation of the algorithms for determining local cerebral metabolic rates of glucose using positron emission tomography dynamic data. *IEEE Transactions on Medical Imaging*, **14**, 697–710.

[58] Wen, L., Eberl, S., Fulham, M. J., Feng, D., and Bai, J. (2009) Constructing reliable parametric images using enhanced GLLS for dynamic SPECT. *IEEE Transactions on Biomedical Engineering*, **56**, 1117–1126.

[59] Dai, X., Chen, Z., and Tian, J. (2011) Performance evaluation of kinetic parameter estimation methods in dynamic FDG-PET studies. *Nuclear Medicine Communications*, **32**, 4–16.

[60] Zeng, G. L., Hernandez, A., Kadrmas, D. J., and Gullberg, G. T. (2012) Kinetic parameter estimation using a closed-form expression via integration by parts. *Physics in Medicine and Biology*, **57**, 5809–5821.

[61] Zeng, G. L., Kadrmas, D. J., and Gullberg, G. T. (2012) Fourier domain closed-form formulas for estimation of kinetic parameters in multi-compartment models. *IEEE Nuclear Science Symposium Conference Record*, pp. 3209–3216.

[62] Lim, S. W., Chrysochou, C., Buckley, D. L., Kalra, P. a., and Sourbron, S. P. (2013) Prediction and assessment of responses to renal artery revascularization with dynamic contrast-enhanced magnetic resonance imaging: a pilot study. *American Journal of Physiology. Renal Physiology*, **305**, F672–F678.

[63] Markwardt, C. B. (2009) Non-linear Least-squares Fitting in IDL with MPFIT. *Astronomical Data Analysis Software and Systems XVIII ASP Conference Series*, **411**, 251.

[64] Wang, C., Yin, F.-F., and Chang, Z. (2015) An efficient calculation method for pharmacokinetic parameters in brain permeability study using dynamic contrast-enhanced MRI. *Magnetic Resonance in Medicine*, **75**, 739–749.

[65] Cai, W., Feng, D., Fulton, R., and Siu, W.-C. (2002) Generalized linear least squares algorithms for modeling glucose metabolism in the human brain with corrections for vascular effects. *Computer Methods and Programs in Biomedicine*, **68**, 1–14.

[66] Ichise, M., Toyama, H., Innis, R. B., and Carson, R. E. (2002) Strategies to improve neuroreceptor parameter estimation by linear regression analysis. *Jourbal of Cerebral Blood Flow & Metabolism*, **22**, 1271–1281.

[67] Chen, K., Lawson, M., Reiman, E., Cooper, A., Feng, D., Huang, S. C., Bandy, D., Ho, D., Yun, L. S., and Palant, A. (1998) Generalized linear least squares method for fast generation of myocardial blood flow parametric images with N-13 ammonia PET. *IEEE Transactions on Medical Imaging*, **17**, 236–243.

[68] Banks, H. T., Dediu, S., and Ernstberger, S. L. (2007) Sensitivity functions and their uses in inverse problems. *Journal of Inverse and Ill-Posed Problems*, **15**, 683–708.

[69] Veraart, J., Sijbers, J., Sunaert, S., Leemans, A., and Jeurissen, B. (2013) Weighted linear least squares estimation of diffusion MRI parameters: Strengths, limitations, and pitfalls. *NeuroImage*, **81**, 335–346.

[70] Kershaw, L. E. and Buckley, D. L. (2006) Precision in measurements of perfusion and microvascular permeability with T1-weighted dynamic contrast-enhanced MRI. *Magnetic Resonance in Medicine*, **56**, 986–992.

[71] Lee, V. S., Rusinek, H., Noz, M. E., Lee, P., Raghavan, M., and Kramer, E. L. (2003) Dynamic three-dimensional MR renography for the measurement of single kidney function: initial experience. *Radiology*, **227**, 289–294.

[72] Sun, Y., Jolly, M. P., and Moura, J. M. F. (2004) Integrated registration of dynamic renal perfusion MR images. *Proceedings - International Conference on Image Processing, ICIP*, vol. 3, pp. 1923–1926.

[73] Zikic, D., Sourbron, S. P., Feng, X., Michaely, H. J., Khamene, A., and Navab, N. (2008) Automatic alignment of renal DCE-MRI image series for improvement of quantitative tracer kinetic studies. *Proceedings of Medical Imaging: Image Processing. International Society for Optical Engineering (SPIE*, pp. 1–8, no. March.

[74] Song, T., Lee, V. S., Chen, Q., Rusinek, H., and Laine, A. F. (2010) An automated three-dimensional plus time registration framework for dynamic MR renography. *Journal of Visual Communication and Image Cepresentation*, **21**, 1–8.

[75] Positano, V., Bernardeschi, I., Zampa, V., Marinelli, M., Landini, L., and Santarelli, M. F. (2013) Automatic 2D registration of renal perfusion image sequences by mutual information and adaptive prediction. *Magma*, **26**, 325–335.

[76] Sance, R., Ledesma-Carbayo, M. J., Lundervold, A., and Santos, A. (2007) Alignment of 3D DCE-MRI abdominal series for optimal quantification of kidney function. *ISPA 2007 - Proceedings of the 5th International Symposium on Image and Signal Processing and Analysis*, pp. 413–417.

[77] Zöllner, F. G., Sance, R., Rogelj, P., Ledesma-Carbayo, M. J., Rørvik, J., Santos, A., and Lundervold, A. (2009) Assessment of 3D DCE-MRI of the kidneys using non-rigid image registration and segmentation of voxel time courses. *Computerized Medical Imaging and Graphics*, **33**, 171–181.

[78] Wang, H., Dong, L., O'Daniel, J., Mohan, R., Garden, A. S., Ang, K. K., Kuban, D. a., Bonnen, M., Chang, J. Y., and Cheung, R. (2005) Validation of an accelerated 'demons' algorithm for deformable image registration in radiation therapy. *Physics in Medicine and Biology*, **50**, 2887–2905.

[79] Yang, X., Ghafourian, P., Sharma, P., Salman, K., Martin, D., and Fei, B. (2012) Nonrigid Registration and Classification of the Kidneys in 3D Dynamic Contrast Enhanced (DCE) MR Images. *Proceedings of SPIE*, **8314**, 83140B.

[80] Merrem, A. D., Zöllner, F. G., Reich, M., Lundervold, A., Rorvik, J., and Schad, L. R. (2013) A variational approach to image registration in dynamic contrast-enhanced MRI of the human kidney. *Magnetic Resonance Imaging*, **31**, 771–777.

[81] Chefd'hotel, C., Hermosillo, G., and Faugeras, O. (2001) A variational approach to multi-modal image matching. *Variational and Level Set Methods in Computer Vision, 2001. Proceedings. IEEE Workshop on*, pp. 21–28.

[82] Khalifa, F., Beache, G. M., El-Ghar, M. A., El-Diasty, T., Gimel'farb, G., Kong, M., and El-Baz, A. (2013) Dynamic contrast-enhanced MRI-based early detection of acute renal transplant rejection. *IEEE Transactions on Medical Imaging*, **32**, 1910–1927.

[83] Liu, W. and Ruan, D. (2013) Estimating nonrigid motion from inconsistent intensity with robust shape features. *Medical Physics*, **40**, 121912–1–121912–13.

[84] Conlin, C. C., Zhang, J. L., Rousset, F., Vachet, C., Zhao, Y., Morton, K. A., Carlston, K., Gerig, G., and Lee, V. S. (2015) Performance of an efficient image-registration algorithm in processing MR renography data. *Journal of Magnetic Resonance Imaging : JMRI*, **43**, 391–397.

[85] Melbourne, A., Atkinson, D., White, M. J., Collins, D., Leach, M., and Hawkes, D. (2007) Registration of dynamic contrast-enhanced MRI using a progressive principal component registration (PPCR). *Physics in Medicine and Biology*, **52**, 5147–5156.

[86] Wollny, G., Kellman, P., Santos, A., and Ledesma-Carbayo, M. J. (2012) Automatic motion compensation of free breathing acquired myocardial perfusion data by using independent component analysis. *Medical Image Analysis*, **16**, 1015 – 1028.

[87] Hamy, V., et al. (2014) Respiratory motion correction in dynamic MRI using robust data decomposition registration Application to DCE-MRI. *Medical Image Analysis*, **18**, 301–313.

[88] Buonaccorsi, G. A., et al. (2007) Tracer kinetic model-driven registration for dynamic contrast-enhanced MRI time-series data. *Magnetic Resonance in Medicine*, **58**, 1010–1019.

[89] Likhite, D., Adluru, G., and DiBella, E. (2015) Deformable and rigid model-based image registration for quantitative cardiac perfusion. Camara, O., Mansi, T., Pop, M., Rhode, K., Sermesant, M., and Young, A. (eds.), *Statistical Atlases and Computational Models of the Heart - Imaging and Modelling Challenges*, vol. 8896 of *Lecture Notes in Computer Science*, pp. 41–50, Springer International Publishing.

[90] White, C. J. and Olin, J. W. (2009) Diagnosis and management of atherosclerotic renal artery stenosis: improving patient selection and outcomes. *Nature Clinical Practice Cardiovascular medicine*, **6**, 176–190.

[91] Zoccali, C. (2002) Atherosclerotic Renal Artery Stenosis: Epidemiology, Cardiovascular Outcomes, and Clinical Prediction Rules. *Journal of the American Society of Nephrology*, **13**, 179 – 183.

[92] Chrysochou, C. and Kalra, P. A. (2009) Epidemiology and Natural History of Atherosclerotic Renovascular Disease. *Progress in Cardiovascular Diseases*, **52**, 184–195.

[93] Chrysochou, C. and Kalra, P. A. (2008) Atheromatous renovascular disease: Overview and challenges. *Journal of Renal Care*, **34**, 179–190.

[94] Huang, A. J., Lee, V. S., and Rusinek, H. (2003) MR imaging of renal function. *Radiologic Clinics of North America*, **41**, 1001–1017.

[95] Hackstein, N., Heckrodt, J., and Rau, W. S. (2003) Measurement of Single-Kidney Glomerular Filtration Rate Using a Contrast-Enhanced Dynamic Gradient-Echo Sequence and the Rutland-Patlak Plot Technique. *Journal of Magnetic Resonance Imaging*, **18**, 714–725.

[96] Rehling, M., Møller, M. L., Lund, J. O., Jensen, K. B., Thamdrup, B., and Trap-Jensen, J. (1985) 99mTc-DTPA gamma-camera renography: Normal values and rapid determination of single-kidney glomerular filtration rate. *European Journal of Nuclear Medicine*, **11**, 1–6.

[97] Grenier, N., Mendichovszky, I., de Senneville, B. D., Roujol, S., Desbarats, P., Pedersen, M., Wells, K., Frokiaer, J., and Gordon, I. (2008) Measurement of Glomerular Filtration Rate With Magnetic Resonance Imaging: Principles, Limitations, and Expectations. *Seminars in Nuclear Medicine*, **38**, 47–55.

[98] Notohamiprodjo, M., Reiser, M. F., and Sourbron, S. P. (2010) Diffusion and perfusion of the kidney. *European Journal of Radiology*, **76**, 337–347.

[99] Buckley, D. L., Shurrab, A. E., Cheung, C. M., Jones, A. P., Mamtora, H., and Kalra, P. A. (2006) Measurement of single kidney function using dynamic contrast-enhanced MRI: Comparison of two models in human subjects. *Journal of Magnetic Resonance Imaging*, **24**, 1117–1123.

[100] Lee, V. S., et al. (2007) Renal function measurements from MR renography and a simplified multicompartmental model. *American Journal of Physiology. Renal Physiology*, **292**, F1548–F1559.

[101] Vivier, P. H., et al. (2011) Kidney function: glomerular filtration rate measurement with MR renography in patients with cirrhosis. *Radiology*, **259**, 462–70.

[102] Bokacheva, L., Rusinek, H., Zhang, J. L., Chen, Q., and Lee, V. S. (2009) Estimates of glomerular filtration rate from MR renography and tracer kinetic models. *Journal of Magnetic Resonance Imaging*, **29**, 371–382.

[103] Eikefjord, E., Andersen, E., Hodneland, E., Hanson, E., Sourbron, S., Svarstad, E., Lundervold, A., and Rorvik, J. T. (2016) Dynamic contrast-enhanced MRI measurement of renal function in healthy participants. *Acta Rdiologica*, [Epub].

[104] Hackstein, N., Kooijman, H., Tomaselli, S., and Rau, W. S. (2005) Glomerular filtration rate measured using the Patlak plot technique and contrast-enhanced dynamic MRI with different amounts of gadolinium-DTPA. *Journal of Magnetic Resonance Imaging*, **22**, 406–414.

[105] Petersen, L. (1999) Glomerular filtration rate estimated from the uptake phase of 99Tc-DTPA renography in chronic renal failure. *Nephrology Dialysis Transplantation*, **14**, 1673–1678.

[106] Attenberger, U. I., et al. (2010) Comprehensive MR evaluation of renal disease: Added clinical value of quantified renal perfusion values over single MR angiography. *Journal of Magnetic Resonance Imaging*, **31**, 125–133.

[107] Garpebring, A., Wirestam, R., Östlund, N., and Karlsson, M. (2011) Effects of inflow and radiofrequency spoiling on the arterial input function in dynamic contrast-enhanced MRI: A combined phantom and simulation study. *Magnetic Resonance in Medicine*, **65**, 1670–1679.

[108] Dujardin, M., Sourbron, S., Luypaert, R., Verbeelen, D., and Stadnik, T. (2005) Quantification of renal perfusion and function on a voxel-by-voxel basis: A feasibility study. *Magnetic Resonance in Medicine*, **54**, 841–849.

[109] O'Connor, J. A. P. G. J., J. P. and Jayson, G. C. (2007) DCE-MRI biomarkers in the clinical evaluation of antiangiogenic and vascular disrupting agents. *British Journal of Cancer*, **96**, 189–195.

[110] Mendichovszky, I. A., Cutajar, M., and Gordon, I. (2009) Reproducibility of the aortic input function (AIF) derived from dynamic contrast-enhanced magnetic resonance imaging (DCE-MRI) of the kidneys in a volunteer study. *European Journal of Radiology*, **71**, 576–581.

[111] Dickie, B. R., Banerji, A., Kershaw, L. E., McPartlin, A., Choudhury, A., West, C. M., and Rose, C. J. (2016) Improved accuracy and precision of tracer kinetic parameters by joint fitting to variable flip angle and dynamic contrast enhanced mri data. *Magnetic Resonance in Medicine*, **76**, 1270–1281.